



Horizon 2020
Programme

METIS

Research and Innovation Action (RIA)

This project has received funding from the European
Union's Horizon 2020 research and innovation programme
under grant agreement No 945121

Start date : 2020-09-01 Duration : 48 Months

Physics-based simulation of ground motion tools and database

Authors : Dr. Irmela ZENTNER (EDF), Takashi Akazawa, Luis Alvarez Sanchez, Gabriele Ameri, David Baumont, Fabrice Cotton, Kojiro Irikura, Marco Pilz, Hoby Razafindrakoto, Ludivine Saint Mard, Hussein Shible, Kazuhiro Somei

METIS - Contract Number: 945121

Project officer: Katerina PTACKOVA

Document title	Physics-based simulation of ground motion tools and database
Author(s)	Dr. Irmela ZENTNER, Takashi Akazawa, Luis Alvarez Sanchez, Gabriele Ameri, David Baumont, Fabrice Cotton, Kojiro Irikura, Marco Pilz, Hoby Razafindrakoto, Ludivine Saint Mard, Hussein Shible, Kazuhiro Somei
Number of pages	107
Document type	Deliverable
Work Package	WP4
Document number	D4.3
Issued by	EDF
Date of completion	2023-04-11 08:55:29
Dissemination level	Public

Summary

One of the goals of METIS WP4 is to develop methods to generate synthetic ground motion time histories on bedrock using source and path terms consistent with the ones used to compute seismic hazard. For this purpose METIS proposes to develop and compare a suite of open-source tools to perform physics-based simulations for engineering application. Both stochastic, empirical and hybrid models are assessed and further developed for use in low to moderate seismicity areas such as encountered in most European nuclear countries. This report builds on deliverable D5.1, entitled Methodology for selecting ensembles of rock-hazard consistent ground motions for fragility curve computations and datasets for WP6, where more detail can be found on the ground motion selection strategies developed in METIS project and engineering validation of stochastic ground motion databases. This report summarizes the ground motion simulation and modification methods that have been analysed and applied or further developed within METIS WP4. More precisely, the 4 ground motion definition methods analysed in this work are the following: ? Irikura recipe with EGF ? 3D Stochastic physics-based approach ? Hybrid approach combining NGF and stochastic model for higher frequencies ? Recorded ground motion corrected for site response effects using spectral decomposition ? EGF-based ground motion simulation technique where rock motion is obtained by deconvolution For this purpose, existing opensource tools such as SCEC platform (<https://www.scec.org/>) and as well as two new tools, one implementing an improved version of the Otardole 3D stochastic ground motion simulation method and the other one implementing the Irikura recipe, are included in the analysis. The METIS codes for physics-based strong-motion simulation in Europe developed in the projects will be disseminated through METIS website (links to the repositories/websites describing the methods). The two last approaches, deemed suitable for the purpose of creation of a scenario-specific rock ground motion including uncertainty, are applied to METIS study. First results are shown but require further work in the framework of WP4. Indeed, in agreement with the rationale of METIS where hazard and ground motion is developed on bedrock level, no particular site term has to be introduced in the stochastic approach. This is an advantage over other methods that rely on records (used as EGF) that have been recorded nearby but not on th...

Approval

Date	By
2023-04-11 09:08:14	Dr. Marco PAGANI (GEM)
2023-04-11 09:11:19	Dr. Irmela ZENTNER (EDF)



METIS

Seismic Risk Assessment
for Nuclear Safety

Research & Innovation Action

NFRP-2019-2020

Methodologies for physics-based simulation of ground motion

Analysis of different approaches and applications to METIS case study

Deliverable D4.3

Version N°2

Authors:

Takashi Akazawa

Luis Alvarez-Sanchez

Gabriele Ameri

David Baumont

Fabrice Cotton

Kojiro Irikura

Marco Pilz

Hoby Razafindrakoto

Ludivine Saint-Mard

Hussein Shible

Kazuhiro Somei

Irmela Zentner



This project has received funding from the Horizon 2020 programme under grant agreement n°945121. The content of this presentation reflects only the author's view. The European Commission is not responsible for any use that may be made of the information it contains.



Document Information

Grant agreement	945121
Project title	Methods And Tools Innovations For Seismic Risk Assessment
Project acronym	METIS
Project coordinator	Dr. Irmela Zentner, EDF
Project duration	1 st September 2020 – 31 st August 2024 (48 months)
Related work package	WP4 – PSHA on rock
Related task(s)	Task 4.5 SIMULATION OF STRONG GROUND-MOTION ON BEDROCK
Lead organisation	GFZ, EDF
Contributing partner(s)	EDF, GFZ, GRI, Seister, GEM
Due date	30 th January 2023
Submission date	February 2023
Dissemination level	

History

Version	Submitted by	Reviewed by	Date	Comments
N°1	Irmela Zentner, Luis Alvarez-Sanchez	Marco Pagani Paola Traversa Francesca Pacor	8/02/2023 5/04/2023	Update of report and response detailed to reviewers



Table of Contents

1.	Introduction.....	8
2.	Validation and Verification (V&V) strategies	10
3.	Ground motion simulation methodologies	13
3.1.	Irikura recipe with empirical Green's functions (EGF)	13
3.1.1.	Methodology	13
3.1.2.	Validation/application for KK NPP case study	14
3.1.3.	Advantages/disadvantages of the approach for engineering applications.....	17
3.2.	Hybrid stochastic method using the SCEC platform	17
3.2.1.	Methodology	17
3.2.2.	Example application and validation for Central Italy and Rhine Graben case.....	17
3.2.3.	Advantages/disadvantages of the approach for engineering applications.....	23
3.3.	3D Stochastic simulation based on Otavola method	23
3.3.1.	Methodology	23
3.3.2.	Validation for Japanese data - seismological tests.....	24
3.3.3.	Validation to EDP - European database	31
3.3.4.	Advantages/disadvantages of the approach for engineering applications.....	34
3.4.	Recorded ground motion corrected for site term	35
3.4.1.	Methodology	35
3.4.2.	Validation and example application	36
3.4.3.	Advantages/disadvantages of the approach for engineering applications.....	38
3.5.	Combining spectral decomposition and empirical Green's functions approach to simulate time histories at bedrock conditions	39
3.5.1.	Methodology	39
3.5.2.	Advantages/disadvantages of the approach for engineering applications.....	41
3.6.	Summary of modelling options discussed	42
4.	Approach(es) for METIS case study application	43
4.1.	Example application of Seister approach.....	43
4.2.	3D Stochastic rock motion database (proposal for approach to be implemented)	50
5.	Conclusions and further work.....	50
6.	Acknowledgments	50
7.	Bibliography.....	51
8.	Appendix	58
8.1.	SCEC platform	58
8.2.	Details on the Seister approach and application	59



Abbreviations and Acronyms

Acronym	Description
AI	Arias intensity
CAV	Cumulative absolute velocity
CS	Conditional spectrum
D ₅₋₉₅	5-95% significant duration
EDP(s)	Engineering demand parameter(s)
EGF	Empirical Green's function
FAS	Fourier Amplitude Spectrum
GIT	General inversion technique
GM	Geometrical Mean of the horizontal components
GMMs	Ground motion model(s) (often called GMPE-Ground Motion Prediction Model)
GMSM	Ground motion simulation methodology(s)
GP	Graves and Pitarka
GRI	Japanese Geo Research Institut
IM(s)	Intensity measure(s)
KK NPP	Kashiwazaki-Kariwa Nuclear Power Plant
MDoF(s)	Multi degree of freedom system(s)
M _w	Moment magnitude
NGF	Numerical Green's Function
NPP	Nuclear power plant
PBEE	Performance based earthquake engineering
PGA	Peak ground acceleration
PGV	Peak ground velocity
PSA	Pseudo Spectral Acceleration
PSHA	Probabilistic seismic hazard analysis

Rjb	Joyner and Boore distance
R _{hypocentral}	Hypocentral distance
Rrup	Rupture distance
Sa	Spectral acceleration
SDoF(s)	Single Degree of Freedom System(s)
SCEC	Southern California Earthquake Center
SMGA	Strong Motion Generation Area
SSC	Systems, structures and components
T	Period of vibration
UD	Vertical component of the ground motion
V&V	Verification and validation
V _{S30}	Average shear wave velocity in the upper 30m
WP	Work package
ε	Residual



Summary

One of the goals of METIS WP4 is to develop methods to generate synthetic ground motion time histories on bedrock using source and path terms consistent with the ones used to compute seismic hazard. For this purpose METIS proposes to develop and compare a suite of open-source tools to perform physics-based simulations for engineering application. Both stochastic, empirical and hybrid models are assessed and further developed for use in low to moderate seismicity areas such as encountered in most European nuclear countries. This report builds on deliverable D5.1, entitled *Methodology for selecting ensembles of rock-hazard consistent ground motions for fragility curve computations and datasets for WP6*, where more detail can be found on the ground motion selection strategies developed in METIS project and engineering validation of stochastic ground motion databases.

This report summarizes the ground motion simulation and modification methods that have been analysed and applied or further developed within METIS WP4. More precisely, the 4 ground motion definition methods analysed in this work are the following:

- Irikura recipe with EGF
- 3D Stochastic physics-based approach
- Hybrid approach combining NGF and stochastic model for higher frequencies
- Recorded ground motion corrected for site response effects using spectral decomposition
- EGF-based ground motion simulation technique where rock motion is obtained by deconvolution

For this purpose, existing opensource tools such as SCEC platform (<https://www.scec.org/>) and as well as two new tools, one implementing an improved version of the Otardole 3D stochastic ground motion simulation method and the other one implementing the Irikura recipe, are included in the analysis. The METIS codes for physics-based strong-motion simulation in Europe developed in the projects will be disseminated through METIS website (links to the repositories/websites describing the methods).

The two last approaches, deemed suitable for the purpose of creation of a scenario-specific rock ground motion including uncertainty, are applied to METIS study. First results are shown but require further work in the framework of WP4. Indeed, in agreement with the rationale of METIS where hazard and ground motion is developed on bedrock level, no particular site term has to be introduced in the stochastic approach. This is an advantage over other methods that rely on records (used as EGF) that have been recorded nearby but not on the exact location under study and thus may exhibit different site effect. This drawback can be overcome by introducing a site term correction based on the general inversion technique (GIT). The latter allows for the separation of spectral content from source, propagation and site terms for a given location by analysing ground motion databases.

Keywords

Ground motion, simulation, time history, stochastic, Empirical, Numerical, Green's function, source, propagation, site, record, Validation, opensource tool, physics-based, kinematic, seismic scenario

1. Introduction

One of the goals of METIS WP4 is to develop methods to generate synthetic ground motion time histories on bedrock, using source and path terms consistent with the ones used to compute seismic hazard. For this purpose, METIS proposes to develop and compare a suite of open-source tools to perform physics-based simulations for engineering application. Both stochastic and empirical models are assessed and further developed for use in low to moderate seismicity areas, such as is the case of most European countries where nuclear facilities are located.

Generally speaking, physics based stochastic ground motion simulation methods distinguish the source, propagation and site response contributions to the time histories observed on ground surface.

Figure 1 shows an illustration of these contributions.

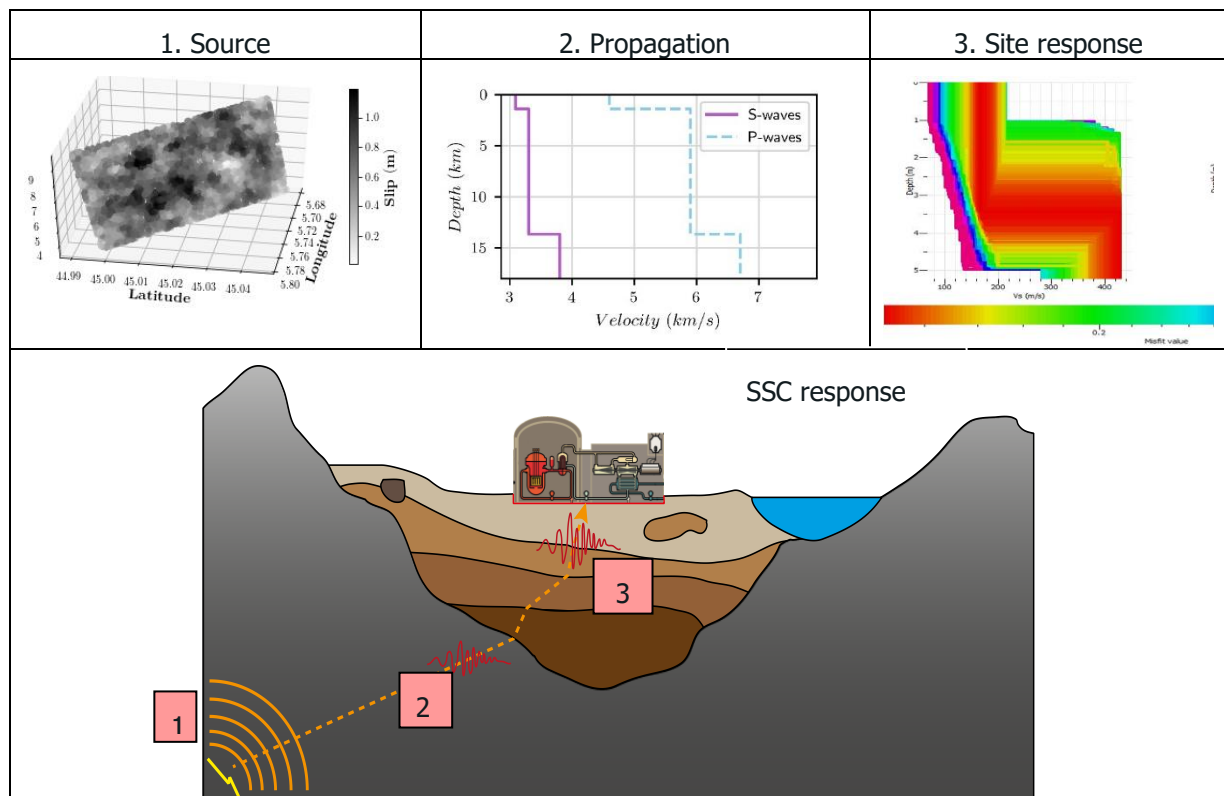


Figure 1: Illustration of Source, propagation, and site response contributions to the motion observed on ground surface (upper), and integration of these contributions in the overall analysis chain (lower)

The integrated approach developed in METIS project considers seismic hazard and hazard consistent ground motion on outcropping rock/bedrock level. Estimating earthquake ground motions at reference bedrock conditions is a major challenge in seismic risk assessment. This is needed, either because the target site is located on outcropping bedrock or because soil response will be subsequently integrated by soil response analysis. The vast majority of strong-motion databases contain earthquake recordings of stations installed on soil or soft-rock sites, while very few stations are on hard-rock sites. This condition thwarts the availability of ground motion time histories at bedrock, especially in the magnitude-distance range of interest for seismic hazard oriented towards engineering applications, i.e., high magnitudes and short distances. This drawback may be overcome by simulating rock ground motion or by correcting observed ground motion from site effects. Both approaches are discussed in this report.

It is acknowledged that the ground motion recorded at bedrock and at outcropping rock levels are not strictly the same. This is due to wave scattering resulting from the heterogeneities and/or due to residual site effects resultant from the upper (more degraded) rock layers. Moreover the output of Probabilistic Seismic Hazard Analysis (PSHA) is not always available for outcropping rock conditions since common Ground Motion Models (GMMs) are not validated for very hard rock conditions. These issues, however, are not discussed here because for the purposes of METIS it is assumed that PSHA results are available for bedrock conditions.

The goal of this report is to assess the adequateness of different approaches to develop scenario-specific and hazard consistent databases of ground motions for the site condition of interest of the METIS project. Such output will then be considered for record selection, applying the methods developed in METIS WP 5. The methodology for site response analysis given (bed)rock ground motion is addressed by deliverable D5.3 entitled *Methodology for site response analysis to obtain surface ground motions from rock-hazard-consistent ground motions*. The overall workflow implemented in project is illustrated below:

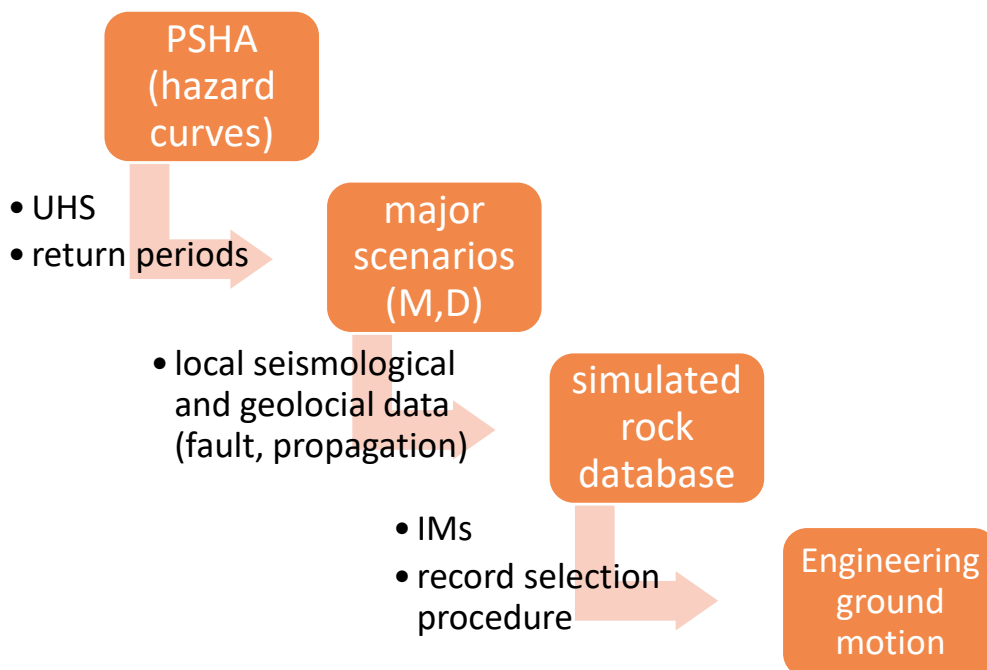


Figure 2: General workflow considered in the METIS project for site-specific response analysis

This report builds on deliverable D5.1, entitled Methodology for selecting ensembles of rock-hazard consistent ground motions for fragility curve computations and datasets for WP6, where more detail can be found on the ground motion selection strategies developed within METIS, alongside the engineering validation of stochastic ground motion databases generated with the ground motion simulation methodology introduced in section 3.3 of this report.

In agreement with the rationale of METIS where hazard and ground motion are developed on bedrock level, no particular site term is required in the simulation of ground motion following the stochastic approach. This represents an advantage over other methods that rely on records (used as EGF) that have been recorded nearby but not on the exact location under study, and thus may exhibit different site effects. This drawback may be overcome by introducing a site term correction based on the general inversion technique (GIT). The latter allows for the disaggregation of the spectral content of ground motions into the contributors shown in **Figure 1**, i.e. source, propagation, and site terms.



Here, different approaches for the development of synthetic ground motion are introduced, analysed and their possible use illustrated through example applications. These methodologies build on existing approaches using stochastic FAS and empirical Green's functions and different methods for source rupture modelling. Specifically, we have tested and applied existing opensource tools available within the SCEC platform (<https://www.scec.org/>), additionally this report considers the in-house software for the Irikura recipe (Irikura, 1983) generated by the Japanese Geo Research Institute (GRI). Finally, METIS also promotes two new opensource tools, one implementing an improved version of the Otarola 3D stochastic ground motion simulation method (Otarola et al., 2016; Ruiz et al., 2018), and the another one implementing the Irikura recipe and developed by EDF (Saint Mard, 2019).

Within this report, section 1 is the introduction, section 2 describes the validation and verification strategies agreed on in a preliminary phase of this work and applied to METIS case study synthetic database. In particular a battery of tests to assess the appropriateness of synthetic and recorded ground motion from both a seismological and engineering point of view is presented.

Section 3 describes a set of ground motion simulation methods analysed in this work. The following approaches are analysed:

- Irikura recipe with EGF
- 3D Stochastic physics-based approach
- Hybrid approach combining NGF and stochastic model for higher frequencies
- Recorded ground motion/EGF corrected for site response effects using spectral decomposition (the first modifies records to create a rock motion database the second is EGF-based ground motion simulation technique later on called Seister approach)

We discuss possible applications and provide advantages and disadvantages for each of the 5 methods and approaches. Details and further analysis of the stochastic ground motion database can also be found in METIS D5.1. Eventually, we provide a summary of the different source, propagation and site models used in the 5 ground motion simulation or modification techniques.

In section 4, we assess approaches to assemble the database of synthetic ground motions for METIS case study using the stochastic ground motion simulation methodology, fully described in (Alvarez et al., 2022b) and an example application of the Seister approach.

Conclusions and perspectives are given in section 5.

2.Validation and Verification (V&V) strategies

Development of Ground motion simulation methodologies (GMSM) has been an active research field due to their promising capacity to overcome the inherent limitations of availability of real records (e.g., Graves and Pitarka, 2010; Atkinson et al., 2010). However, in order to confidently use ground motion simulations in hazard and seismic risk studies, issues such as verification, validation, robustness and transparency must be properly addressed.

The verification of the GMSM refers to the appropriate functioning of the computer programs employed to conduct the simulations. Validation essentially refers to the quantitative evaluation of the accuracy of the GMSM to model an observation (Bijelee et al., 2014). Robustness is directly related to the epistemic uncertainty associated to the modelling of the ground motion and, finally, transparency refers to the reproducibility of results by users other than the author of the GMSM.

Overall, authors have conducted validations of GMSM by comparing reference and homologue simulated ground motions in terms of: (a) Intensity Measures (IMs), (b) Engineering Demand Parameters (EDPs), or (c) A combination of both. In the majority of cases, comparisons are

conducted accepting or discarding null hypothesis regarding the statistical similarity of the reference and simulated populations of EDPs or IMs.

Validation via IMs, also referred as seismological validations, has been traditionally used in studies aiming to introduce or improve GSM (e.g. Otarola et al., 2016; Motazedian et al., 2005). The Southern California Earthquake Center (SCEC) has also set up a platform to implement such a validation scheme for a collection of broadband simulation methods (SRL special focus section on broadband platform validation: Goulet et al., 2015; Dreger and Jordan, 2015). Due to its wide-spread use by engineers, the most commonly employed validation IM is the spectral acceleration at several periods of interest. Several other IMs have also been used in past studies, such as PGV, PGD, Arias Intensity, significant duration, etc. Additionally, other researchers proposed validation schemes including proxies for key features of recorded ground motions, such as the evolutionary character of the frequency content (Rezaeian et al., 2015), or signal polarization, non-linear response and correlation of spectral accelerations in response spectra (Burks et al., 2014), etc.

Figure 3 and **Figure 4** developed in task 4.5 of WP4 show schematics of such validations procedures with respect to past events and ground motion models, respectively.

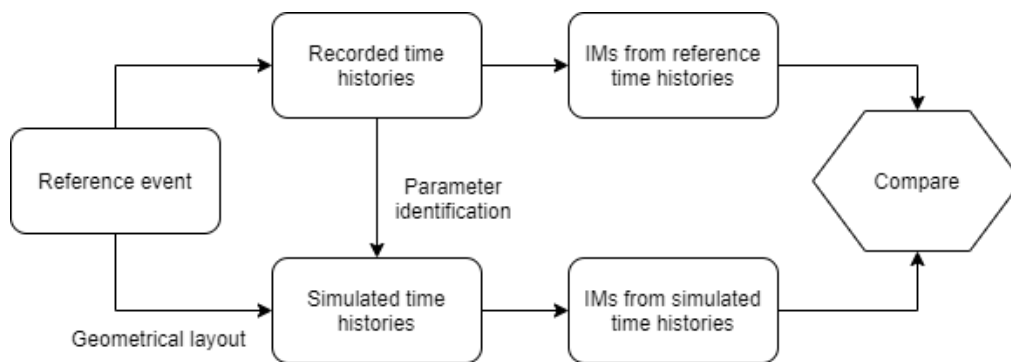


Figure 3: Schematic Procedure for the validation of ground motion simulation methodologies to recorded events.

Several authors have based their validation proposals on the comparison of EDPs, obtained from the time history analysis of structural models. These engineering oriented methods basically try to quantify whether the response of a structure to simulated ground motions waveforms is statistically equivalent to the ones obtained using real ground motions from a given set of records (Atkinson and Goda 2010; Burks et al. 2015; Dreger et al. 2015; Galasso et al. 2012; Galasso et al. 2013; Goda et al. 2015; Goulet et al. 2014; Iervolino et al. 2010; Rezaeian et al. 2015; Tsioulou et al. 2019; Zhong et al. 2021). Single degree of freedom (SDoF) systems are often used as a proxy for complex structures whose modal response could be described by one fundamental vibration period. However, these validations could also be performed using more complex structures idealized as multi-degrees-of-freedom (MDoF), or with sophisticated structural models, allowing to assess the structural effect of period elongation and the evolution of the time histories frequency content **Figure 5** shows an schematic of the validation procedure to structural response (measured in terms of Engineering Demand Parameters), proposed in WP4.

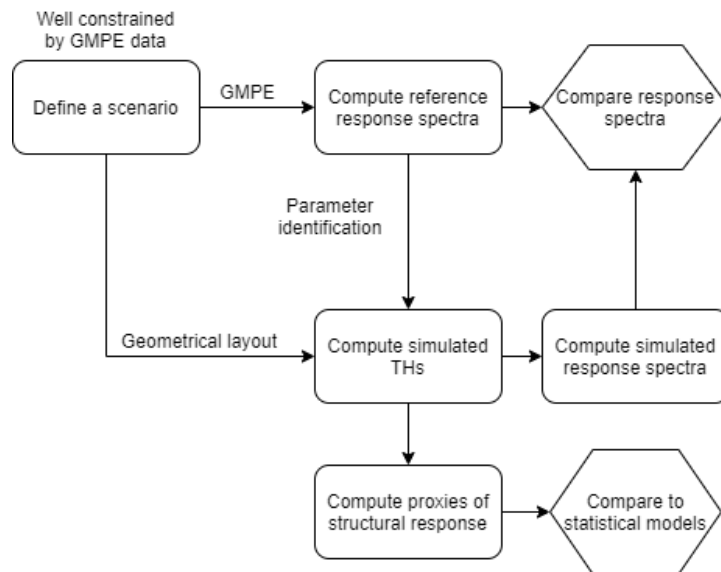


Figure 4:. Schematic Procedure for the validation of ground motion simulation methodologies to Ground Motion Models.

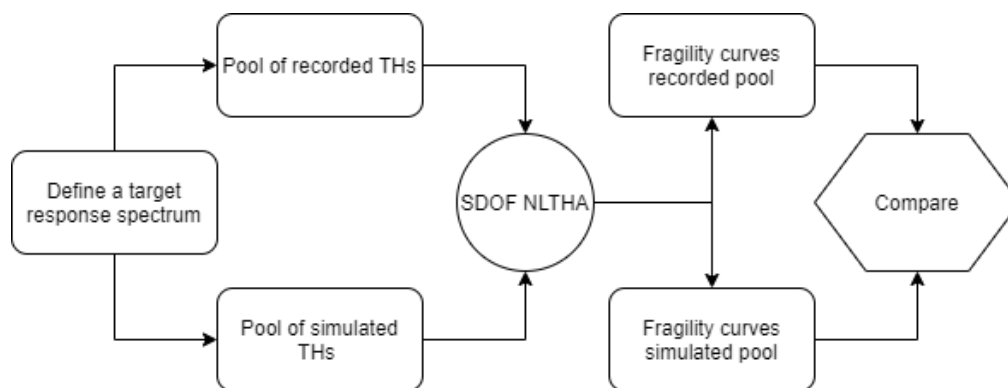


Figure 5: Schematic Procedure for the validation of ground motion simulation methodologies to Engineering Demand Parameters

Despite these validations, several issues have been found in the validation of GSM for applications oriented towards the prediction of future earthquakes. For example, previous efforts such as SCEC reported inconsistent median results from the predictions of different GSM, thus affecting the robustness of the simulations. Additionally, variability of simulated ground motions has not been properly addressed in the past, as inconsistencies have been noticed when comparing results from different GSM with empirical ground motion models GMMs. To address these issues, authors such as Razafindrakoto et al., (2021) have proposed validation procedures comparing the distributions of different residuals (inter/intra-event) computed by means of synthetic catalogues of ground motions realistically generated with respect to the seismicity of a studied area.

With this context in mind, the application of the full V&V strategy to the different ground-motion simulation approaches is out of the scope of the METIS project. The following 3 procedures for the validation of ground motion simulation methodologies are proposed and applied, at least partly, to candidate databases in WP4 and WP5:



- validation to recorded events,
- validation to Ground Motion Models,
- validation to Engineering Demand Parameters

It is assumed that the codes considered here have been sufficiently verified elsewhere. In this report, it is our aim to provide a few elements on validation and add example applications to illustrate the practical implementation and possible issues.

3. Ground motion simulation methodologies

The following sub-sections describe the ground motion simulation methods considered in METIS in more detail, furthermore, they provide input on V&V and example applications. Additionally, advantages and disadvantages of the herein considered GMSM are discussed.

3.1. Irikura recipe with empirical Green's functions (EGF)

3.1.1. Methodology

The Irikura recipe is one of the ground motion simulation methodologies based on recent findings from earthquake source physics in seismology and structural damage mechanisms in earthquake engineering (Irikura and Miyake, 2011). It was applied worldwide for to simulate large crustal earthquakes (Irikura et al. 2004), and widely used in Japan for seismic safety evaluations of nuclear power plants (IAEA 2015). The Irikura recipe introduces heterogeneity in source description by the characterized source model consisting of one or plural multiple asperity areas (Strong Motion Generation Area: SMGA) that is patches with a uniform slip velocity inside the rupture area, which allows simulating the accurate ground motions including the contents of high frequency of large earthquakes and large damage pulses. The Irikura recipe stands on several concepts of a kinematic methodology describing the rupture as a function of space and time.

The characterized source model in the Irikura recipe is particularly useful in prediction cases as where we do not know the appropriate values of several value of parameters are not known. The methodology is built based on theoretical (Eshelby 1957 among others) and empirical scaling relations (Somerville et al. 1999 among others) and allows estimating three source parameters such as outer (total fault area), inner (asperity area / SMGA), and extra fault parameters (**Figure 6**). In the last several decades, strong ground motion simulations using the recipe have also succeeded in reproducing observed broadband strong ground motion (e.g., Morikawa et al. 2008). Also, many researchers have investigated the kinematic source models and SMGA models for past large crustal earthquakes, and have validated the scaling relationships, which are used in the recipe.

For both past and future earthquakes, the empirical Green's function (EGF) method has been often applied to simulate the ground motion based on the characterized source model. This method uses a record of small events, such as an aftershock, as the EGF that contains useful information about the media from the source to site. The idea is to sum up the correct number of EGF in space and time, in order to obtain the acceleration from a larger event, following the self-similarity relations (Kanamori and Anderson, 1975) between small and large earthquakes. This technique has certain limitations, such as for example artificial periodicity and intermediate-frequency underestimation due to a uniform time shift in the summation scheme. Having identified these limitations, Irikura (1986) and Irikura and Kamae (1994) proposed a new summation scheme and subfaults repartition to avoid these numerical issues. The resultant workflow after these modifications is illustrated in **Figure 6**.

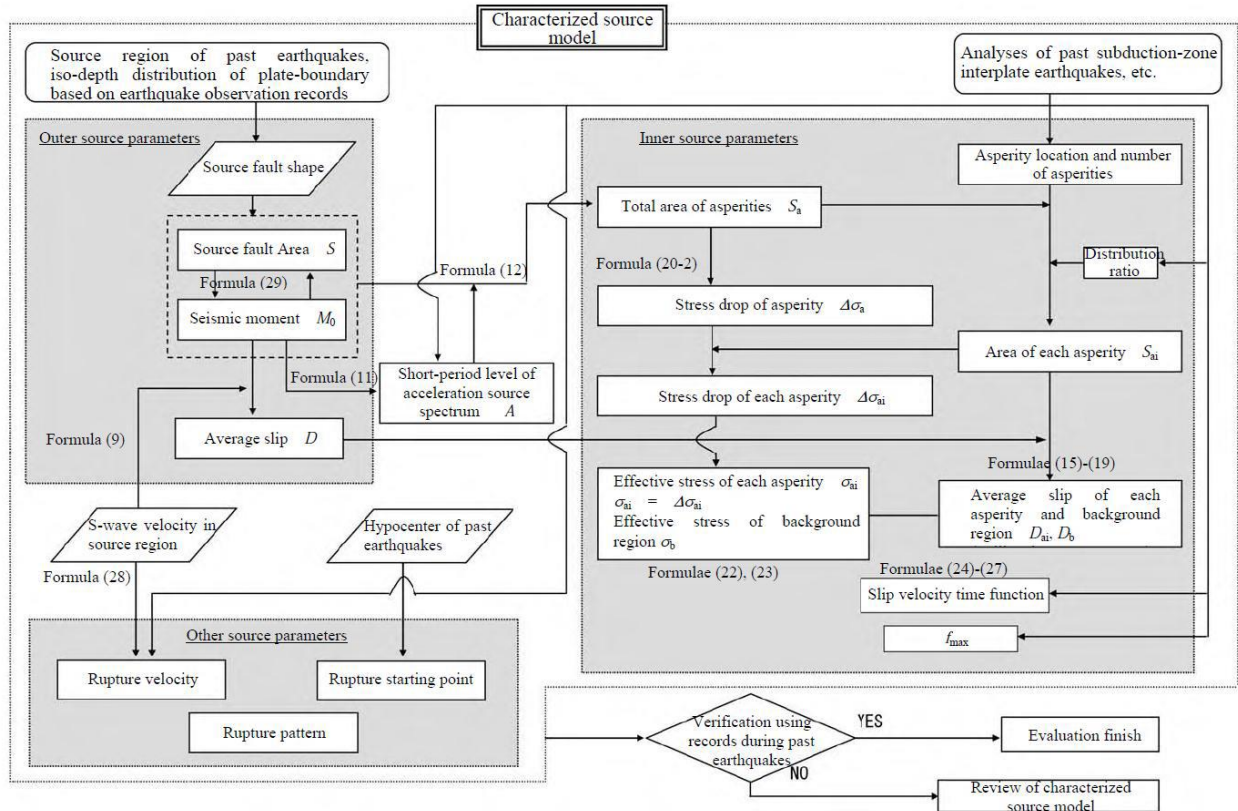


Figure 6: Flowchart of source characterization following the Irikura recipe (IAFA, 2015)

3.1.2. Validation/application for KK NPP case study

The 2007 Chuetsu-oki earthquake (Mw 6.6) occurred approximately 15 km off the west coast of the Niigata prefecture, in Honshu Island, Japan. This earthquake, causing strong ground motions at the nuclear power plant sites in Japan, is one of the largest recorded crustal events. The mainshock of this event resulted in peak ground motion accelerations (PGA) above 500 cm/s². These high-amplitude IMs were recorded at different sites, including the Kashiwazaki-Kariwa Nuclear Power Plant (KK NPP) site located 10 km away from the source fault of the mainshock. At these near-source stations, the observed large PGAs and PGVs exceeded the average ground motion that is expected by the Japanese Ground Motion Model proposed by Si and Midorikawa (1999) (see right panel in **Figure 7**).

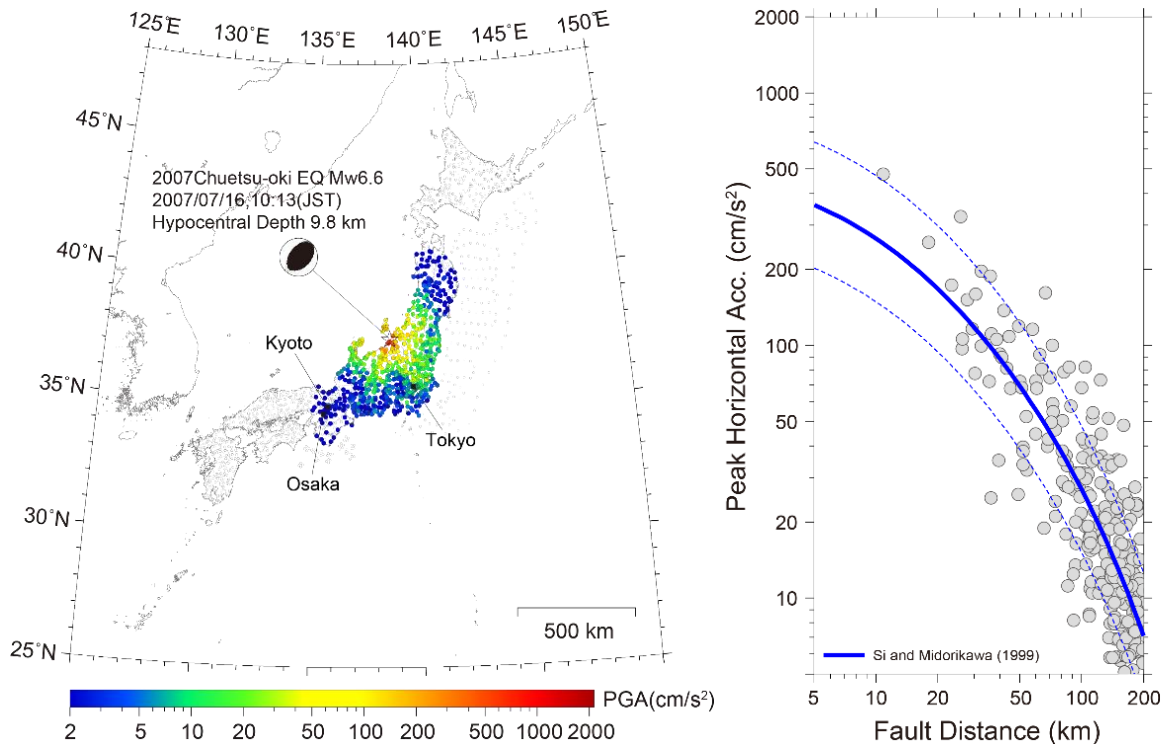


Figure 7: (Left) Distribution of PGAs registered at different stations for the main-shock of the 2007 Chuetsu-oki earthquake. (Right) Attenuation of PGA with respect to distance to source for the main-shock of the 2007 Chuetsu-oki earthquake.

The validation of the Strong Motion Generation Area (SMGA) model for the 2007 Chuetsu-oki earthquake was conducted using the EGF method to simulate the observed ground motions at the KK NPP. The records of a Mw4.4 aftershock occurring close to the hypocenter of the mainshock were used as the EGFs (see **Figure 8**). The best parameters (i.e., size of the SMGA, rupture velocity, rise time, and relative rupture starting point inside the SMGA) were estimated through the forward ground motion simulation in the frequency range 0.2-10 Hz. As shown in **Figure 8**, the preferred source model with three SMGA patches reproduced well the three pulses observed at the near-source KKNPP stations (KKN1R2, KKN5R2, and KKNSG4). We also simulated ground motions at 18 stations around the source area, and compared their response spectra with the ones actually recorded for the main-shock. **Figure 9** shows the obtained results, where a good match between simulated and recorded ground motions may be observed.

The stress drops of the preferred SMGA model were estimated between 19.2 and 38.2 MPa. These are relatively larger than the average expected values for Japanese crustal events, thus explaining the larger observed ground motions with respect to the empirical GMMs. The robustness and uncertainties in the SMGA parameters are needed to be discussed in future works because there is still variability of the location, rupture starting point, and stress drop between the SMGA models. Also, it is necessary to compare our SMGA model with the other kinematic and/or dynamic source models, to deepen the discussion of the broadband ground motion generation process.

The results in this section have been computed with GRI in-house software.

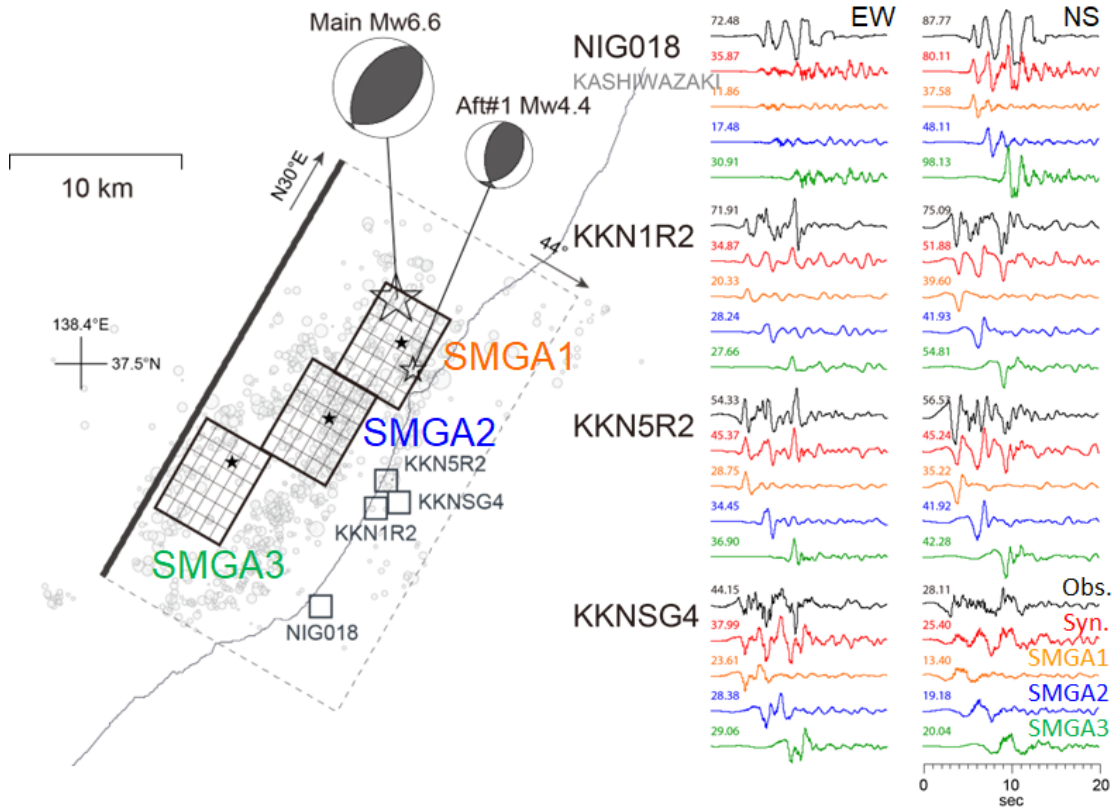


Figure 8: (Left) Map view of preferred SMGA model. The rupture starting point of the SMGA are represented by the small solid star. Large and small open stars indicate the epicentres of mainshock and the EGF event (Aftershock) with their moment tensor solutions. (Right) Comparisons of velocity waveforms in the EW and NS components at near-source stations between observation (black) and simulation (red) in 0.2-10 Hz. Orange, blue, and green mean the simulation from each SMGA1, 2, and 3, respectively. The maximum amplitude of the waveforms is shown above each trace in cm/s.

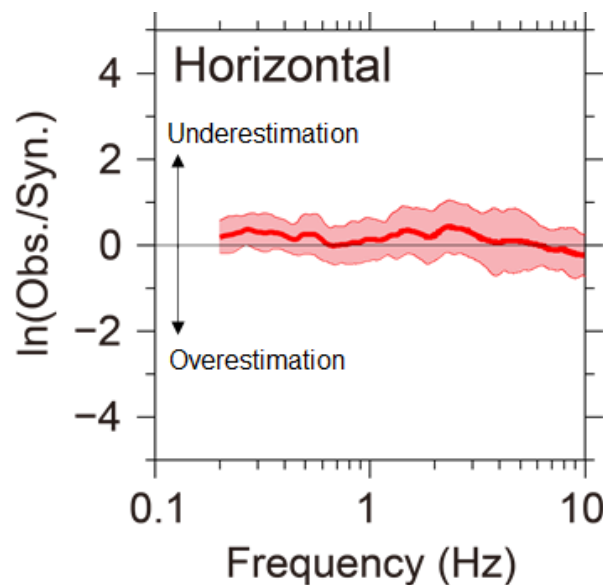


Figure 9: Natural logarithm of pseudo velocity response spectra ratio in the horizontal component between the observation and simulation. The thick and thin red lines show the mean and standard deviation for 18 stations in and around the source area, respectively.



3.1.3. Advantages/disadvantages of the approach for engineering applications

The advantage of the recipe relies in the simplicity of its application. The recipe provides the quantitative source modeling method for specific earthquakes scenarios, even when data to characterize the fault is missing, which is useful in low-to-moderate seismic area such as France and other stable parts of Europe. The recipe also has an advantage over randomized source models in that it can simulate rupture directivity pulses, which enhance response spectra. A disadvantage in use of source modeling by the recipe is the difficulty to specify the number of SMGAs and their locations when no historical records exist.

A clear advantage of the EGF simulation method is what we directly know the Green's function in a broadband frequency range using the observed records of small earthquakes. One disadvantage relies on the availability of EGF. Indeed, in low-to-moderate seismic areas, such as EU countries with NPP, it is not obvious to have small, recorded events and large enough to have a good noise-signal ratio close to the site of interest. Also, the EGF does not allow to represent non-linearity phenomenon in site effects, which can be considerable in case of large earthquakes.

Finally, the herein discussed method includes, by definition, site effects experienced by the considered EGFs, therefore it may not be the best option when the goal is the creation of a synthetic rock motion database for engineering applications. This drawback, however, could be overcome by the manipulation of the EGF as suggested in the approaches proposed by Pilz et al (section 3.4) and in the Seister approach (section 3.5). In addition, the ground motion can be defined with a probabilistic model to account for different slip configurations.

3.2. Hybrid stochastic method using the SCEC platform

3.2.1. Methodology

The simulation approach adopted in this section is the one of Graves and Pitarka (2015) (GP method) as implemented in the SCEC BBP (v.17.3) and tailored for Europe. It is a hybrid simulation approach based on frequency-wavenumber Green's functions for low frequency and a semi-stochastic ray theory technique for high frequency, that sums the response for an array of sub faults used to represent the seismic source. The response is generated considering the contribution of source, path, and site effects. These separate low-and high-frequency motions are, then, combined at a transition frequency of 1 Hz to produce three component broadband time series through a matching filter process.

To adapt the method to the European context, the following modifications have been incorporated (Razafindrakoto et al., 2021):

- 1) calibration of regional high frequency attenuation properties using recent GIT results.
- 2) incorporation of a local velocity model.

In addition, the hybrid approach has been modified to account for P-waves in the high frequency computation. This is achieved by a modification of the modulating function to introduce the P-wave amplitude. The earthquake source in the GP method consists of a kinematic rupture model characterized by a spatio-temporal evolution of the rupture.

3.2.2. Example application and validation for Central Italy and Rhine Graben case

In this section, we present two validation approaches: (a) standard validation using past earthquake and (b) validation in terms of ground motion variability.

a) Validation using past earthquake: Applications to central Italy

This section presents the results of ground motion simulations for the 2016 Mw6.2 Amatrice earthquake, as an illustrative example applicability of the GP method to Central Italy, an active area in Europe. This event struck central Italy on August 24th at 01:36 UTC, causing 299 fatalities (Azzaro et al., 2016)

Various kinematic rupture models have been proposed for the Mw 6.2 Amatrice earthquake (e.g., Pizzi et al., 2017). This study utilizes an earthquake source consisting of a finite rupture of 26km x 15km whose geometry and dimension are based on Chiaraluce et al. (2016). The rupture process, on the other hand, was generated using the stochastic slip generator of Graves and Pitarka (2016). In terms of HF motion, using an average velocity model appropriate for the area to compute Green's function, with kappa value of 0.017s (Pilz et al., 2021). We also adopt values of the stress parameter computed from spectral decomposition of Bindi & Kotha (2020).

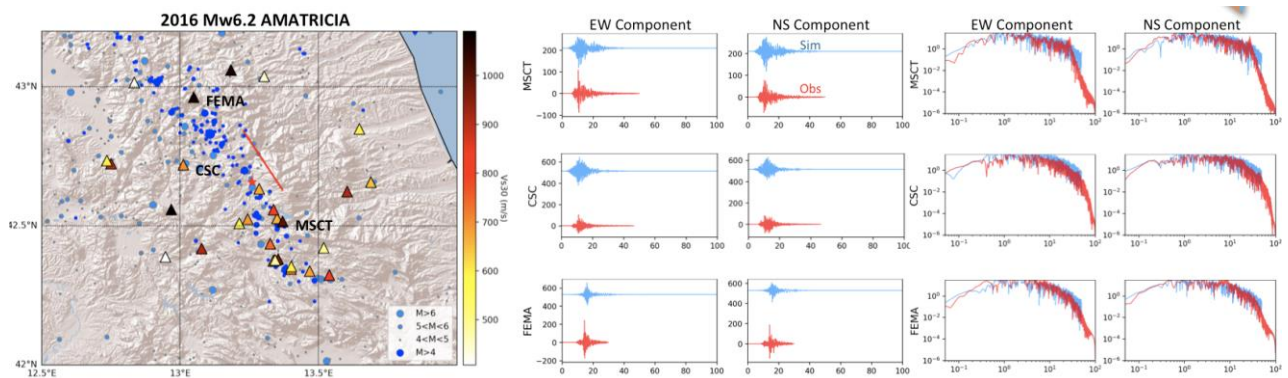


Figure 10: Summary of the simulation results of the 2016 Amatrice earthquake: acceleration time series with the corresponding Fourier spectra.

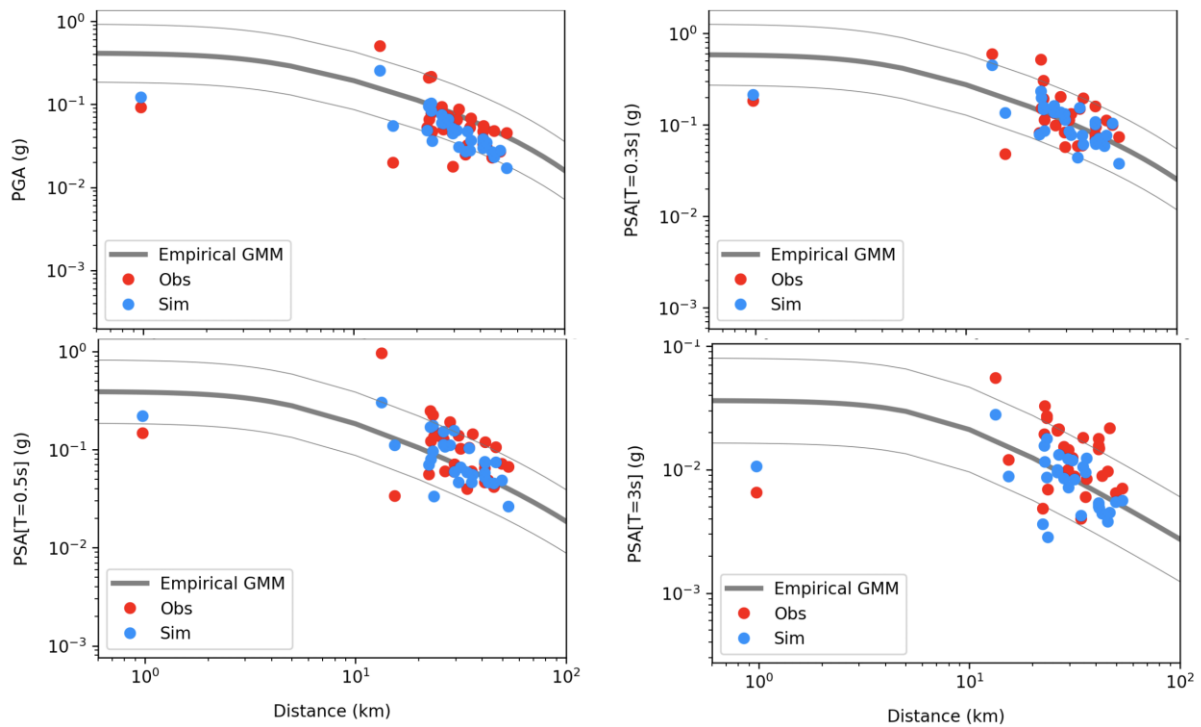


Figure 11: Comparison of the recorded, simulation and the empirical ground motion model introduced in Kotha et al., (2018)

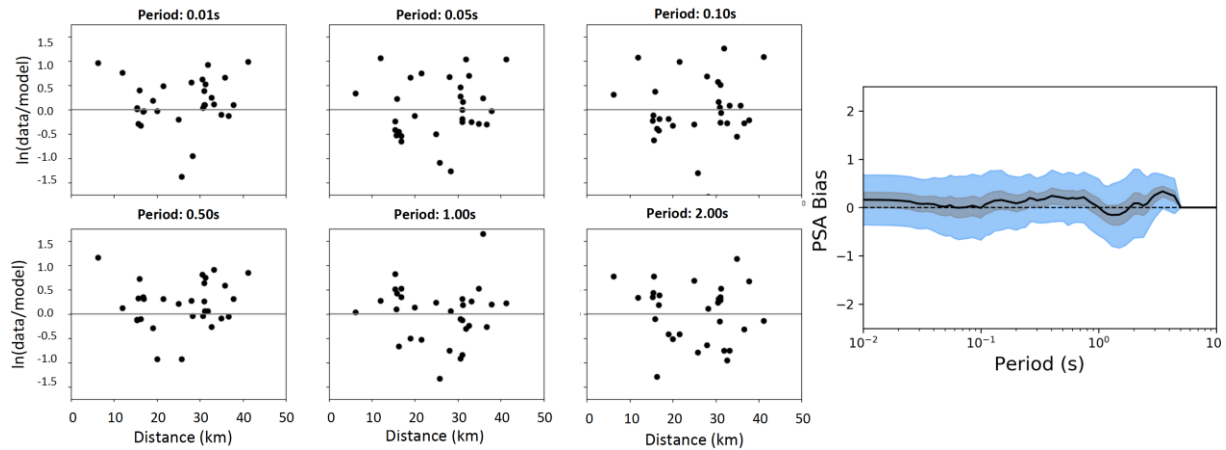


Figure 12: Quantitative comparison between data and model

Figure 10 compares the observed and simulated acceleration time series at three representative rock sites. It illustrates that the arrival times are relatively consistent between simulated and observed ground motions, although, the simulations show more variability in amplitudes. To examine further the performance of these methods, we also observe, in **Figure 11**, that the simulated PGA and PSA values are consistent with the observations, and with the overall distance attenuation from the empirical GMMs. The simulated PGA and PSA values are consistent with the observations, and their scaling with distance consistent with the attenuation from the empirical GMM.

To quantify the misfit between the observed and simulated ground motions, we compute residuals as the difference between the logarithm of the observed and simulated intensity measure. **Figure 12** shows the PSA results. The mean value of the residuals oscillates near zero (horizontal dotted line in the right panel of **Figure 12**). Simulations reproduce the overall amplitude and duration of the observed ground motion and adopting parameters from spectral decomposition gives well calibrated time histories.

b) Validation in terms of variability - Application to Rhine graben

In this section, we will discuss how the distribution of model parameters control ground-motion variability, and whether the simulations are consistent with empirical ground motion model in terms of both median and standard deviation.

In this regard, we compute a database with simulated ground motion time histories based on a stochastic catalogue of ruptures (i.e., a set of earthquake scenarios, left panel in **Figure 13**) that could occur in the Rhine Graben area. The detailed description of the database construction and resulting time histories is available in Razafindrakoto et al. (2022). To better understand the origins of the ground motion variability, we performed five experiments highlighting the effect of stress parameters and velocity structure.

In addition to the stochastic catalogue, we also consider fault-specific earthquake scenarios (see right panel in **Figure 13**), for the Erft fault system, located about 15km west of the city of Cologne (Lower Rhine Graben), among the fastest slipping systems in the area (Basilic et al., 2013). The rupture in this case has a strike, dip, and rake of 147° , 57.5° and 87° respectively (Grunthal et al., 2018). Among other studies, Pilz et al. (2021) used this fault system to evaluate the potential effect and seismic risk related to an Mw6.5 earthquake scenario in the area. To build the rupture sets, the Erft fault is treated as a "simple fault type" in the OpenQuake Engine (Pagani et al., 2014), so the uncertainty in the location of future ruptures is accounted for by enumerating, for each magnitude, the different possible areas on the fault surface that a rupture corresponding to that magnitude could occur. First, the fault segment that ruptures are sampled across a uniformly spaced mesh of 2km

along the surface and down dip. Then, we randomly select 100 scenarios samples (from all the ruptures) for the simulation (see **Figure 13**).

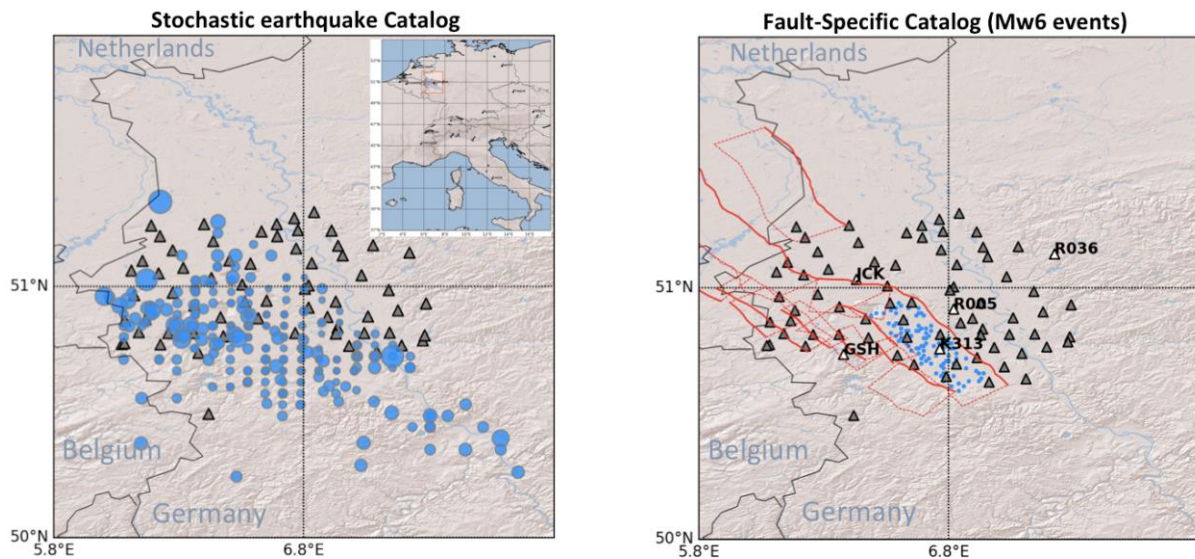


Figure 13: (Left panel) Location of earthquake scenarios (blue dots), and the stations used to perform the simulations (gray triangles), in the Rhine Graben area from an stochastic catalogue, and (right panel) fault specific catalogue.

Simulations are performed adopting the GP method. The location, magnitude, and focal mechanism (dip, strike, rake) are obtained from each rupture in the stochastic catalogue. The fault dimension is defined based on the scaling relationship of Leonard (2014), and the rupture process is generated using the stochastic slip generator of Graves and Pitarka (2016). In such a slip generator, the considered slip-rate function is a Kostrov-like pulse (Liu et al., 2006), and the average rupture speed is about 80% of the local shear-wave velocity. Such rupture speed is further reduced by a factor of 0.6 for depths less than 5 km, to account for the shallow crustal weak- zone in surface-rupturing events. Another critical element for simulation is the crustal velocity structure that is used to compute Green's function. This study uses velocity models derived from the deep seismic refraction/wide-angle reflection profile nearest to the Rhine Graben area. **Figure 14** shows an example of the simulation results for two scenarios along the Erft fault system. As expected, large amplitudes are seen close to the source and decay moving away from source.

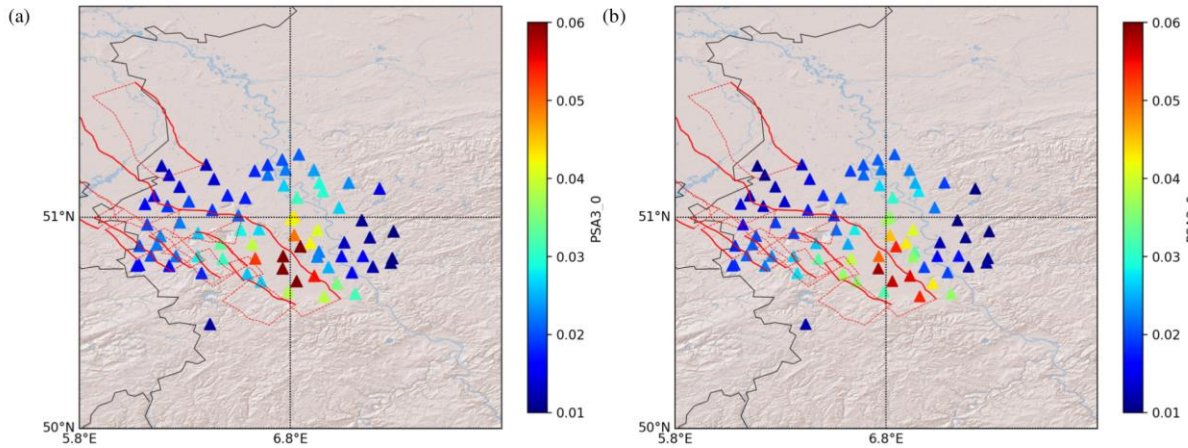


Figure 14: Simulated ground motion in terms of spectral acceleration at $T=3s$ for 2 scenarios

To investigate the ground motion variability, we analyze the residuals between the simulation and the empirical GMM prediction of Kotha et al. (2020). Then, such residuals are decomposed into various components associated with ground motion variability (between-event, within-event, and the remaining terms) through a random-effects splitting algorithm (e.g., Bates et al., 2015; Stafford, 2014).

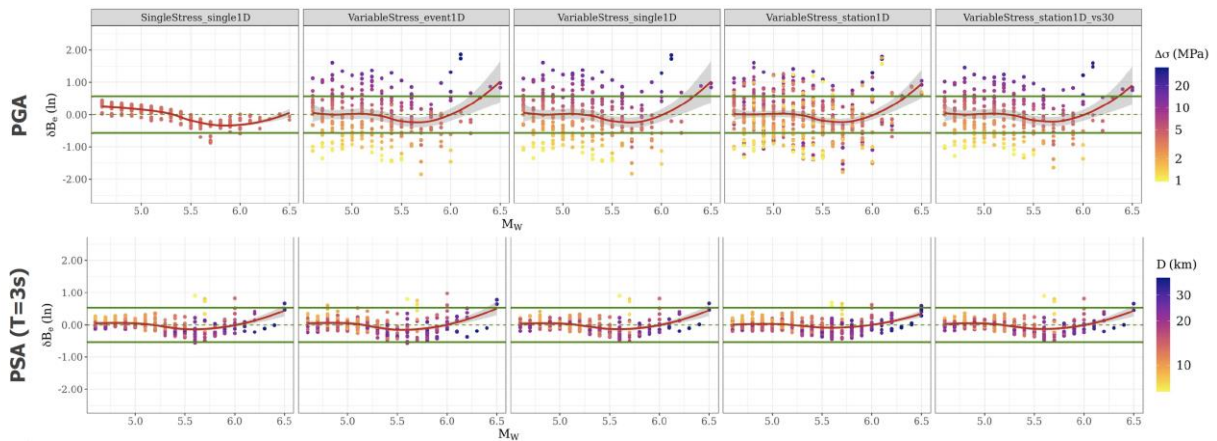


Figure 15: Between-event term residuals for five sets of simulations.

Figure 15 illustrates the between-event (dBe) computed for five experiments with the goal of highlighting the sensitivity of stress parameters and velocity structure on ground motion variability. All the stochastic catalogue experiments show that dBe fluctuates around zero for $M_w < 6$, then increases with magnitude for $M_w > 6$. This increase becomes steeper as we incorporate variability in stress parameters. We also observe that the adopted magnitude-dependent stress-drop from spectral decomposition is clearly mapped onto the trends of the between-event residuals for PGA and $PSA(T=0.5s)$. Therefore, it is an essential metric that can be used to calibrate/validate the stress parameters of the earthquake scenario in the simulations to ensure a consistent resulting between-event residual with regional data.

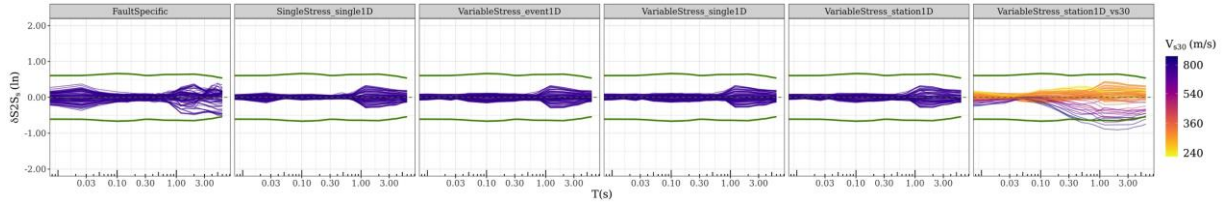


Figure 16: Within-event terms

In terms of within-event terms, **Figure 16** shows that $\delta S2S$ are centered around zero, and have relatively low variability, nearly zero, compared to that predicted by empirical GMMs, about 0.6. This minimal within-event term is expected because we are using a 1D velocity model.

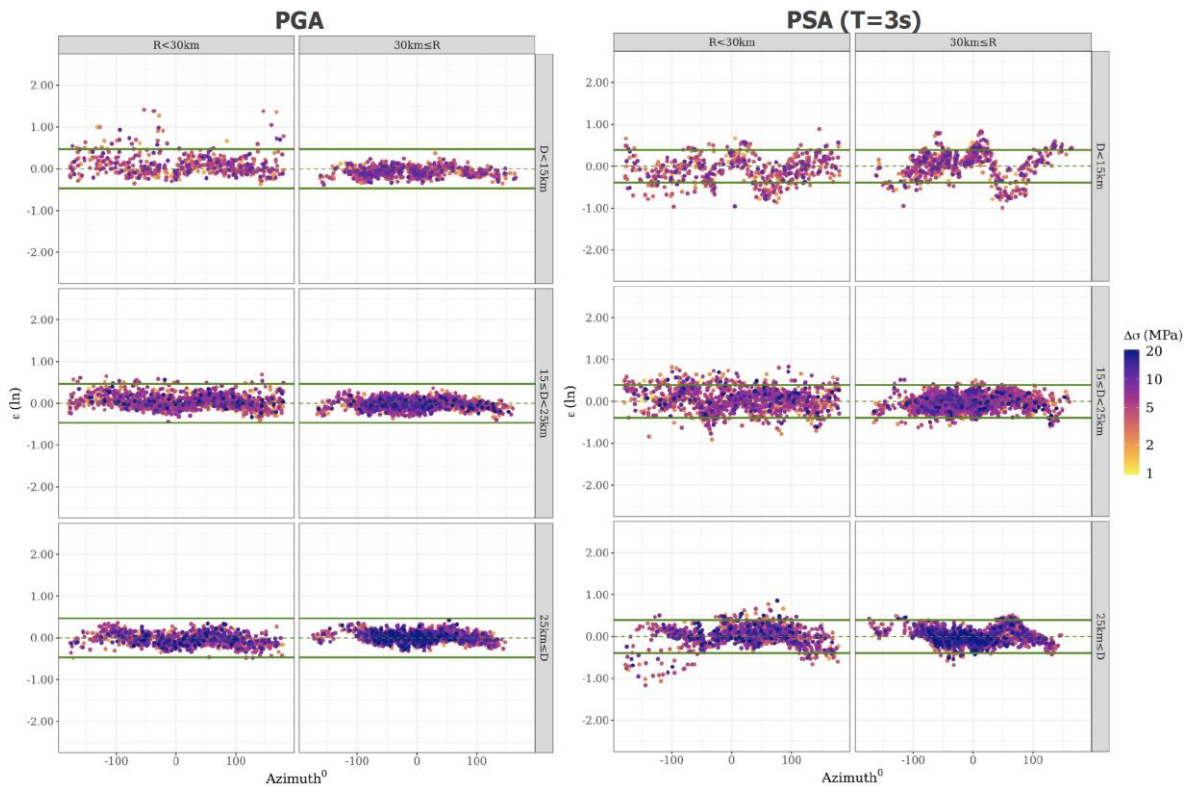


Figure 17: Leftover residual as a function of azimuth, depth, and stress parameters for fault-specific case: (a) PGA, (b) PSA(T=3s)

The leftover residual, ϵ , represents variabilities that are not included in the random effects δBe and $\delta S2S$, such as the randomness in the system and physical phenomena not captured by these random effects. **Figure 17** illustrate the generated ϵ as a function of depth, distance, azimuth, and stress parameters for PGA and PSA (T=3s) using the stochastic catalog and samples of ruptures from one specific fault system, respectively. We observe that for both cases that residuals ϵ are not random. They follow patterns depending on depth, distance, azimuth, and the choice of intensity measures. However, there is no striking dependency on the stress parameters. Given that these patterns are mainly at close distance and/or shallow depth, they are likely due to near-source effects (e.g., radiation pattern, rupture process), which are not well constrained for the empirical GMM.



3.2.3. Advantages/disadvantages of the approach for engineering applications

Among the existing simulation approaches, the GP method has proven its capacity to reliably simulate the broadband ground motion simulation at a specific area of study. This technique embraces the benefits of both the deterministic and semi-stochastic approaches at Low and high frequency ranges, respectively. The GP approach could be used to simulate ground motion at sites with various conditions (e.g., rock, sediments), as it adopts an empirical Vs30-based approach to incorporate the site amplification at low- and high-frequency. Alternative approaches can also be used to model site response in GP ground motion simulations, such as explicitly model nonlinear site response (e.g., Pilz et al. 2020, De la Torre et al. 2020), and the use of site response from spectral decomposition approach or GIT (e.g., Razafindrakoto et al. 2021).

The findings in this study also support the potential of incorporating scenario-based ground-motion simulations for the characterization of seismic hazard and other engineering applications. The validation carried out showed that we could confidently use the approach to generate a population of time histories (ground motion database) for hazard and risk analyses, and to complement the data in the surrounding area that lack seismic stations and recordings. However, the computational effort remains an issue for the creation of large databases for ground motion selection.

It is important to note that this study adopts a 1D velocity structure, which lead to an underestimation of the within-event terms from homogeneous site condition. Aside from that, the chosen transition frequency is 1Hz (see Graves & Pitarka, 2016). This choice relies on the knowledge of the velocity structure and the source complexity. Therefore, the modeler should ensure that the velocity Structure and the source are able to generate sufficient HF for pushing this transition to higher frequency.

3.3. 3D Stochastic simulation based on Otarola method

3.3.1. Methodology

The ground motion simulation method presented in this section is a modified version of the stochastic technique introduced in Otarola & Ruiz, (2016) and Ruiz et al., (2018), and modified to include a more realistic representation of the source and the inter-frequency correlation structure of the spectral amplitudes.

The stochastic ground motion simulation method proposed in Otarola & Ruiz, (2016) and Ruiz et al., (2018) computes time histories in the frequency domain and model the Fourier Amplitude Spectru (FAS) as a convolution of modulated noise with a random phase and a mean ground motion spectrum:

$$FAS = U(f, r, M_0) \sqrt{S_0} \quad (1)$$

Where U is the mean simulated ground motion spectrum, S_0 is the white noise with normalized power spectral density, f is the frequency, r is the source-receiver distance, and M_0 is the source seismic moment. Considering a finite-source model, where the source is discretized into an array of point-sources, time histories are constructed as the lagged summation of the individual sub faults contributions, (Atkinson et al., 2009; Beresnev & Atkinson, 1997; Motazedian & Atkinson, 2005). The definition of the mean simulated ground motion spectrum, for wave type w (P, SV, and SH), sub-source i and component d (vertical, radial, and tangential) is shown in the following equation:

$$U_{i,d}^w(f, r_i, M_{0i}) = C_{i,d}^w(M_{0i}) S_i^w(f) A_i^w(r_i, f) Z_{i,d}^w(f) \quad (2)$$

Where $C_{i,d}^w$ is the scaling constant, $S_i^w(f)$ represents the source, $A_i^w(r_i, f)$ the propagation (attenuation due to the path) and $Z_{i,d}^w(f)$ the site-specific effects component of the simulated ground

motion spectrum. The full description of the formulation of each of these components can be found in Alvarez (2022).

The phase of the simulated ground motions is included by mean of the band limited Gaussian white noise with finite duration. The duration of the ground motion, on the other hand, is modelled considering a source related component (linked to the rise time of the assumed source model), and a propagation component (related to the elongation of the signal with respect to the distance from the source). A modulating function is applied to the white noise with the intention to include the characteristic temporal non-stationary nature of ground motion time series. The Saragoni and Hart (1973) modulating function, $\omega(t, e, \eta, t_\eta)$, shown in equation (3) is often considered in stochastic simulation methods, e.g., Otarola et al., (2016) and Ruiz et al., (2018), and was also considered in this study.

$$\omega(t, e, \eta, t_\eta) = a \left(\frac{t}{t_\eta} \right)^b \exp \left(-c \left(\frac{t}{t_\eta} \right) \right) \quad (3)$$

Where e and η are parameters defining the shape of the function, $a = \exp(1)/e$, $b = -e \ln(\eta)/(1 + e(\ln(e)-1))$, $c = b/e$, $t_\eta = f_{Tgm} \cdot T_{gm}$. T_{gm} is the duration of the signal for the computation of the window function, and f_{Tgm} is a factor modeling the elongation of the windows. Previous implementations of this modulating function have considered different combinations of parameters. These, however, are often adjusted for matching reference signals, e.g., Otarola et al., (2016) and Ruiz et al., (2018)

The herein presented method differs from previous stochastic methods such as those considered in Beresnev & Atkinson, (1997); Boore, (1983), (2003); Motazedian & Atkinson, (2005), not only by computing the whole body-wave spectra, but also for using a ray-like propagation of the seismic waves through a layered media (considering Snell's law to vary the incidence angle of the seismic rays coming from the source to the site). Finally, this methodology includes a postprocessing procedure to add the correlation structure between spectral amplitudes coming from the analysis of within-site residuals (Wang et al., 2019). More details on this procedure may be found in Alvarez (2022).

3.3.2. Validation for Japanese data - seismological tests

This section presents the results obtained by applying the 3D stochastic simulation technique within a ground motion prediction framework, i.e., by evaluating not only the correspondence of the simulated and predicted IMs, but also the capacity of this technique to reproduce the uncertainty associated through the consideration of the uncertainty of the input variables.

These validation procedures are in line with the ones discussed in Chapter 2 (Validation and Verification strategies) of this document and, specifically, with the comparison between simulations and recordings of past events and reference GMMs (see the schematics shown in

Figure 3 and

Figure 4).

The comparisons were conducted for a case study considering a generic earthquake scenario and valid Ground Motion Models as reference. In particular, the case study considered a magnitude 6.6 ($M_w = 6.6$) earthquake in the region of Niigata, Japan. In addition to this generic scenario, a real earthquake scenario, the 2004 M_w 6.6 Niigata earthquake, was considered as a reference for the test of the 3D stochastic simulation technique. Acknowledging that the main objective of this chapter is the assessment of the simulation technique for ground motion prediction purposes, i.e., in consideration of the uncertainty related to the predicted IMs, the intention of the case study is not to replicate the reference event, but rather the predictions given by valid GMMs for an event matching its causative features. The consideration of a reference event provides an actual observation to the comparisons of simulated and reference IMs, furthermore, it allows for the direct comparison of waveforms not currently available in GMMs. In the end, the herein compared reference predictions and simulation

share the main causative parameters with the reference event, i.e., magnitude, location of the hypocenter (latitude, longitude, and depth), and finally the points of observation, here considered through their location and site conditions (V_{s30}). All other aspects such as geometry of the fault, distribution of the slip and variables considered in the construction of the simulated ground motion spectrum were varied according to relationships and distributions found in the literature. More details may be found in Alvarez (2022).

The comparisons were focused on a series of stations matching the ranges of applicability of the simulation technique: minimizing the presence of surface waves (not explicitly modelled in the method), and the non-linear response of the soil. These conditions were approximated by considering stations with maximum hypocentral distance of 70 km, and for sites with a minimum average shear wave propagation velocity in the upper 30m of 500 m/s ($V_{s30} \geq 500$ m/s).

Figure 18a shows the location of the source model of the observed reference event, as reported in Asano & Iwata, (2009), and the location of the stations of interest with respect to the rupture. Additionally, the average shear wave velocity of the soil columns for each of the stations of interest is also shown in **Figure 18b**.

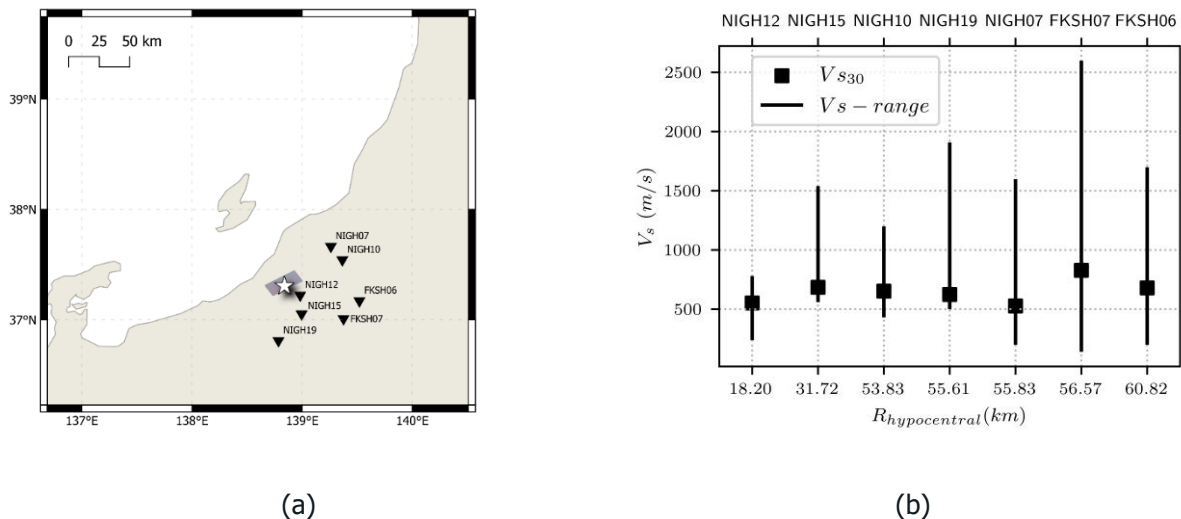


Figure 18: (a) – Projection of the rupture model of the observed reference event, and location of the stations of interest. (b) – Average Shear wave velocity for all stations of interest, where the point represents V_{s30} , the upper and lower end of the bars represent the maximum and minimum V_s of the soil columns of each station

The full description of the input for the ground motion simulation technique may be found in (Alvarez, 2022). A comparison of the simulated and observed FAS and acceleration time histories (for all stations of interest) may be consulted in Alvarez (2022). To allow for a description of the obtained results, **Figure 19** shows these comparisons for stations NIGH12 and FKSH06. The displayed simulated acceleration time histories correspond to the simulated realisation resulting in the median arias intensity (AI) of the Geometrical Mean of the horizontal component, AI_{GM} , of the simulated set. To facilitate the comparison, observed and simulated time histories were aligned at the instant where 1% of the maximum arias intensity is reached.

Overall, congruence between the observed and median simulated scenarios was observed, not only in terms of maximum amplitude, but also in the evolution of the amplitude over the duration of the ground motion. See for example **Figure 19**, where the arrival times of the observed and simulated wave packages are in synchrony for all components. This matching is more easily appreciated in

simulations for stations furthest from the source as the arrival of the different sub-source (in the finite fault model) contributions arrive with more prominent delays. The matching of acceleration waveforms was mainly attributed to the calibration of the modulating windows. This feature has been very rarely explored in the stochastic simulation of ground motions, more so for a finite-fault simulation scheme where the slip distribution and rupture propagation history play a key role in the construction of the time histories. The calibration procedure proposed in Alvarez (2022). resulted in a good correspondence of the overall waveforms (with respect to the observe event) and of the distribution of the energy over time, when compared to the AS16 reference model, (Afshari et al., 2016, see **Figure 20**).

The comparison of the Fourier Amplitude Spectra displayed a good agreement between the reference and the simulated ground motions. For example, **Figure 21** shows that the median simulated scenario captured the distinctive peak noticed in the reference event at 8 Hz for station FKSH06. To complement the evaluation of the frequency content, **Figure 22** and **Figure 23** show a comparison of the spectral accelerations at different periods of vibration for the geometrical mean of the horizontal components (GM) and the vertical (UD) component, respectively. These figures compare the predictions from a reference ground motion model, the simulated ground motions, and the observed spectral accelerations from the recorded time histories. For the comparison of the GM component, shown in **Figure 22**, the ground motion model proposed in Kotha et al., (2018) was considered as reference. Due to the availability of the information considered in the derivation of the model, the comparisons were conducted against to two different version of the ground motion model, an ergodic and a site-specific one. The ergodic estimation refers to a "regular" application of the ground motion model, where one considers that the variability in ground motion at a single site-source pair is the same as the variability in ground motion observed in a more global dataset, (al Atik et al., 2010). The site-specific version, on the other hand, considers the site-specific residuals ($\delta S2S_s$) for each specific station, obtained from the regressions performed for the construction of the ground motion model. **Figure 22** shows that the mean spectral accelerations computed from the simulated set fairly match the spectral content of the reference ground motion model. Specifically, good correspondence was found between the observed event, the ground motion model, and the simulated set for all stations when considering PGA (**Figure 22a**) and a period of vibration of 0.20s (**Figure 22b**). When considering longer periods of vibration, both the reference ground motion model and the simulated ground motions overestimated the observed event. However, simulations were consistent with the predictions, specifically for stations furthest from the source, see for example **Figure 22c** and **Figure 22d**. These differences are likely to be due to specific characteristics of the source of the reference event and therefore not adequately captured in the general representations considered in the ground motion simulation procedure.

The standard deviation from the simulated sets was estimated between the ergodic and site-specific estimations of the reference GMM for periods of vibration below 1.0s. In fact, the standard deviation of the simulated sets increases with the period of vibration for all considered stations, thus leading to believe that the increase in the uncertainty is directly linked to the epistemic modelling of the source and the overall simplistic modelling of the rupture. In fact, the high variability of the stress drop, used in the computation of the corner frequency (directly defining the energy content at low frequencies) affects the standard deviation in question. Alvarez (2022) provide a sensitivity analysis for the input variables of the simulation technique, here one can observe the clearly dominant effect of the stress drop in the mean and standard deviation of the simulated ground motions.

The comparison of spectral accelerations computed for the vertical component of the ground motions is shown in **Figure 23**. These comparisons considered only the ergodic application of the reference ground motion model due to the lack of the site-specific residuals. The results indicated that simulations overestimate the amplitude of the vertical component of the motion when compared to the considered reference model and the observed reference event. This observation was specifically true for stations furthest from the source, which indicates that the attenuation functions estimated from the GIT were a better approximation to the context of the region than those of the generic

values obtained from the literature. The overestimation of the vertical component may be due to different factors such as the simplistic approximation of the corner frequency of P-waves based on the ratio of propagation velocities at the depth of the sub-faults, (Otarola & Ruiz, 2016). Another cause may be the limitations of the model in the representation of phenomena such as the transformation of P to SV waves, and vice versa, due to the reflection of seismic waves at the interface of the layers of the velocity models. These limitations need to be further explored. Finally, the analysis of the compared standard deviations leads to the same conclusions as those obtained from the analysis of the horizontal components.

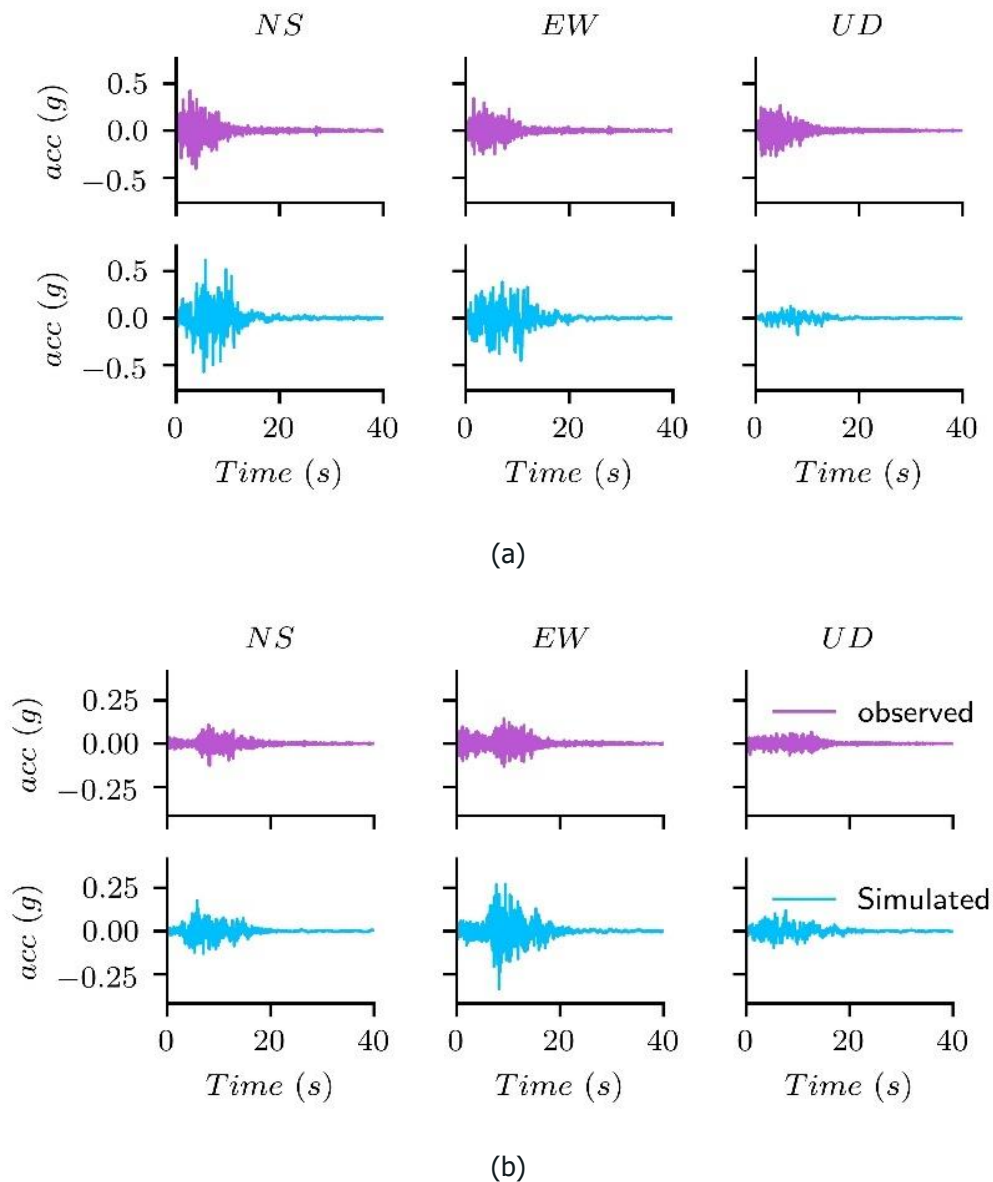


Figure 19:. Comparison between observed and simulated ground motions. Acceleration time histories aligned at the instant where 1% of the maximum arias intensity (AI) is reached for stations (a) – NIGH12 and (b) – FKSH06. The shown simulated scenarios correspond to the median AI of the GM component.

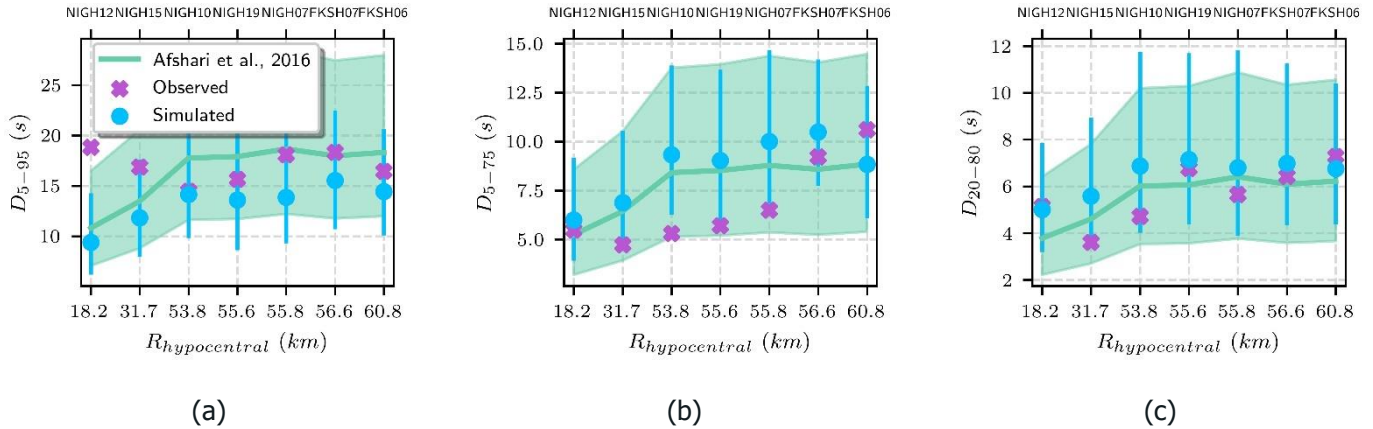


Figure 20:. Comparison of different significant durations for the stations of interest. Duration between (a) – 5%-95%, (b) – 5%-75%, and (c) – 20%-80% of the Arias intensity of the geometrical mean of the horizontal components. The shaded area and the bars represent the space between $\pm 1\sigma$ for the predictions considering the Afshari et al., (2016) and simulated models, respectively.

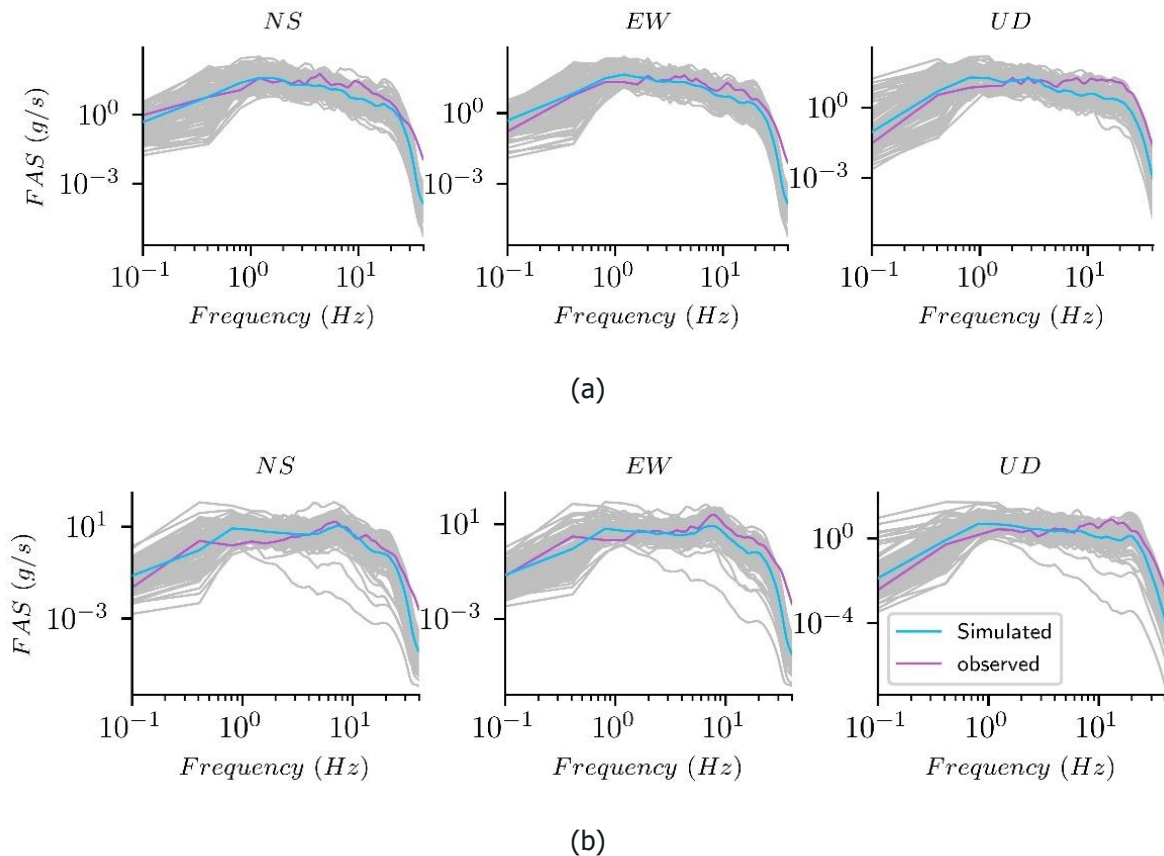


Figure 21:. Comparison between observed and simulated ground motions. Comparison of smoothed FAS, the grey lines correspond to individual simulations and the highlighted scenarios correspond to the median of the distribution (a) – NIGH12 and (b) – FKSH06.

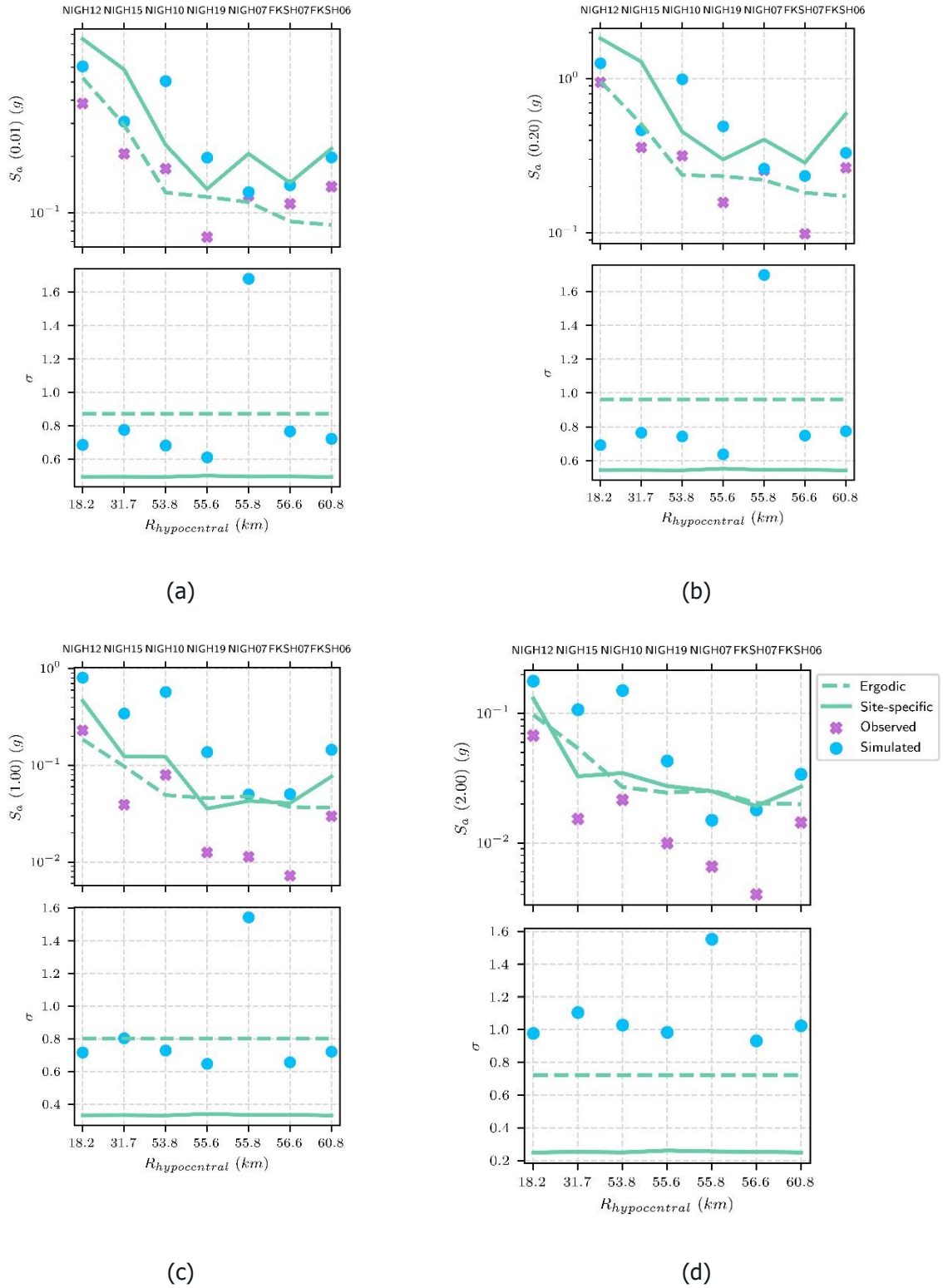


Figure 22: Comparison of mean and standard deviation of spectral accelerations for the geometrical mean of the horizontal components (GM). Observed, simulated, and predicted for the stations of interest and at different periods of vibration, (a) - $PSA(0.01s)$ or PGA, (b) - $PSA(0.05s)$, (c) - $PSA(1.0s)$, and (d) - $PSA(2.0s)$

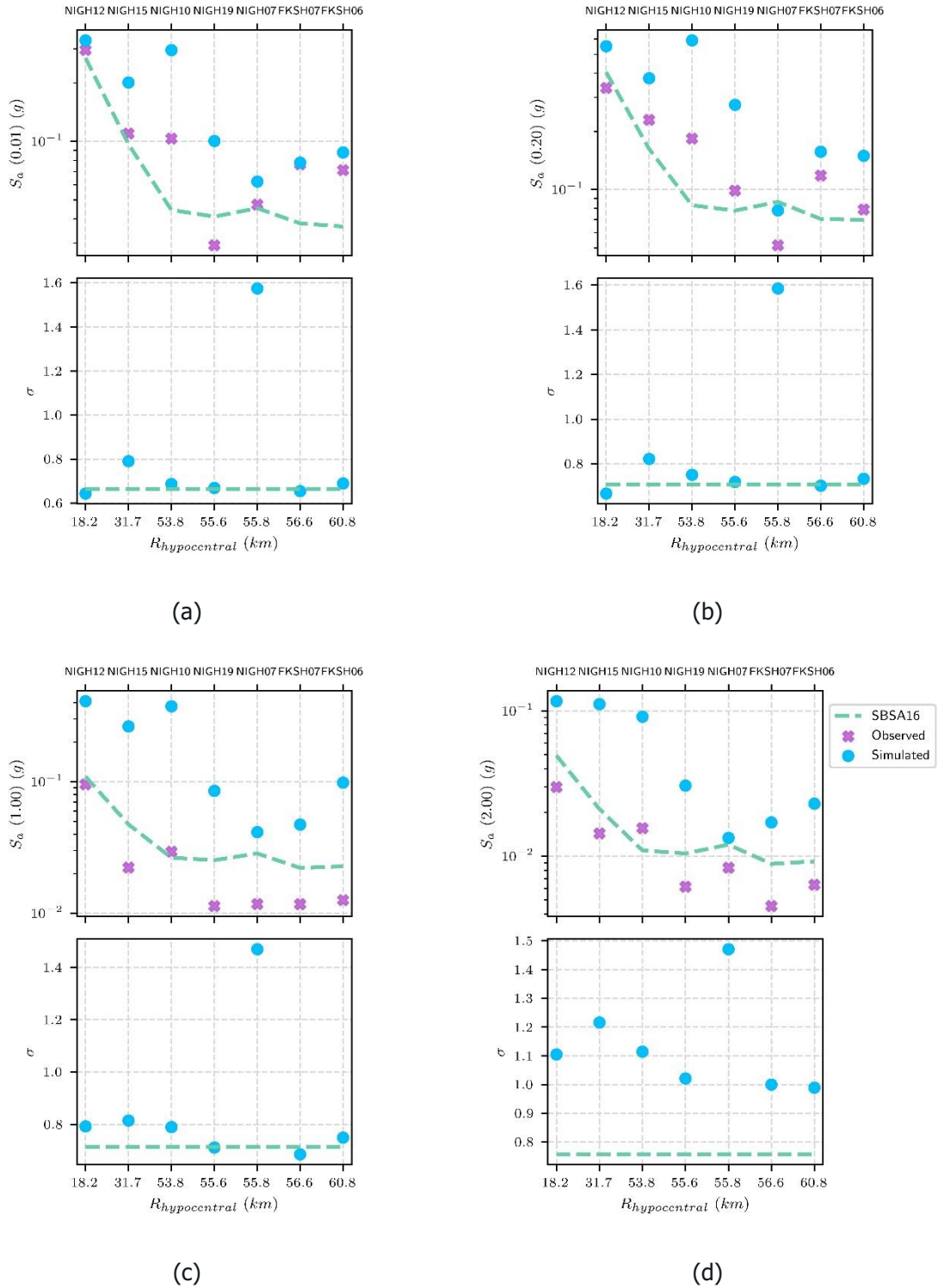


Figure 23: Comparison of mean and standard deviation of spectral accelerations for the vertical component (UD). Observed, simulated, and predicted for the stations of interest and at different periods of vibration, (a) - $PSA(0.01s)$ or PGA, (b) - $PSA(0.05s)$, (c) - $PSA(1.0s)$, and (d) - $PSA(2.0s)$



3.3.3. Validation to EDP - European database

The 3D stochastic ground motion simulation methodology was employed to generate a database of synthetic ground motion for Europe. This application was conducted with the purpose of studying the use of simulated ground motions for record selection and subsequent analysis of SDoFs (identical to the validation to EDPs introduced in section 2.0 of this document).

The synthetic database (SDB) was generated to be consistent with a reference database of recorded ground motions (RDB). The RDB was defined as a subset of the ESM (European Strong Motion) database introduced in Lanzano et al., (2019). The consistency was enforced in terms of the joint probability distributions of the main causative parameters of the scenarios contained in the RDB, namely: moment magnitude (M_w), source-to-site distance (in this case considered as the hypocentral distance $R_{\text{hypocentral}}$), hypocentral depth ($Z_{\text{hypocentre}}$), and site characteristics (in this case defined as the time-averaged shear wave velocity in the upper 30m, V_{S30}). More details on the construction of the SDB may be found in the METIS deliverable WP5.1 and in Alvarez (2022).

The previously discussed databases were considered for record selection in the analysis of the structures detailed in deliverable WP5.1. For the sake brevity, this section builds on the results obtained for just one of the considered structures: a SDoF with an elastic period of vibration of 1s and characterized by a pinching hysteresis model. The results indicated that records selected with a conditional spectrum approach (CS), (Baker, 2011), for different IM Levels, result in simulated and recorded ground motion with essentially the same distributions of causative parameters, i.e., M_w , $R_{\text{hypocentral}}$, and V_{S30} (see **Figure 24**). Despite this agreement, the distribution of studied IMs revealed that the selected ground motions had different distributions of duration for all considered IM Levels (duration was not considered in the iterative calibration of the simulation technique). See for example **Figure 25**Figure 26.

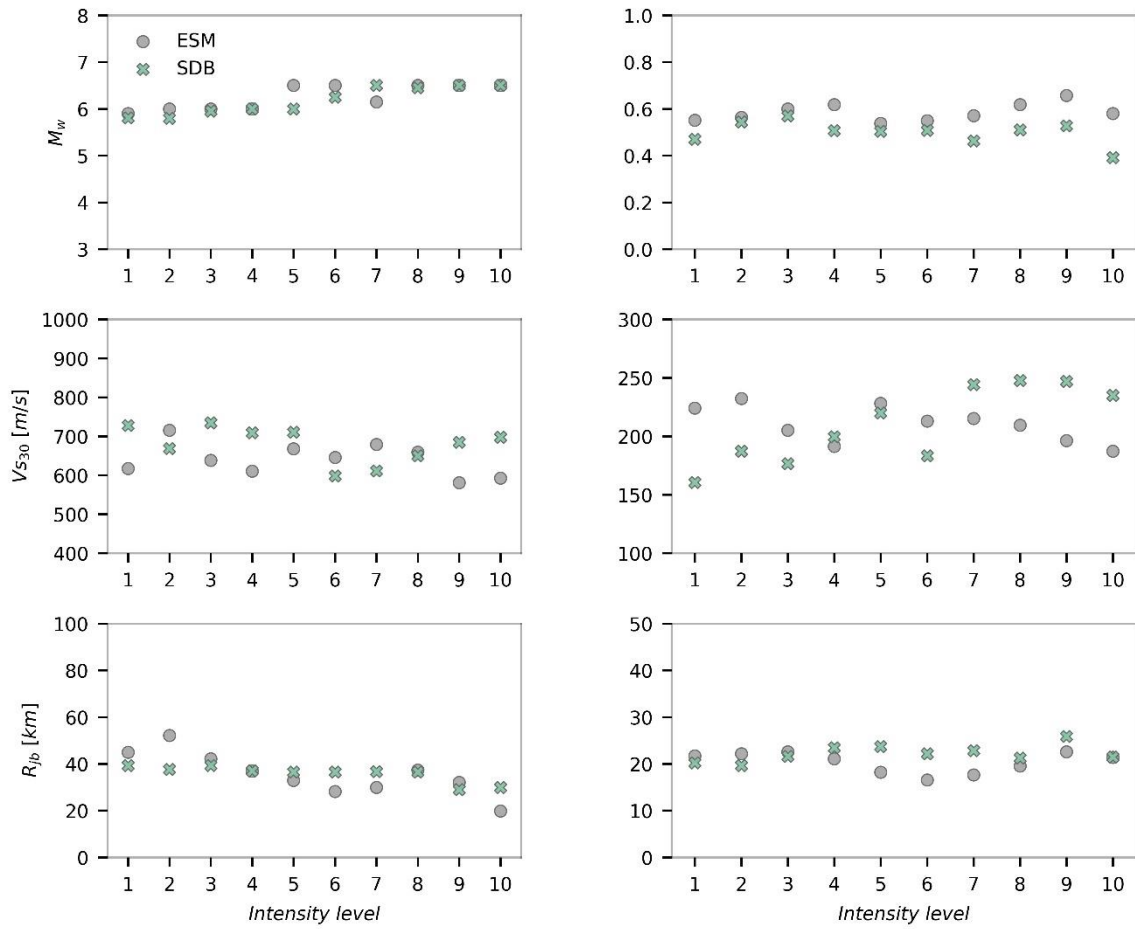


Figure 24: Distribution of M_w , V_{s30} and $R_{hypocentral}$ in terms of median (left side column) and standard deviation (right side column) for the case of $T=1.0s$

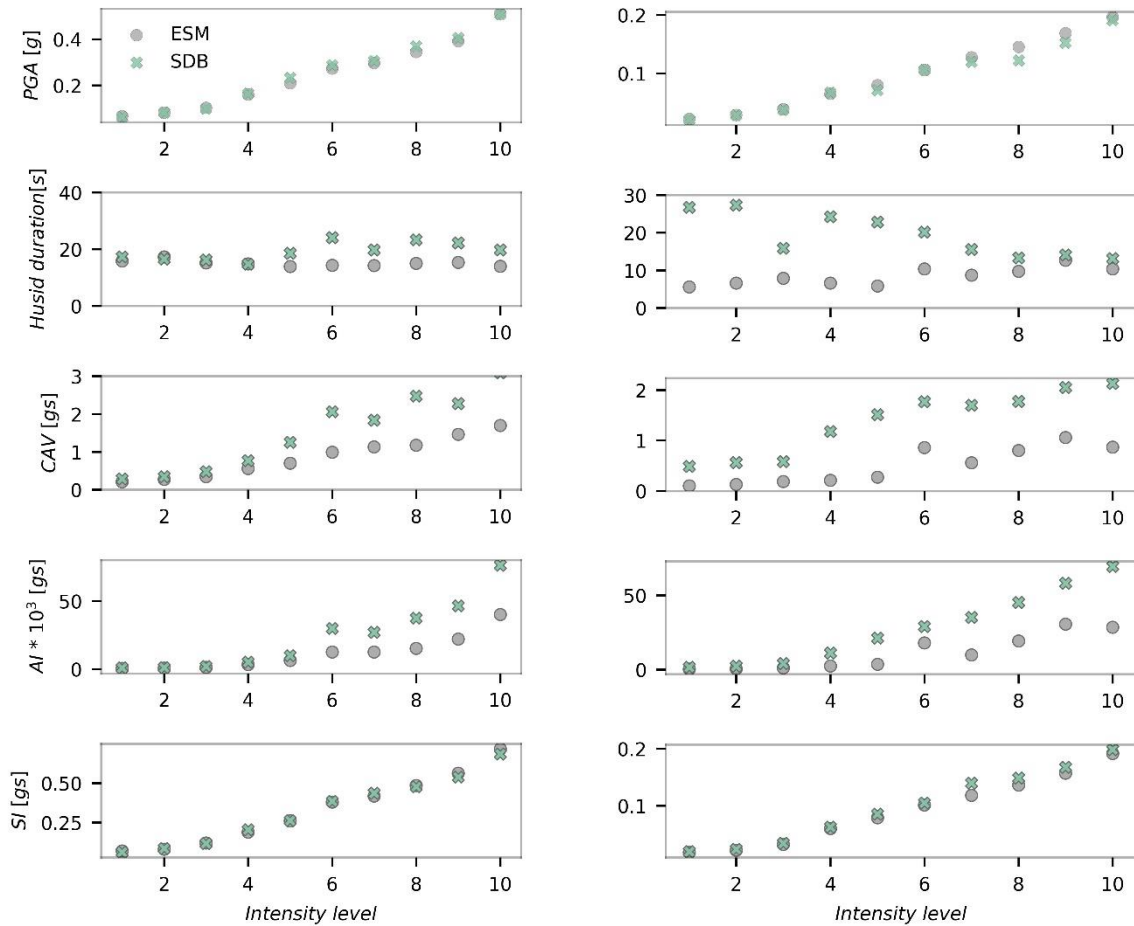


Figure 25: Distribution of different IMs, namely peak ground acceleration (PGA), Husid duration, Cumulative absolute velocity (CAV), Arias intensity (AI), and Spectral intensity (SI), from first to the last row, respectively, in terms of median (left column) and standard deviation (right column) for the case of $T=1s$.

The differences in the distribution of duration for records selected from a recorded and simulated database resulted in overall different responses, specifically for displacement related EDPs, e.g., ductility and dissipated energy. These differences, in turn, translated into different fragility curves. For example, **Figure 26** shows a comparison of fragility curves obtained for different ductility thresholds. When including the duration of the ground motion in the record selection scheme, thus expanding the sufficiency of the record selection vector of IMs, the resultant fragility curves show a considerable matching between those computed with records selected from the RDB and SDB. For clarity we refer to this extended record selection scheme as **CS(D_s)**.

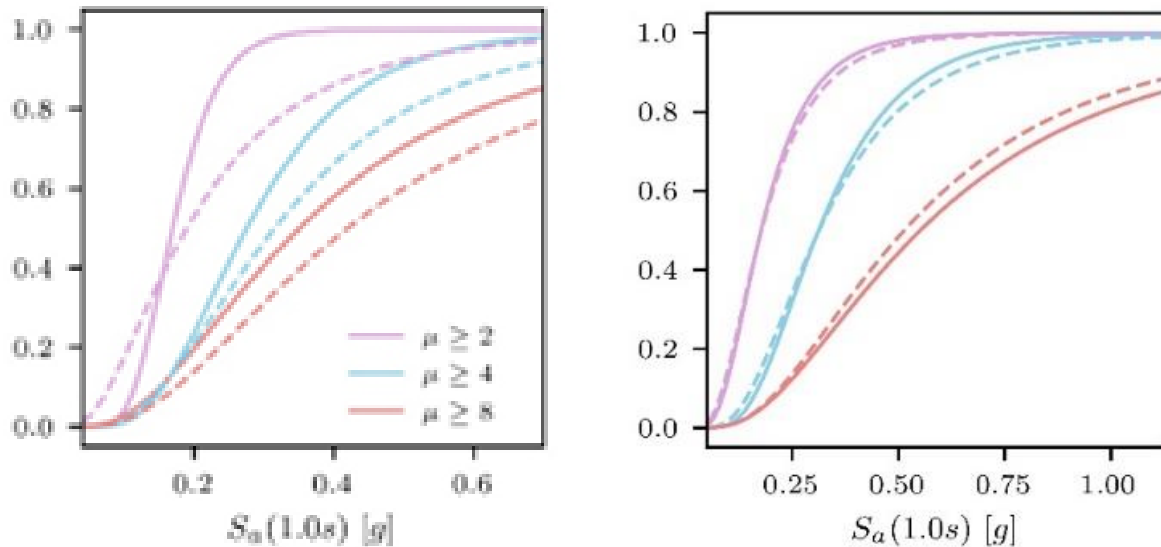


Figure 26: Comparison between the fragility curves obtained with the (left)- *CS* and (right)-*CS(D_s)* based records extracted from RDB (solid line) and SDB (dashed line) for three different ductility levels of SDoF systems with $T_1=1s$ vibration period and pinching hysteresis model.

3.3.4. Advantages/disadvantages of the approach for engineering applications

The technique presented in this section corresponds to an improved 3D stochastic ground motion simulation based on the pioneering work of Otarola & Ruiz, (2016) and S. Ruiz et al., (2018). This method includes a kinematic model of the rupture and the definition of the dynamic corner frequency and energy normalization factor, as described by Dang et al., (2022). Additionally, a post-processing procedure to include the inter-frequency correlation structure noticed in databases of recorded ground motions was proposed. This procedure builds from the original proposal of Wang et al., (2019) but was herein extended to 3D simulations and to consider the correlation structure between spectral amplitudes in different components of the motion.

Based on the validation exercises and the results briefly presented in this document, the advantages of the simulation technique are the following:

- The formulation of the complete body-wave field provides flexibility in the formulation of the different phases of earthquake ground motion. Furthermore, by considering physical models for the simulation of the wave spectra, the simulation technique is not constrained by the availability of recorded ground motions to be used as EGFs. This advantage is crucial for the simulation of ground motion in areas of low seismicity or not very well instrumented.
- When compared to the stochastic modelling considered for the high-frequency portion of the method introduced in section 3.2, the 3D stochastic ground motion simulation method herein considered explicitly models the P-wave spectra of the ground motion whereas the former only approximates the amplitude of the waves with a modified modulating function.
- The method represents a computationally efficient way to simulate earthquake scenarios in comparison to computationally intensive deterministic ground motion simulation methods
- The physical nature of the ground motion simulation model, in the sense that it explicitly models the source, propagation and site components of earthquake ground motion, is directly linked to common parameters obtained in current seismological practice. This allows for the propagation of the uncertainty observed in the input parameters to the results (seen in terms of IMs, for example). Furthermore, the input parameters may be approximated by the study of local data.

- It can be conveniently applied to the simulation of 3D ground motion time histories for rock conditions or incoming waves on bedrock. In consequence, it could be used for the creation of rock motion databases. The consideration of source, propagation, and site effects as separate components of the ground motion allows the technique to conduct simulations without site effects (bedrock) from the start. In other words, no deconvolution aiming to subtract the effect of superficial soil layers is necessary, such as for EGFs, for example.

Regarding the disadvantages of the simulation technique, the following could be mentioned:

- Much as with other stochastic techniques, the simplistic representation of the complex rupture and propagation phenomena results in the misinterpretation of the low-frequency content of the simulated ground motions. This issue can be overcome by adopting a hybrid method like what is presented in section 3.2.
- The absence of an explicit model for surface waves results in a misinterpretation of the frequency content of ground motion at large distances from the source. This drawback is common to all current stochastic methods. However, the importance of surface waves when computing nonlinear structural response is not yet clearly assessed (no major impact expected for the linear case).

3.4. Recorded ground motion corrected for site term

3.4.1. Methodology

A key component in seismic assessment is the determination of time histories for hard-rock site conditions, either as input motion for site response computations or for applications to installations built on this site type. Physics-based corrections can be applied for removing site effects from surface recordings to obtain the underlying bedrock motion. Here, we propose and test the use of the generalized inversion technique (GIT) for deconvolving surface recordings to hard-rock time series at the amplification-free seismic bedrock. The use of GIT results to predict reference or hard-rock motions has already been applied by Castellaro and Albarello (2017) to reconstruct seismic ground motion at reference site conditions and Shible (2021) to develop ground-motion predictive equations (GMPEs) for hard rock sites. Taking the Fourier transform $F(\omega)$ of the recorded time series $s(t)$ yields the amplitude spectrum $A(\omega)$ and phase spectrum $\Phi(\omega)$ with respect to the angular frequency ω :

$$F(\omega) = \frac{1}{2\pi} \int_{-\infty}^{\infty} s(t) e^{-i\omega t} dt = A(\omega) e^{-i\Phi(\omega)} \quad (4)$$

In the far-field, as shown in equation (2) in section 3.3, the Fourier amplitude spectra $A(\omega) = A(2\pi f) \equiv \text{FAS}(f)$ can be split into three main components, a source function, a path contribution over a distance r and a site term. All terms are assumed to be independent from each other. Applying a logarithm to equation (2) will provide a linear equation with an undetermined number of degrees of freedom (Castro et al. 1990). This means that a reference condition either on the response(s) of one or several sites or one or several events' source spectra is required for generalized inversions. The choice of the reference site(s), which is (are) generally assumed to be free of amplification and fixed *a priori*, will have important roles in terms of the average site responses in the dataset considered. If information about the reference site(s) is not available in advance, a frequency independent scaling factor is unresolved. Therefore, only relative amplification levels can be retrieved in that case. However, for the dataset of the Japanese KiK-net, Nakano et al. (2015, 2019) have shown that the site terms are well constrained due to their careful setting of their reference site YMGH06. This site was chosen as it has the highest S - wave velocity at the downhole location among all KiK - net stations, and the surface - to - borehole spectral ratio at that site can be expressed well by a linear 1D



amplification factor. For removing the influence of a shallow weathered rock formation, Nakano et al. (2015) approximated the influence of the weathered rock by a linear 1D amplification factor. The corresponding S - wave velocities of the weathered layers were then estimated by an inversion targeted to fit the recorded surface - to - borehole spectral ratio. For the ESM data set, Bindi and Kotha (2020) have evaluated the percentiles of the distribution of the spectral amplifications for each station and selected those stations with the minimum amplification over the entire network. To this regard, they decomposed the Fourier spectra disseminated by the Engineering Strong Motion service (Lanzano et al. 2019) by constraining to 1 the average amplification of a set of *a priori* selected stations installed on rock.

For deconvolving surface ground motions to time series at the depth of the seismological bedrock, the influence of the shallow layers must be removed. This step should result in an amplification-free dataset conditioned by a robust estimation of linear site effects. The frequency-domain solution is usually utilized, meaning that surface time series are transformed into the Fourier domain, in which the deconvolution is performed. The influence of the horizontal amplification functions is removed by dividing the FAS of the horizontal time series by the site response obtained from GIT analysis. For the latter, the root mean square (RMS) values of both the north-south and east-west components were used for minimizing the effects of the radiation pattern on seismic waves in the horizontal direction. Drouet et al. (2008) and more recently Shible et al. (2022) could show that the site terms from GIT inversions are better resolved and show a lower variability and trade-off with respect to source and path terms.

As equation (2) is composed of FAS, GIT alone is not capable of accounting for event-specific phase modifications associated with site conditions. The phase behaviour is a characteristic attribute of any site resonance which is not simply 1D (e.g., Bard and Bouchon 1985, Roten et al. 2006) and this is an attribute of many sites. Such phase modifications can be obtained in a robust way using the group delay technique (proposed by Sawada (1998) and further refined by Beauval et al. (2003)). The phrase "group delay" is predicated by the fact that these phase derivatives represent the arrival times of the energy peak of a group of waves in the frequency range around the evaluated frequency. In turn, the underlying approach allows to measure for each event and for each frequency the arrival time for each seismic phase by differentiating the phase spectrum obtained by the Fourier transformation of the signal with respect to frequency. For calculating the phase gradient, the corresponding phase spectrum must be unwrapped first, that is, absolute variations larger than π are substituted by adding or subtracting appropriate multiples of 2π . The respective quantity is defined as the group delay time. Because the group delay generally shows large variations over small frequency ranges, we carried out a smoothing operation of the phase spectrum before taking the numerical derivatives. For each event, the frequency-dependent lengthening of ground motion related to local site effects is then represented by the resulting smoothed group delay spectrum with respect to the group delay spectrum for the corresponding recordings of the same component at the reference site which shares similar source and path effects. Finally, applying an inverse Fourier transform to the amplitude and phase corrected spectra allows the site effect-free time series for seismological bedrock conditions to be retrieved. Further details are given in Pilz et al. (2022).

3.4.2. Validation and example application

Pilz et al. (2022) have systematically compared the performance of the proposed deconvolution with recordings at downhole sensors at KiK-net sites. **Figure 27** indicates two examples of the application of the event-specific phase-corrected deconvolution approach at site IBRH11. The waveforms of an M 5.8 earthquake are rich in low frequencies, and the ones of an M 3.5 event are rich in high frequencies. For both events, the horizontal FAS, in particular the shift in frequency content, and the maximum ground motions of the simulated waveforms approximate well those of the observations at the downhole sensor which is in bedrock conditions below the major impedance contrast ($V_{s30} = 2100$ m/s).

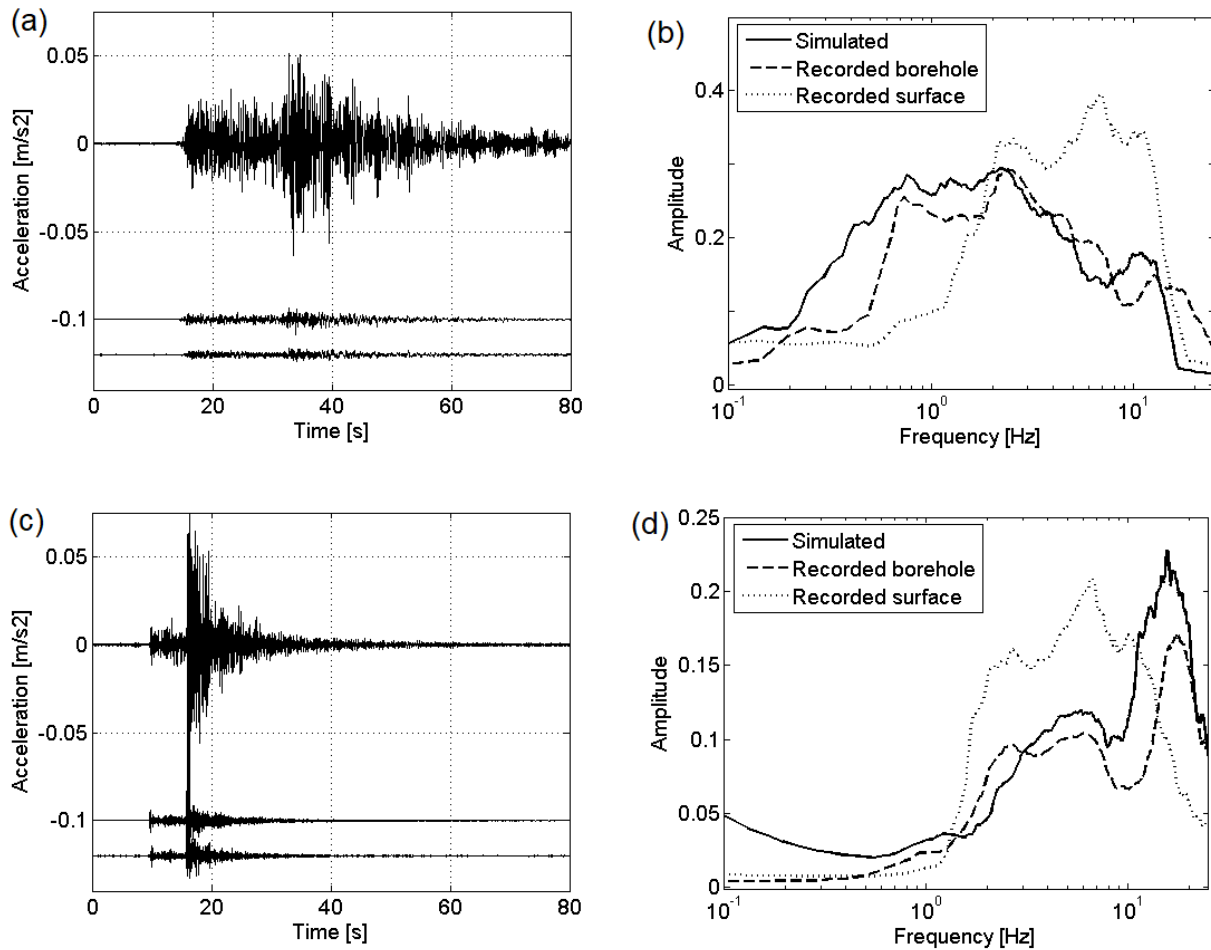


Figure 27:: Waveforms (north-south component) and corresponding Fourier amplitude spectra at KiK-net site IBRH11 for the M 5.8 event of 16 November 2012 (a, b) and the M 3.5 event of 8 September 2011 (c, d). The waveforms show the recording at the surface sensor (top waveform), the recordings at the downhole sensor (middle waveform) and the simulated waveforms at the downhole site (bottom waveform). For comparison the Fourier spectra for the surface station have been divided by a factor 5.

For validation purposes of the proposed methodology, Pilz et al. (2022) have selected a total of 90 KiK-net surface-downhole sites having no significant velocity contrasts below their downhole sensors and with the latter being located at sufficient depth so that they are not impaired significantly by down going waves. The authors have evaluated the effectiveness of the empirical predictions by comparison with recorded time series at the downhole sensors, resulting in quite high correlations and small variations in both spectral shape and amplitude over the entire frequency range for the GIT deconvolution at the majority of the 90 KiK-net sites with all mean residuals less than 0.25 in contrast to empirical and one-dimensional modelling approaches which significantly overestimate the level of hard-rock ground motion for frequencies larger than a few Hz. The reason is that the theoretical site response used for the deconvolution on average substantially underestimates the observed amplification in the high frequency range due to the inability of the transfer function to properly model down going waves which are less influential due to scattering than what 1D SH modelling predicts (Thompson et al. 2012, Tao and Rathje 2020). Moreover, the hypothesis of only vertically propagating waves through laterally homogeneous layers is very likely to break down and further bias the results at sites where prominent non-1D (i.e., 2D or 3D features like topographic effects, basin-edge induced waves, small-scale scattering among others) are present. This occurrence of 2D/3D effects might not

only affect the level of amplification in certain frequency bands but also the duration of ground motion. For example, for basin sites one might expect a longer duration of ground motion in certain frequency bands as well as a larger variability of such lengthening of ground motion which should depend on the azimuth angle of the seismic waves due to different paths from the source to the basin edge as well as the path in the sedimentary basin. The presented phase correction approach allows to consider such event-specific duration increase while the amplification is corrected with respect to a common reference. The fact that the phase is an important parameter in the deconvolution becomes clear when contrasting the deconvolved durations with and without incorporating phase changes (see **Figure 28**).

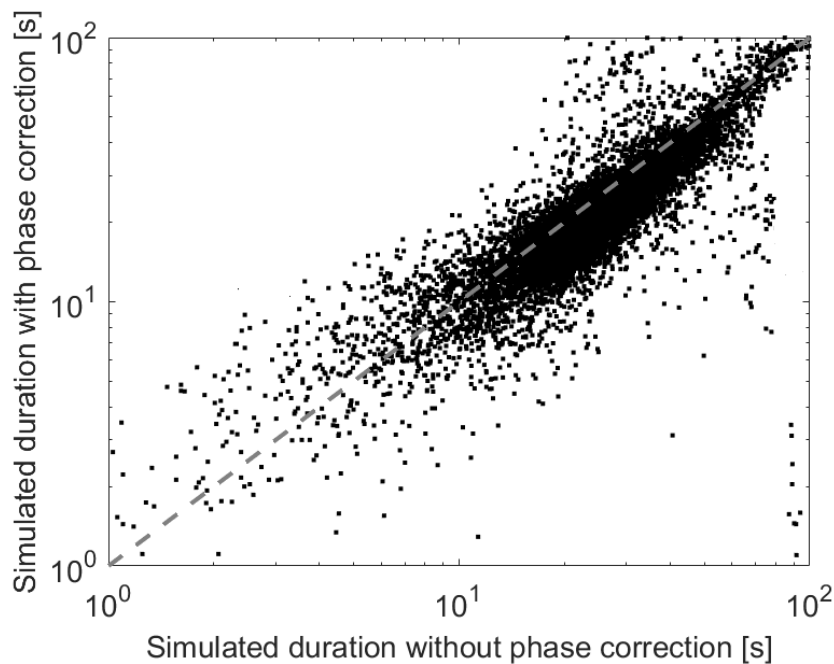


Figure 28:: Comparison of simulated durations for hard-rock conditions at KiK-net sites with and without considering a phase correction.

There is a positive bias when applying no phase correction, meaning that significantly larger durations – on average 22% – are modelled in such cases for hard-rock conditions. In this case, the modelled hard-rock durations simply correspond to the durations measured at the surface sensors. In that case, the deconvolution process consists only of a “de-siting”. Such approaches, however, must be applied if no downhole recordings are available which can be used for event- and site-specific phase corrections.

3.4.3. Advantages/disadvantages of the approach for engineering applications

Apart from empirical estimations, numerical 1D SH site transfer functions are often used to estimate site responses. The resulting transfer functions are then used to deconvolve the surface motion into time series assumed to be recorded at the bottom of the available velocity profile. While in the low frequency range, similar results to the ones obtained from GIT analysis can be expected, there is a strong negative bias at high frequencies. For frequencies higher than ~1 Hz, the waveforms modelled for the downhole sensor through the transfer function will significantly overestimate the recorded ground motion. The reason is that the theoretical site response used for the deconvolution on average substantially underestimates the observed amplification in the high frequency range. This underestimation reflects the inability of the transfer function to properly model down going waves. Moreover, for these frequencies the modelling approach is more ineffective because it requires finer velocity structures and more precise site-specific damping estimates which are critical for quantifying the amplification of seismic waves at high frequencies.



Recent investigations have indicated that only a limited number of sites can be classified as purely 1D sites while for most sites more dimensional effects with varying degree can be observed (Pilz et al. 2022). Unlike theoretical modelling approaches for which the level and resolution of input information strongly affects their accuracy, empirical approaches like GIT are expected to capture all these unconstrained 2D/3D contributions. While at first glance it might not seem consistent to use generic (averaged) GIT site factors for deconvolution due to the event-specific occurrence of such 2D/3D site effects. One possible solution to this would be to use event-specific site factors for maximum-resolvable bedrock motions. This does not necessarily mean that such a bedrock motion is more precise as these event-specific site factors will also reflect all the radiation pattern effects and path variation effects if they exist. Comparisons with event-specific GIT factors have, however, indicated that such no significant bias is caused using average site factors.

The second averaging operation incorporates the averaging of the two horizontal components for obtaining a single horizontal function. Nakano et al. (2015, 2019) found during their course of the GIT analyses for the entire KiK-net data set that the percentage of the sites with strong directional dependence in the separated site terms for NS and EW components is rather low (that is, less than 15% with significant directionality larger than the one standard deviation of the RMS site factors), meaning that also this averaging operation will not significantly affect the results.

Although the presented procedure is valid for deconvolving both horizontal and vertical time series, it has been applied here for horizontal motions only based on average RMS site factors combined with component-specific phase information. For the deconvolution of vertical ground motions, P wave site responses must be accounted for. As S-to-P conversions at the main impedance contrast will transfer energy from the horizontal on the vertical component during the S wave window, the presented deconvolution approach will provide reliable estimates of the vertical hard-rock ground motion not only from the P wave window but even from the S wave window.

While so far, the lack of empirical recordings at hard-rock sites restricts the validity of most ground motion models to sites with significantly lower velocities, the proposed approach establishes a virtual dataset which can directly be used for deriving reference ground motion models such as described for example in D5.1. It is worth mentioning that the deconvolved reference motions have been derived for amplification-free and homogeneous bedrock conditions, meaning that in similar active crustal regimes the direct use of the presented dataset of site effect-free hard-rock waveforms is possible if source and path effects are comparable. The dataset is currently prepared to be published in the open-source site database at the GFZ data portal (<https://dataservices.gfz-potsdam.de/portal/>) and can be provided upon request at any stage.

3.5. Combining spectral decomposition and empirical Green's functions approach to simulate time histories at bedrock conditions

3.5.1. Methodology

Several attempts have been made in the last decades to obtain rock ground motion at reference conditions. Many of these attempts aimed to extrapolate existing models from soft-rock to reference-rock conditions through proxy-based corrections (Cotton et al., 2006; Houtte et al., 2011; Biro and Renault, 2012). Others addressed the problem differently, mainly by deconvolving time histories from site effects under the 1D assumptions before GMM developments, resulting in corrected hard-rock motion (Cadet et al., 2012; Laurendeau et al., 2018; Shible et al., 2018). Furthermore, the detailed review of hard-rock motion predictions by Bard et al. (2020) resulted in several recommendations, one of which is the use of generalized inversions to robustly predict and remove site effects. Following



these recommendations, Shible (2021) extended the deconvolution approach of surface recordings beyond the limitation to 1D conditions through the use of site terms from generalized inversion techniques. Though the results of the deconvolution approach are promising, the potential lack of data in specific regions remains an obstacle to advancing in this direction of empirical modeling.

One alternative is to simulate earthquake ground motions using for example 3D physics-based approaches that can generate synthetic time-histories at bedrock considering a local or regional 3D crustal model and an extended-source model. However, such approaches still suffer from the limited knowledge of the propagation medium which prevents, in most cases, obtaining time histories covering a sufficiently large frequency band (0.1-20 Hz). Another particularly appealing approach is the Empirical Green's Functions (EGF) simulation method which combines empirical data and theoretical models, a version of which is discussed in section 3.1. The basic idea of the EGF approach is to interpret recordings of small events at the site of interest as reasonable approximations of Green's functions (describing the impulse response of the medium) and to convolve them suitably with more or less complex source model to simulate time histories that correspond to larger earthquakes.

The power of this technique lies in its ability to map the site- and path-specific effects into the ground-motion field, providing a local ground-motion model without the need for computationally expensive approaches to simulate 3D wave propagation. The counterpart of this approach is that the site response is only modeled for its linear behavior, while soil nonlinearity potentially observed for large ground motions is not accounted for. Moreover, the application of such an approach to obtain bedrock time histories is challenging because site effects are already included in the recordings at each site.

We propose in our work a methodology to simulate reference bedrock motions by combining spectral decompositions of ground motion with EGF simulation techniques. First, we adopt the nonparametric spectral decomposition approach (also called the generalized inversion technique, GIT) that has been developed and used in many studies to separate the contribution of source, path, and site terms (Castro et al., 1990; Oth et al., 2011, 2015). We remove the decomposed isotropic source and site effects from EGFs before simulations, through the deconvolution in the Fourier domain similar to Shible (2021). Then, we apply the EGF simulation method developed by Dujardin et al. (2020) to couple the EGF with a k^{-2} kinematic rupture model.

The workflow of the proposed methodology is as follows:

1. A dataset of recordings is collected for the target region. The region should be large enough to allow enough data for the application of the GIT,
2. GIT is applied to the selected data to separate source, path, and site terms from the observed Fourier spectra. Generally, the attenuation terms are robustly determined in the adopted GIT approach and unaffected by site/source constraints applied to inversions (Oth et al., 2011; Bindi and Kotha, 2020). This allows for obtaining a robust combined term of source and site effects,
3. EGF (representing only the path term) are obtained by correcting the observed records by source and site terms estimated by GIT. This is done for a sub-set of EGF selected to be used in the simulations to sample appropriately the region around the target site,
4. For each target magnitude (e.g., $M_w=6$) a set of kinematic rupture models following a k^{-2} slip distribution and approximating an ω^{-2} source spectrum are generated according to the approach presented by (Dujardin et al., 2020). Uncertainties in kinematic source parameters (e.g., slip distribution, rupture velocity, hypocentral location, stress drop, rupture dimensions) are sampled,
5. The source time function and the EGF associated with each sub-fault are then convolved to produce 3-component time histories that combine a simulated source contribution in addition to the empirical path effect. As a result, the absence of site effects makes the simulated ground motion representative of reference bedrock conditions.



The region-specific, site-effect-free dataset produced by this approach can be used alone or in combination with existing empirical datasets to adjust existing GMMs, derive new GMMs, or select hazard-consistent time histories to be used in soil or structural response analysis.

3.5.2. Advantages/disadvantages of the approach for engineering applications

This approach benefits from small-magnitude data that may be available in low-seismicity regions to simulate large-magnitude events, the only limitation being the appropriate signal-to-noise ratio of the small-event records. However, in contrast to purely numerical simulation approaches, the proposed methodology cannot be applied if no data is available in the target region. The main advantages of the proposed approach can be summarized as follows:

- It allows the generation of 3-component time histories for reference bedrock conditions containing empirical region-specific path effects. Provided that the usable frequency band of the EGF is large enough, the simulated data cover the wide frequency range of interest for engineering applications (about 0.2 to 20 Hz). Thanks to the use of the EGF, the method accounts for 3D wave propagation without the need for detailed theoretical modeling of the crust and using modest computational resources compared to 3D physics-based modeling,
- The use of the nonparametric GIT to estimate the source and site terms makes the EGF neither sensitive to the reference site(s) used in the inversion nor to uncertainties in the metadata (magnitude, V_{S30}) of the collected recordings,
- The methodology can be used to generate a large set of 3-component time histories covering the necessary magnitude-distance range (e.g., based on hazard disaggregation for a target site) to select hazard-consistent time histories for subsequent site response analysis or structural response evaluation.
- Compared to the classical EGF approach (such as the Irikura recipe in section 3.1), the present methodology can be applied to much-lower-magnitude events ($M2+$). In addition, this methodology relies on deconvolved EGF (for site and source effects) which allows to model ground motion for target reference rock conditions,
- Compared to the hybrid stochastic method, the wave propagations are not modeled numerically but derived empirically from small magnitude records, offering a credible alternative at high frequency,
- The GIT approach is like the recorded ground motion corrected for site term (Pilz et al., 2022). The main differences come from the fact the records were also corrected for the source and used to model target scenarios at specific sites.

However, the approach requires further validation. Further tests are necessary to assess the impact of all the used parameters, inputs, and assumptions in this approach, regarding the GIT used here. For example, the spectral decomposition of ground motion relies on constraints, one of which is the choice of the reference distance. Though it is preferably chosen in the application within the shortest distances bins available, its lower limit is controlled by the presence of data. Quantification of the impact of such a choice should be further assessed.

Limitations and proposals for further improvements of the methodology presented here are:

- the phase modification in the source-site deconvolution. At present, phase is not considered in the deconvolution, and this will undoubtedly bias to some extent the duration of the simulated time histories, particularly for soft-soil sites,
- the source model which is still quite simplified in the current approach. Pseudo-dynamic rupture models and fractal approaches may provide more realistic source radiation. Indeed, in further developments, the proposed approach would offer a better control of the rise time variation as a function of the slip wavenumber, slip gradient and rupture front velocity. The pseudo-dynamic models would allow to ensure greater consistency in parameterization of the kinematic rupture model. In addition, adding phase incoherencies in the crack summations would yield to a better control of the directivity effect over a broad frequency range.

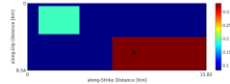
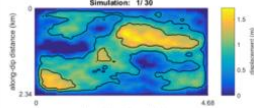
Compared to the Otarola method, this methodology is much more time-consuming, but it does not require to define the target FAS. Note that the target FAS could be a by-product of this approach to feed the Otarola method.

In what follows, this ground motion simulation methods is called the Seister approach.

3.6. Summary of modelling options discussed

In this section, we provide a table summarizing of the modelling options and codes used in this report. In the following section, chapter 4, the application of two of the approaches, suitable for the generation of scenario rock ground motion databases, to METIS case study is illustrated.

Table 1: Summary of modelling options

	Source	Propagation	Site response	Code
Irikura recipe with EGF	Irikura recipe, simplified deterministic slip distribution 	EGF	Site conditions from record (EGF - according to station location, no nonlinearity)	GRI-in-house SCEC* METIS-EDF*
SCEC broadband hybrid stochastic method	Kinematic, GP stochastic slip generator	Low frequencies: NGF	Not applied ✓ Rock motion	SCEC*
		Higher frequencies: ray theory		
3D stochastic enhanced Otarola method	Partial Kinematic source model (Gallovič., 2016)	Ray theory, Attenuation: anelastic & geometrical spreading functions	Not applied ✓ Rock motion	METIS-EDF*
Site corrected recorded time histories	As recorded	As recorded	Cleaned for site effects (site term from GIT) ✓ Rock motion	GFZ-in-house
Seister approach	Kinematic, stochastic slip distribution (Dujardin et al 2020) 	EGF (record)	Cleaned for site effects (site term from GIT) ✓ Rock motion	Seister In-house

*Available as opensource tools



4. Approach(es) for METIS case study application

The goal of the METIS case study application, is to develop scenario specific and hazard consistent databases providing a pool of accelerograms for record selection, applying the methods developed in METIS project WP 5. The METIS virtual site is in central Italy on the Tyrrhenian coast north of Rome.

The two approaches applicable for our purposes are assessed here for developing a rock ground motion database suitable the selection of time histories for structural response analysis:

- Seister approach using EGF finite fault approach corrected for site term
- 3D enhanced stochastic Otavola model developed by Alvarez et al 2022, calibrated to METIS site data

4.1. Example application of Seister approach

The methodology presented in section 3.5 is applied to the METIS case study to present an application in a moderate seismicity context characterized by a limited number of data and available rock motions, in line with the METIS objectives. The METIS virtual site is in central Italy on the Tyrrhenian coast north of Rome. **Figure 29** (upper panel) shows the considered region, stations, and earthquakes of the dataset used for the GIT application. To have reliable estimates of source and site terms, we considered a dataset covering the whole central Italy characterized by a significant number of recordings with a minimal number of 5 recordings per event and station.

The GIT is performed to determine the source and site terms. Only the average estimates are used to perform the source- and site-terms deconvolution as the correlation of the uncertainties on the two terms is unknown. To account for the epistemic uncertainties in the EGF process, we considered a large dataset of EGF (about 100) which is unusually large in such application.

The GIT was implemented as a nonparametric inversion, where no predefined models are assumed a priori. To solve the system of linear equations, two constraints need to be applied: one is on the reference distance at which the attenuation is fixed to unity and the other is usually on the site term(s). The choice of the site constraint in GIT has been shown to have a significant impact on the source and site terms due to a tradeoff. Different ways are proposed to deal with this tradeoff (Nakano et al., 2015; Bindi and Kotha, 2020; Shible et al., 2022; Morasca et al., 2022). We tested two different choices of site constraints which showed no impact on the combined source and site terms, in agreement with Oth et al. (2011) and Bindi and Kotha (2020).

The evaluation of the EGF is not sensitive to the source-site trade-off, but to some extent to the chosen reference distance at which the attenuation is fixed to unity (R_{REF}). After some tests, also supported by previous findings (Oth et al., 2011; Bindi and Kotha, 2020), the non-parametric approach we adopt in this study delivers robust attenuation functions regardless of the reference site adopted. Considering the characteristics of the dataset and the common practice (Oth et al., 2011; Bindi and Kotha, 2020; Shible et al., 2022), the reference distance R_1 was fixed at 10 km. However, adopting a shorter value ($R_1 = 2$ km) tends to increase the amplitude of the EGF up to 40% at 1 Hz. Further investigations are needed to better constrain and reduce the effects of this parameter on the results.

The subset of data selected as EGF is presented in the lower panels of **Figure 29**. The selection is done to have a manageable number of EGF adequately sampling source-to-site distances within 100 km. For the METIS application, such a dataset cannot be populated only using stations close to the METIS site due to the lack of well-recorded events around the site. Thus, we had to extend the selection to more distant stations. We initially selected about 100 EGF corresponding to events with

$3.5 < M_w < 5$, source-to-site distances smaller than 100 km and having a distance from the METIS site of 140 km at most, preferring whenever possible the shortest distances. We note that source-to-station paths of the selected EGFs show a weak coverage of the region within 80 km around the study site (**Figure 29**, lower-left panel). This is because stations close to the METIS site have well-recorded far-distance events in the Apennines but lack of well-recorded local events. Then, 6 outlier EGFs were identified based on the inspection of spectral shapes per distance bin, as shown by red ray paths on the map. **Figure 29** (lower-right panel) shows the magnitude-distance distribution for the selected EGF subset.. Further efforts are needed to include additional local small-magnitude recordings for stations close to the METIS site and improve the path term sampling of the region.

These EGFs, therefore, underwent a deconvolution process to remove source and site effects.

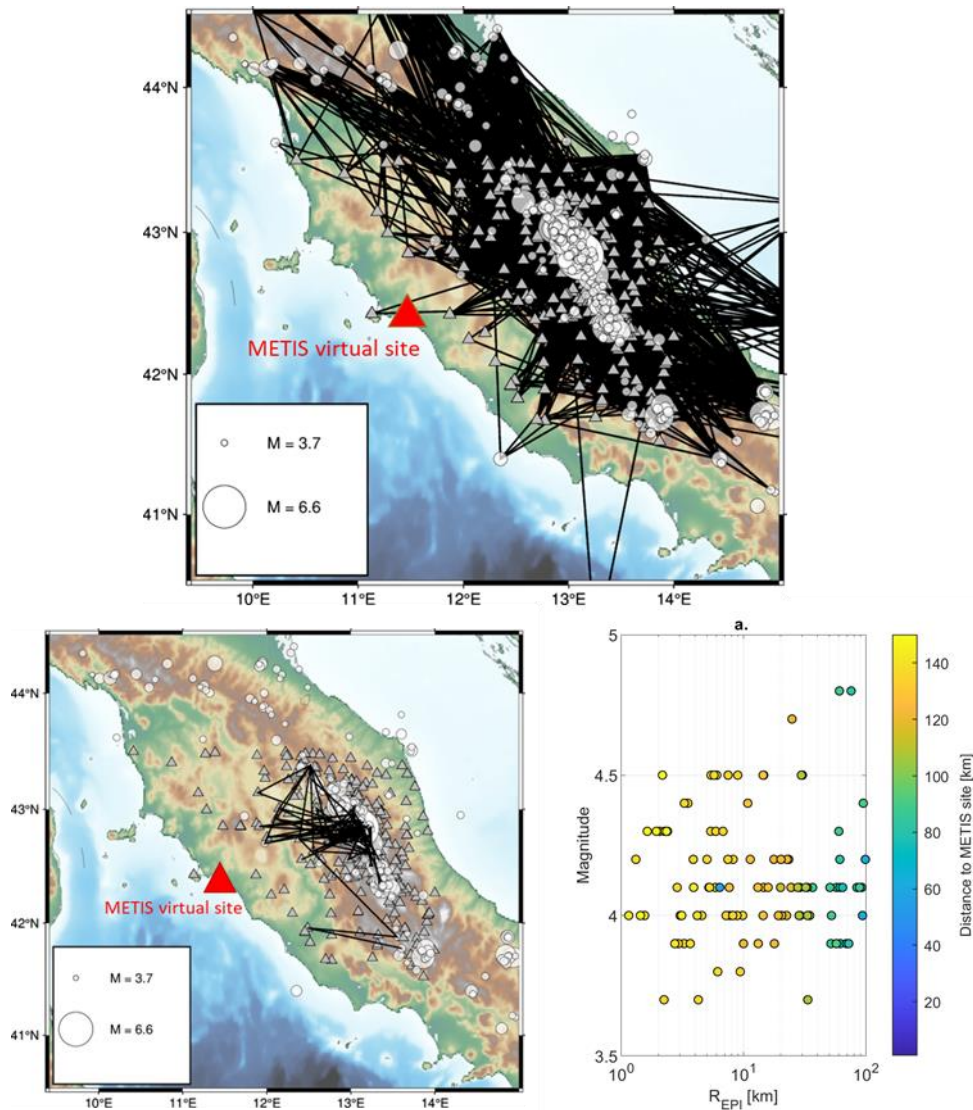


Figure 29:: (upper panel) Map showing the ESM subset of stations and earthquakes, used for the GIT application. The black lines represent the source-site ray paths in the dataset. (lower-left panel) Map showing the source-site ray paths of the selected EGFs from the initial dataset. Red ray paths correspond to outliers identified and excluded from simulations. (lower-right-panel) Magnitude-distance distribution of selected recordings to construct the database for EGF simulations ($DATA_{EGF}$). Red triangles correspond to the outliers identified.

Figure 30 presents the Fourier Amplitude Spectra (FAS) of the selected EGF after correction for source and site terms, grouped into three increasing distance ranges. The amplitude of the FAS decreases with increasing distance as expected, with a larger reduction at high frequencies. Interestingly, the variability of the FAS is small within each group showing that the deconvolution of source and site terms is very effective. The selected EGFs have a usable frequency band of at least 0.2Hz to 25 Hz. Note that a few outliers were identified and removed (6 out of 110).

The simulation approach couples the EGF with a kinematic description of the extended fault assuming a k^{-2} slip model for the target events. We refer to Dujardin et al. (2018, 2020) for further readings on the general formulation of the method. We simulate target events with $M_w = 5.0, 5.5, 6.0, 6.25,$ and 6.5 . Note the methodology can be used to generate a large set of 3-component time histories covering the necessary magnitude-distance range (e.g., based on hazard disaggregation for a target return period) which would allow selecting hazard-consistent time histories for subsequent site response analysis or structural response evaluation. For each M_w , a set of 30 rupture models are used to capture, to some extent, the uncertainties in the kinematic parameters (i.e., slip distribution, rupture velocity, nucleation point, stress drop, and rupture dimensions). The source-to-station distances and azimuths are given by the considered dataset of EGF.

An example of three kinematic models for $M_w=5.5$ scenarios is shown in **Figure 31**. Considering that we used about 100 EGFs and 30 rupture models, we simulated about 3000 time-histories for each magnitude up to 100 km distance.

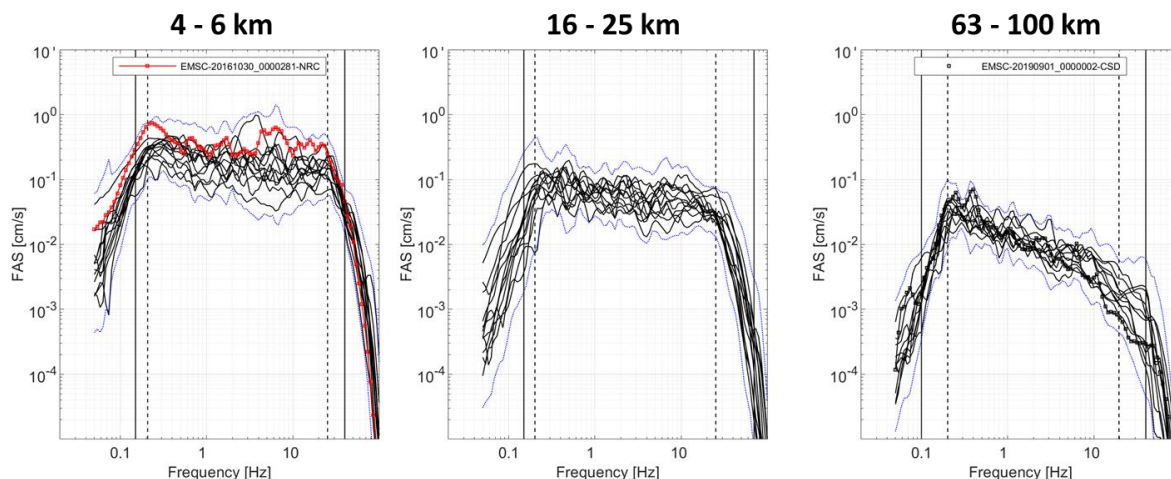


Figure 30: Acceleration Fourier Amplitude Spectra (FAS) of the EGF grouped into three distance bins. The EGF were deconvolved by source and site terms (black). EGF-FAS outliers (red curves) were identified when exceeding the mean ± 2.5 sigma (blue curves) in the frequency range of interest 5-25 Hz.

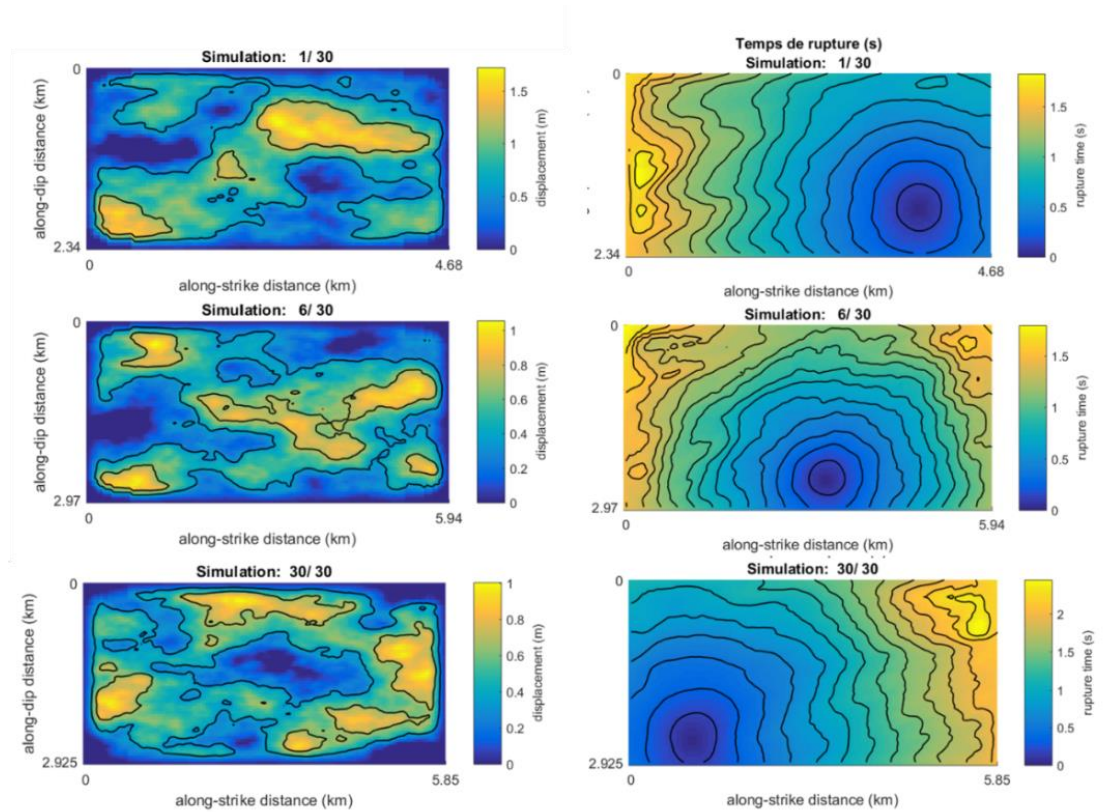


Figure 31:Example of randomly generated K^{-2} slip distributions (left) and hypocenter locations and related rupture times (right) for the $M_w=5.5$ scenarios. Note the different dimensions of the ruptures. The hypocenter (rupture time equal to 0) is always located in the lower half of the rupture.

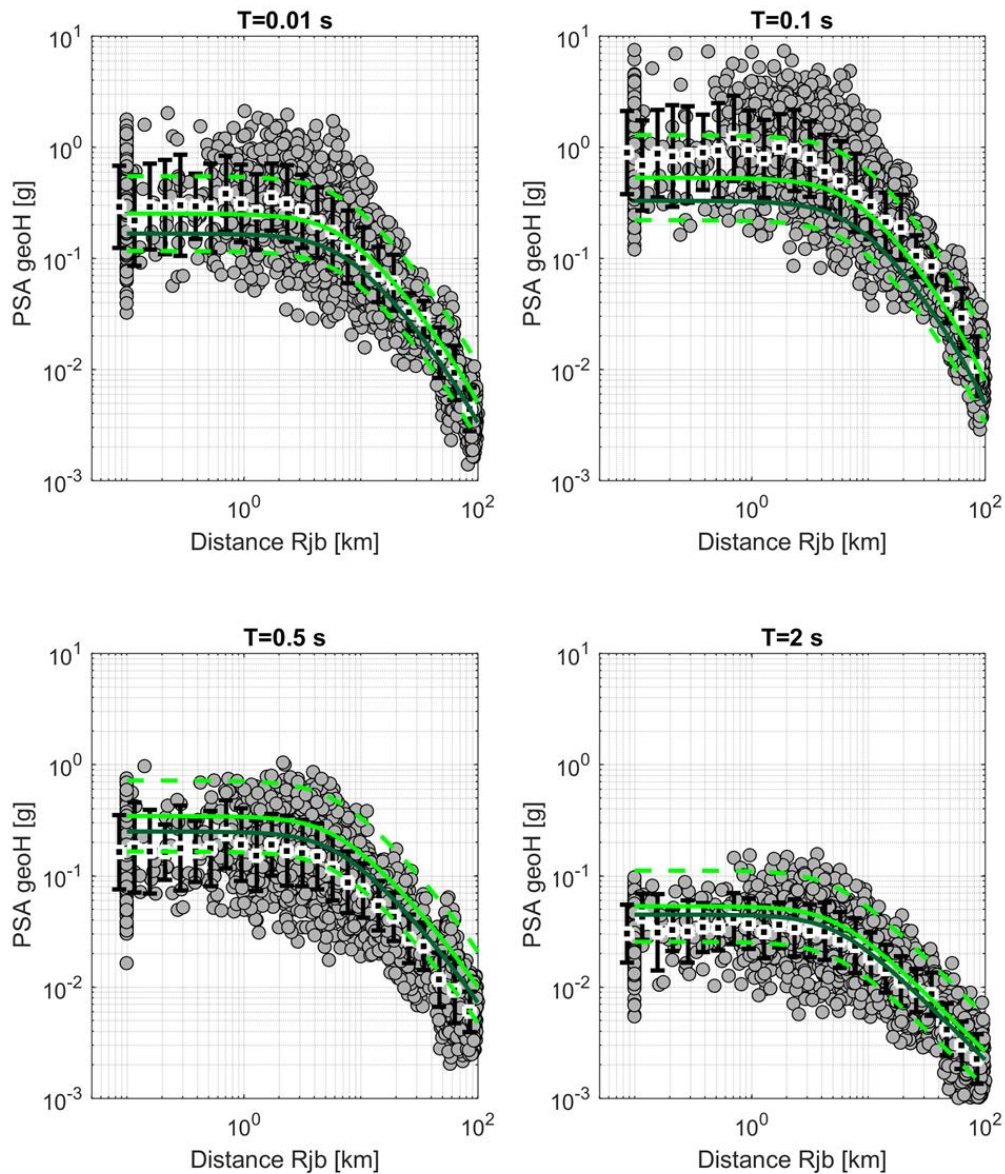


Figure 32: Simulated pseudo-spectral acceleration (PSA) for the geometric mean of the horizontal components (gray dots) as a function of the Joyner-Boore distance (R_{jb}) for 4 spectral periods ($T=0.01$ s, 0.1 s, 0.5 s, and 2 s) for the $M_w=5.5$ scenarios. The vertical black bars represent the mean and standard deviation of simulated values over distance bins. Stations within the surface projection of the rupture are plotted at $R_{jb} = 0.1$ km. The GMM for Italy (ITA18) by Lanzano et al. (2019) is plotted in light green (median ± 1 standard deviation) considering a $V_{s30} = 800$ m/s and normal fault mechanism. The median ITA18 adjusted for reference rock conditions according to Lanzano et al. (2022) is shown in dark green.

In **Figure 32**, for the $M_w=5.5$ scenarios, the response spectra (at spectral periods $T = 0.01$ s, 0.1 s, 0.5 s, and 2 s) from the time histories are represented as a function of distance (R_{jb}) and are compared with the empirical GMM for Italy (ITA18) by Lanzano et al. (2019) for a $V_{s30} = 800$ m/s and with the one modified by Lanzano et al. (2022) for reference rock. We observe that the simulated values are in good agreement with the Lanzano et al. (2019; 2022) GMM and the mean values of the simulations are in general within one standard deviation of the GMM. The distance scaling of the simulated values is also very consistent with that of ITA18 confirming that the use of the EGF to

account for the path effect is appropriate. The standard deviation of the simulated values is also in broad agreement with that of the ITA18 at least up to about 20 km. At a longer distance, the standard deviation of simulated values decreases possibly because the variability of the rupture models mostly affects ground motions at short distances. At longer distances, the variability is mostly controlled by differences in the attenuation along the path which in our case relies on a limited region/dataset. Note that simulated time histories were low-passed filtered at 15Hz (further tests are being made to extend the usable frequency up to 20-25 Hz).

In **Figure 33**, the comparison with the ITA18 model is presented in terms of response spectra at distances of 10 km and 50 km. We observe that the response spectra of the simulated time histories are generally in good agreement with the ones predicted by the ITA18 GMM being the mean simulated spectrum within the standard deviation of the ITA18 estimates. We also note that the spectral shapes of the mean simulated spectra are slightly different than those from ITA18 adjusted for reference rock and in particular the peak of the spectrum (around 10 Hz) is shifted toward higher frequencies. Such difference is mostly related to the EGF because the source spectra are on average flat above the corner frequency and could be due to the reference bedrock conditions implied by the adopted deconvolution procedure. Indeed, the correction for both nonparametric source and site terms implies that any site amplification is removed regardless the reference site conditions adopted in the GIT. The results are thus representative of the seismic bedrock at each station. Further analyses are ongoing to understand the origin of such differences.

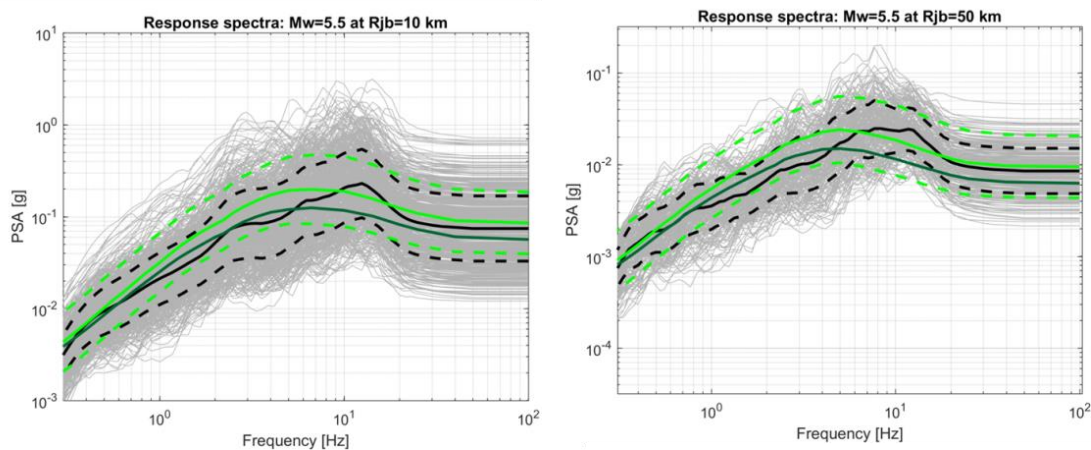


Figure 33: Simulated response spectra (in gray) in two distance bins around 10 km (left) and around 50 km (right) for Mw=5.5 scenarios. The mean of the simulated spectra is shown in black. The GMM for Italy (ITA18) by Lanzano et al. (2019) is plotted in light green (median \pm 1 standard deviation) considering a $V_{S30} = 800$ m/s and normal fault mechanism. The median ITA18 adjusted for reference rock conditions according to Lanzano et al. (2022) is shown in dark green.

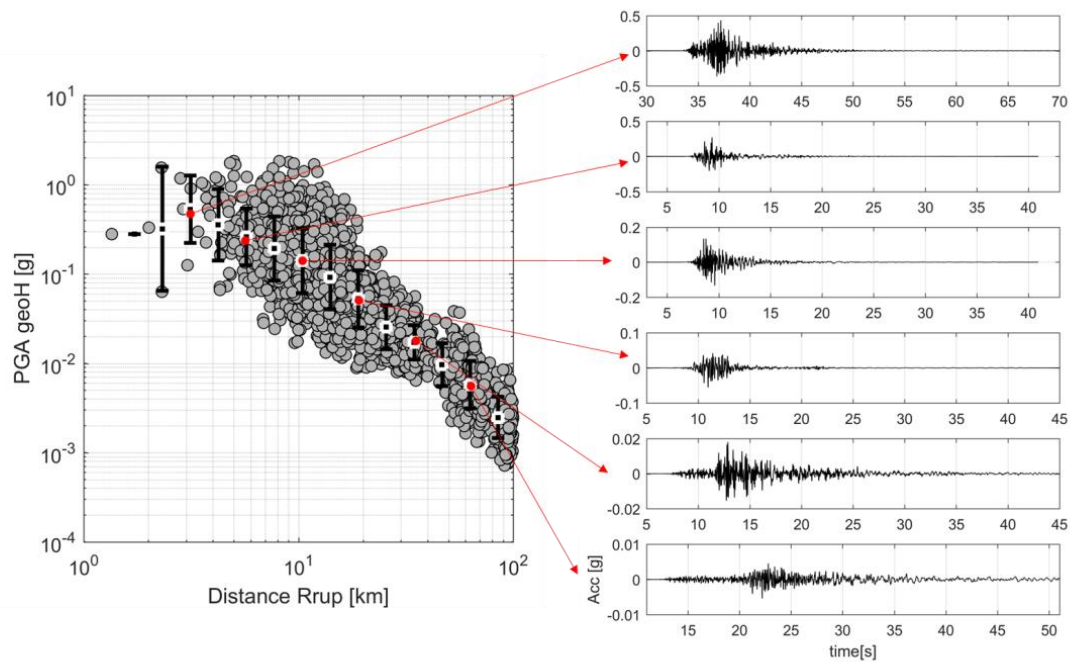


Figure 34: (Left) Simulated PGA (geometric mean of horizontal components) as a function of the rupture distance (R_{rup}) for the $M_w=5.5$ events. The vertical black bars represent the mean and standard deviation of simulated values over distance bins. (Right) selected time-histories (one horizontal component) having PGA values close to the mean PGA in increasing distance bins. The time axes have the same duration.

The **Figure 34** shows example time histories having PGA values close to the mean PGA in increasing distance bins. We can note that while the amplitudes of the simulated time histories decrease, the durations realistically increase with increasing distance as well as the time difference between P- and S-waves arrivals. Realistic time histories can thus be selected to be representative of a desired hazard level, including related variability.

Even though the proposed methodology has some limitations (discussed in section 3.5.2) it offers the possibility to obtain time-histories at bedrock carrying the information on region-specific path effects without a detailed knowledge of the 3D crustal model. The approach can be applied to regions with limited data relying on EGF extracted from small-magnitude records. In the perspective of the application to the METIS case study, 3-component time histories covering the necessary magnitude-distance range (e.g., based on hazard disaggregation for a target return period) could be extracted from the compiled dataset (or simulated for the necessary scenarios) for subsequent site response analysis or structural response evaluation. Before application in engineering studies, the distributions of IMs from simulated ground motions need to be evaluated to make sure that they are like those of real ground motions. This will be done by following the procedure for the validation of ground motion simulation methodologies to Engineering Demand Parameters described in section 2 (examples of such comparisons are also in Deliverable D5.1).

4.2. 3D Stochastic rock motion database (proposal for approach to be implemented)

The 3D stochastic Ground motion simulation methodology is applied to the METIS case study to generate a site-specific scenario database. This means that the methodology will be used to simulate the earthquake scenarios obtained from the disaggregation of the PSHA for the considered region. These scenarios are to be obtained from a calibrated model considering the parameters describing the shape of the FAS, obtained from studies based on the inversion of recorded data, and then adapted to the specificities of the simulation method by an iterative calibration of the parameters describing the spectral shape and duration of the simulated earthquake ground motion (much like described in section 2.4.2 of this document). To this end, the attenuation, site, and source effects obtained from the results presented in section 4.1 can be used. This does not only provide a more specific regional characterization of the FAS, but also a more comparable set of scenarios for the herein considered study. The verification of the calibration procedure can be conducted considering the same scenarios and reference GMMs introduced in the previous section, i.e., ITA18 (Lanzano et al, 2019).

5. Conclusions and further work

This work has compared different approaches and tools for possible application to the development of a scenario specific database containing many rock time histories suitable for record selection for engineering studies.

Indeed, for nuclear safety assessment very high return periods need to be considered to determine relevant scenarios and deduce target ground motion characteristics for record selection. The lack of such extreme events in European databases and the scarcity of ground motion recorded on rock motivates the interest in artificial time histories in general and ground motion time history simulation. The methods need to be suitable for the simulation of many scenarios ground motion representing natural variability at moderate cost.

Two approaches suitable for the simulation of rock ground motion and featuring the 3 components have been selected. They need further validation for engineering application applying the battery of tests described in section 2 and D5.1 focusing on rock conditions and if approved will be applied to generate an artificial database for record selection in METIS case study.

6. Acknowledgments

Strong motion data for the KK site used in section 3.1 were provided by the National Research Institute for Earth Science and Disaster Resilience (K-NET, KiK-net, and F-net) and Tokyo Electric Power Company Holdings (TEPCO). The TEPCO data were obtained from the Association for Earthquake Disaster Prevention. The part of this study was based on the 2022 research project "Examination for uncertainty of strong ground motion prediction for inland crustal earthquakes" by The Secretariat of the Nuclear Regulation Authority (NRA), Japan.



7. Bibliography

- Afshari, K., & Stewart, J. P. (2016b). Physically parameterized prediction equations for significant duration in active crustal regions. *Earthquake Spectra*, 32(4), 2057–2081. <https://doi.org/10.1193/063015EQS106M>
- Afshari, K., Stewart, J. P. (2019). Insights from California vertical arrays on the effectiveness of ground response analysis with alternative damping models. *Bulletin of the Seismological Society of America*, 109(4), 1250-1264.
- Al Atik, L., Abrahamson, N., Bommer, J. J., Scherbaum, F., Cotton, F., & Kuehn, N. (2010). The variability of ground-motion prediction models and its components. *Seismological Research Letters*, 81(5), 794–801. <https://doi.org/10.1785/gssrl.81.5.794>
- Alvarez, L. (2022) Improved 3D Ground Motion Simulation for Structural Response Analysis. Doctoral dissertation, IUSS, Université Gustave Eiffel.
- Anderson J (2004) Quantitative measure of the goodness-of-fit of synthetic seismograms
- Alvarez, L., Bonilla, L. F., Bazzurro, P., Aochi, H., Zentner, I., Senfaute, G. (2022). Assessment of a 3D Stochastic Ground Motion Simulation Methodology. (In Process).
- Asano, K., & Iwata, T. (2009). Source rupture process of the 2004 Chuetsu, Mid-Niigata Prefecture, Japan, earthquake inferred from waveform inversion with dense strong-motion data. *Bulletin of the Seismological Society of America*, 99(1), 123–140. <https://doi.org/10.1785/0120080257>
- Atkinson GM, Assatourians K (2014) Implementation and Validation of EXSIM (A Stochastic Finite-Fault Ground-Motion Simulation Algorithm) on the SCEC Broadband Platform *Seismological Research Letters* 86:48-60 doi:10.1785/0220140097
- Atkinson GM, Goda K (2010) Inelastic Seismic Demand of Real versus Simulated Ground-Motion Records for Cascadia Subduction Earthquakes *Bulletin of the Seismological Society of America* 100:102-115 doi:10.1785/0120090023
- Atkinson, G. M., Assatourians, K., Boore, D. M., Campbell, K., & Motazedian, D. (2009). A guide to differences between stochastic point-source and stochastic finite-fault simulations. *Bulletin of the Seismological Society of America*, 99(6), 3192–3201. <https://doi.org/10.1785/0120090058>
- Azzaro, R., et al. (2016), The 24 August Amatrice 2016 earthquake: Macroseismic survey in the damage area and EMS intensity assessment, *Ann. Geophys.*, 59, 8, doi:10.4401/ag-7203
- Bard, P. Y., & Bouchon, M. (1980). The seismic response of sediment-filled valleys. Part 2. The case of incident P and SV waves. *Bulletin of the Seismological Society of America*, 70(5), 1921-1941.
- Bard, P.-Y., S. S. Bora, F. Hollender, A. Laurendeau, and P. Traversa, 2020, Are the Standard V S - Kappa Host-to-Target Adjustments the Only Way to Get Consistent Hard-Rock Ground Motion Prediction?, *Pure Appl. Geophys.*, 177, no. 5, 2049–2068, doi: 10.1007/s00024-019-02173-9.
- Basilic, R., Kastelic, V., Demircioglu, M. B., Garcia Moreno, D., Nemser, E. S., Petricca, P., Sboras, S. P., Besana-Ostman, G. M., Cabral, J., Camelbeeck, T., Caputo, R., Danciu, L., Domac, H., Fonseca, J., García-Mayordomo, J., Giardini, D., Glavatovic, B., Gulen, L., Ince, Y., Pavlides, S., Sesetyan, K., Tarabusi, G., Tiberti, M. M., Utkucu, M., Valensise, G., Vanneste, K., Vilanova, S., Wössner, J. (2013): The European Database of Seismogenic Faults (EDSF) compiled in the framework of the Project SHARE, (Share - The European Database of Seismogenic Faults). <https://doi.org/10.6092/INGV.IT-SHARE-EDSF>
- Bates, D., M. Machler, B. Bolker, and S. Walker (2015). Fitting Linear Mixed-Effects Models Using lme4, *Journal of Statistical Software* 67(1), 1–48



Beauval, C., Bard, P. Y., Moczo, P., & Kristek, J. (2003). Quantification of frequency-dependent lengthening of seismic ground-motion duration due to local geology: Applications to the Volvi area (Greece). *Bulletin of the Seismological Society of America*, 93(1), 371-385.

Bijelić N, Lin T, Dierlen, D (2014) Seismic Response of a Tall Building to Recorded and Simulated Ground Motions. Tenth U.S. National Conference on Earthquake Engineering Frontiers of Earthquake Engineering, doi: 10.4231/D3VH5CJ72

Bijelić N, Lin T, Deierlein GG (2018) Validation of the SCEC Broadband Platform simulations for tall building risk assessments considering spectral shape and duration of the ground motion Earthquake Engineering & Structural Dynamics 47:2233-2251 doi:<https://doi.org/10.1002/eqe.3066>

Bijelić N, Lin T, Deierlein GG (2019) Evaluation of Building Collapse Risk and Drift Demands by Nonlinear Structural Analyses Using Conventional Hazard Analysis versus Direct Simulation with CyberShake Seismograms Bulletin of the Seismological Society of America 109:1812-1828 doi:10.1785/0120180324

Bindi, D., & Kotha, S. R. (2020). Spectral decomposition of the Engineering Strong Motion (ESM) flat file: regional attenuation, source scaling and Arias stress drop. *Bulletin of Earthquake Engineering*, 18(6), 2581-2606.

Bindi, D., Zaccarelli, R., Razafindrakoto, H., Yen, M.-H., Cotton, F. (2023): Empirical shaking scenarios for Europe: a feasibility study. –*Geophys. J. Int.*, 232, 2, 990-1005.

Biro, Y., and P. Renault, 2012, Importance and Impact of Host-to-Target Conversions for Ground Motion Prediction Equations in PSHA, *Proc. of the 15th World Conference on Earthquake Engineering.*, 10.

Boore, D. M. (1983). STOCHASTIC SIMULATION OF HIGH-FREQUENCY GROUND MOTIONS BASED ON SEISMOLOGICAL MODELS OF THE RADIATED SPECTRA. In *Bulletin of the Seismological Society of America* (Vol. 73, Issue 6).

Boore, D. M. (2003). Simulation of Ground Motion Using the Stochastic Method. *Pure and Applied Geophysics*, 160, 635–676.

Burks LS, Baker JW (2014) Validation of Ground-Motion Simulations through Simple Proxies for the Response of Engineered Systems Bulletin of the Seismological Society of America 104:1930-1946 doi:10.1785/0120130276

Burks LS, Zimmerman RB, Baker JW (2015) Evaluation of Hybrid Broadband Ground Motion Simulations for Response History Analysis and Design Earthquake Spectra 31:1691-1710 doi:10.1193/091113EQS248M

Cadet, H., P.-Y. Bard, and A. Rodriguez-Marek, (2012), Site effect assessment using KIK-net data: Part 1. A simple correction procedure for surface/downhole spectral ratios, *Bull Earthquake Eng*, 10, no. 2, 421–448, doi: 10.1007/s10518-011-9283-1.

Castro, R. R., Anderson, J. G., Singh, S. K. (1990). Site response, attenuation and source spectra of S waves along the Guerrero, Mexico, subduction zone. *Bulletin of the Seismological Society of America*, 80(6A), 1481-1503.

Castellaro, S., & Albarello, D. (2017). Reconstructing seismic ground motion at reference site conditions: the case of accelerometric records of the Italian National Accelerometric Network (RAN). *Bulletin of Earthquake Engineering*, 15, 2377-2391.

Chiaraluce L., Di Stefano R., Tinti E., Scognamiglio L., Michele M., Casarotti E., Cattaneo M., De Gori P., Chiarabba C., Monachesi G., Lombardi A., Valoroso L., Latorre D., Marzorati S (2017) The 2016 Central Italy Seismic Sequence: A First Look at the Mainshocks, Aftershocks, and Source Models. *Seismological Research Letters* 2017; 88 (3): 757–771. doi: <https://doi.org/10.1785/0220160221>



Cotton, F., F. Scherbaum, J. J. Bommer, and H. Bungum, 2006, Criteria for Selecting and Adjusting Ground-Motion Models for Specific Target Regions: Application to Central Europe and Rock Sites, *J Seismol*, 10, no. 2, 137, doi: 10.1007/s10950-005-9006-7.

Das S., Kostrov B. V. (1986), Fracture of a single asperity on a finite fault, *Earthq Source Mechanics* (Geophysical Monograph 37, Maurice Ewing Series, 6, American Geophysical Union) pp. 91- 96.

De la Torre CA, Bradley BA, Lee RL (2020) Modeling nonlinear site effects in physics-based ground motion simulations of the 2010–2011 Canterbury earthquake sequence. *Earthq Spectra* 36:856–879

Dreger, D. S., & Jordan, T. H. (2015). Introduction to the focus section on validation of the SCEC broadband platform V14.3 simulation methods. *Seismological Research Letters*, 86(1), 15–16. <https://doi.org/10.1785/0220140233>

Dreger DS, Beroza GC, Day SM, Goulet CA, Jordan TH, Spudich PA, Stewart JP (2014) Validation of the SCEC Broadband Platform V14.3 Simulation Methods Using Pseudospectral Acceleration Data *Seismological Research Letters* 86:39-47 doi:10.1785/0220140118

Drouet, S., Chevrot, S., Cotton, F., & Souriau, A. (2008). Simultaneous Inversion of Source Spectra, Attenuation Parameters, and Site Responses: Application to the Data of the French Accelerometric Network. *Bulletin of the Seismological Society of America*, 98(1), 198-219.

Dujardin, A., F. Hollender, M. Causse, C. Berge-Thierry, B. Delouis, L. Foundotos, G. Ameri, and H. Shible, 2020, Optimization of a Simulation Code Coupling Extended Source (k–2) and Empirical Green's Functions: Application to the Case of the Middle Durance Fault, *Pure Appl. Geophys.*, 177, no. 5, 2255–2279, doi: 10.1007/s00024-019-02309-x.

Eshelby, J. D. (1957), The determination of the elastic field of an ellipsoidal inclusion, and related problems, *Proc Roy Soc A* 241, 376-396.

Fayaz J, Azar S, Dabaghi M, Zareian F (2020) Methodology for Validation of Simulated Ground Motions for Seismic Response Assessment: Application to CyberShake Source-Based Ground Motions *Bulletin of the Seismological Society of America* doi:10.1785/0120200240

Frankel A (2009) A constant stress-drop model for producing broadband synthetic seismograms: Comparison with the next generation attenuation relations *Bulletin of the Seismological Society of America* 99 doi:10.1785/0120080079

Galasso C, Kaviani P, Tsioulou A, Zareian F (2018) Validation of Ground Motion Simulations for Historical Events using Skewed Bridges *Journal of Earthquake Engineering* 24:1-23 doi:10.1080/13632469.2018.1483277

Galasso C, Zareian F, Iervolino I, Graves R (2012) Validation of Ground-Motion Simulations for Historical Events Using SDoF Systems *The Bulletin of the Seismological Society of America* 102:2727-2740 doi:10.1785/0120120018

Galasso C, Zhong P, Zareian F, Iervolino I, Graves RW (2013) Validation of ground-motion simulations for historical events using MDoF systems *Earthquake Engineering & Structural Dynamics* 42:1395-1412 doi:<https://doi.org/10.1002/eqe.2278>

Goda K, Kurahashi S, Ghofrani H, Atkinson GM, Irikura K (2015) Nonlinear Response Potential of Real versus Simulated Ground Motions for the 11 March 2011 Tohoku-oki Earthquake *Earthquake Spectra* 31:1711-1734 doi:10.1193/071213EQS201M

Goda K, Kurahashi S, Ghofrani H, Atkinson GM, Irikura K (2015) Nonlinear Response Potential of Real versus Simulated Ground Motions for the 11 March 2011 Tohoku-oki Earthquake *Earthquake Spectra* 31:1711-1734 doi:10.1193/071213EQS201M

Goulet CA, Abrahamson NA, Somerville PG, Wooddell KE (2014) The SCEC Broadband Platform Validation Exercise: Methodology for Code Validation in the Context of Seismic-Hazard Analyses *Seismological Research Letters* 86:17-26 doi:10.1785/0220140104.



Graves, R. W., and A. Pitarka (2015). Refinements to the Graves and Pitarka (2010) broadband ground-motion simulation method, *Seismol. Res. Lett.* 86, 75–80.

Graves, R. W., and A. Pitarka (2016). Kinematic ground-motion simulations on rough faults including effects of 3D stochastic velocity perturbations, *Bull. Seismol. Soc. Am.* 106, 2136–2153.

Grünthal, G., Stromeyer, D., Bosse, C. *et al.* The probabilistic seismic hazard assessment of Germany—version 2016, considering the range of epistemic uncertainties and aleatory variability. *Bull Earthquake Eng* **16**, 4339–4395 (2018). <https://doi.org/10.1007/s10518-018-0315-y>

Headquarters for Earthquake Research Promotion (2017) Strong ground motion prediction method for earthquakes with specified source faults (“Recipe”), April 2017. (in Japanese)

Iervolino I, De Luca F, Cosenza E (2010) Spectral shape-based assessment of SDOF nonlinear response to real, adjusted and artificial accelerograms *Engineering Structures* 32:2776–2792

International Atomic Energy Agency (2015) Strong ground motion simulation based on fault rupture modelling for seismic hazard assessment in site evaluation for nuclear installations, *Safety Report Series*, No. 85, 2015

Irikura K. (1983) Semi-Empirical Estimation of Strong Ground Motions during large earthquakes, *Bull. Disas. Prev. Res. Inst., Kyoto Univ.*, Vol. 33, Part 2, No.298.

Irikura K. (1986) Prediction of strong acceleration motions using empirical Green’s Function. *Proceedings of the 7th Japan Earthq. Eng symposium.*

Irikura K., Kamae K. (1994) Estimation of strong ground motion in broad-frequency band based on a seismic source scaling model and an empirical Green’s function technique, *Annali di geofisica*, Vol. 37, No. 6, pp. 1721-1743.

Irikura K., Miyake H. (2011) Recipe for predicting strong ground motion from crustal earthquake scenarios, *Pure Appl. Geophys*, DOI: 10.1007/s00024-010-0150-9.

Irikura K., Miyake H., Iwata T., Kamae K., Kawabe H., Dalguer L.A. (2004) Recipe for predicting strong ground motion from future large earthquake, *Proceedings of the 13th World Conference on Earthquake Engineering* No. 1371.

Jayaram N, Shome N (2012) A Statistical Analysis of the Response of Tall Buildings to Recorded and Simulated Ground Motions. Paper presented at the 15WCEE, Lisbon, Portugal,

Kanamori H., Anderson L. (1975) Theoretical basis of some empirical relations in seismology, *Bull. Seismol. Soc. Am.*, Vol. 65, No. 5, pp. 1073-1095.

Karimzadeh S, Askan A, Yakut A (2018) Assessment of Simulated Ground Motions in Earthquake Engineering Practice: A Case Study for Duzce (Turkey). In: Dalguer LA, Fukushima Y, Irikura K, Wu C (eds) *Best Practices in Physics-based Fault Rupture Models for Seismic Hazard Assessment of Nuclear Installations*. Springer International Publishing, Cham, pp 265-283. doi:10.1007/978-3-319-72709-7_16

Kotha, S., Bindi, D (2018) A new approach to site classification: Mixed-effects Ground Motion Prediction Equation with spectral clustering of site amplification functions, *Soil Dynamics and Earthquake Engineering*, 110, 318-329 doi: 10.1016/j.soildyn.2018.01.051

Lanzano, G., Sgobba, S., Luzi, L., Puglia, R., Pacor, F., Felicetta, C., D’Amico, M., Cotton, F., & Bindi, D. (2019). The pan-European Engineering Strong Motion (ESM) flatfile: compilation criteria and data statistics. *Bulletin of Earthquake Engineering*, 17(2), 561–582. <https://doi.org/10.1007/s10518-018-0480-z>

Laurendeau, A., P.-Y. Bard, F. Hollender, V. Perron, L. Foundotos, O.-J. Ktenidou, and B. Hernandez, 2018, Derivation of consistent hard rock ($1000 < V_S < 3000$ m/s) GMPEs from surface and down-hole



recordings: analysis of KiK-net data, Bull Earthquake Eng, 16, no. 6, 2253–2284, doi: 10.1007/s10518-017-0142-6.

Lee RL, Bradley BA, Stafford PJ, Graves RW, Rodriguez-Marek A (2020) Hybrid broadband ground motion simulation validation of small magnitude earthquakes in Canterbury, New Zealand Earthquake Spectra 36:673-699 doi:10.1177/8755293019891718

Leonard, M. (2014). Self-Consistent Earthquake Fault-Scaling Relations: Update and Extension to Stable Continental Strike-Slip Faults, Bull. Seis. Soc. Am. 104(6), 2953–2965.

Liu P., Archuleta R., Hartzell S. (2006). Prediction of Broadband Ground-Motion Time Histories: Hybrid Low/High-Frequency Method with Correlated Random Source Parameters. *Bulletin of the Seismological Society of America* 2006; 96 (6): 2118–2130. doi: <https://doi.org/10.1785/0120060036>

Maechling, P. J., F. Silva, S. Callaghan, and T. H. Jordan (2015). SCEC Broadband Platform: System Architecture and Software Implementation, Seismol. Res. Lett., 86, no. 1, doi: 10.1785/0220140125

Morasca, P., D'Amico, M., Sgobba, S., Lanzano, G., Colavitti, L., Pacor, F., Spallarossa, D., 2023. Empirical correlations between an FAS non-ergodic ground motion model and a GIT derived model for Central Italy. *Geophysical Journal International* 233, 51–68. <https://doi.org/10.1093/gji/ggac445>

Morikawa N., Senna S., Hayakawa Y., Fujiwara H. (2008) Application and verification of the 'recipe' to strong-motion evaluation for the 2005 west off Fukuoka earthquake (mw=6.6)", Proc. 14th World Conf. Earthq. Eng., Beijing, paper no. 02-0039.

Motazedian, D., & Atkinson, G. M. (2005). Stochastic finite-fault modeling based on a dynamic corner frequency. *Bulletin of the Seismological Society of America*, 95(3), 995–1010. <https://doi.org/10.1785/0120030207>

Nakano, K., Kawase, H., Matsushima, S. (2019). A study on the site amplifications estimated by generalized inversion technique. *Journal of Japan Association for Earthquake Engineering*, 19(2), 2_1-2_24.

Nakano, K., Matsushima, S., Kawase, H. (2015). Statistical properties of strong ground motions from the generalized spectral inversion of data observed by K-NET, KiK-net, and the JMA Shindokey network in Japan. *Bulletin of the Seismological Society of America*, 105(5), 2662-2680.

Olsen K, Mayhew J (2010) Goodness-of-fit Criteria for Broadband Synthetic Seismograms, with Application to the 2008 M-W 5.4 Chino Hills, California, Earthquake *Seismological Research Letters* - SEISMOL RES LETT 81:715-723 doi:10.1785/gssrl.81.5.715

Otarola, C., & Ruiz, S. (2016). Stochastic generation of accelerograms for subduction earthquakes. *Bulletin of the Seismological Society of America*, 106(6), 2511–2520. <https://doi.org/10.1785/0120150262>

Oth, A., D. Bindi, S. Parolai, and D. D. Giacomo, 2011, Spectral Analysis of K-NET and KiK-net Data in Japan, Part II: On Attenuation Characteristics, Source Spectra, and Site Response of Borehole and Surface Stations Spectral Analysis of K-NET and KiK-net Data in Japan, Part II, *Bulletin of the Seismological Society of America*, 101, no. 2, 667–687, doi: 10.1785/0120100135.

Oth, A., H. Miyake, and D. Bindi, 2015, On the Relation of Earthquake Stress Drop and Ground Motion Variability, AGU Fall Meeting Abstracts, 51, S51A-2641.

Pagani M, Monelli D, Weatherill G, Danciu L, Crowley H, Silva V, *et al.* OpenQuake Engine: An Open Hazard (and Risk) Software for the Global Earthquake Model. *Seismological Research Letters* 2014; **85**(3): 692–702. DOI: 10.1785/0220130087

Petrone F, Abrahamson N, McCallen D, Miah M (2021) Validation of (not-historical) large-event near-fault ground-motion simulations for use in civil engineering applications *Earthquake Engineering & Structural Dynamics* 50:116-134 doi:<https://doi.org/10.1002/eqe.3366>



Pilz, M., F. Cotton, H. N. T. Razafindrakoto, G. Weatherill, and T. Spies (2021). Regional broadband ground-shaking modelling over extended and thick sedimentary basins: An example from the Lower Rhine Embayment (Germany). *Bull. Earthq. Eng.*, 19 (2), 581-603

Pilz, M., Cotton, F., Zhu, C., Nakano, K., & Kawase, H. (2022). Deriving Site Effect-Free Hard-Rock Time Histories in Japan from the Generalized Inversion Technique. *Bulletin of the Seismological Society of America*, doi: <https://doi.org/10.1785/0120220155>

Pizzi, A., A. Di Domenica, F. Gallovič, L. Luzi, and R. Puglia (2017). Fault segmentation as constraint to the occurrence of the main shocks of the 2016 Central Italy seismic sequence, *Tectonics*, 36, doi: 10.1002/2017TC004652.

Razafindrakoto, H. N. T.; Cotton, Fabrice; Weatherill, Graeme; Bindi, Dino (2022): Simulation Database of Broadband Ground-Motion Time Histories for the Rhine Graben Area. V. 1.0.0. GFZ Data Services. <https://doi.org/10.5880/GFZ.2.6.2022.004>

Razafindrakoto, H. N. T.; Fabrice Cotton, Dino Bindi, Marco Pilz, Robert W. Graves, Sanjay Bora (2021). Regional Calibration of Hybrid Ground Motion Simulations in Moderate Seismicity Areas: Application to the Upper Rhine Graben. *Bull. Seismol. Soc. Am.* 111 (3): 1422–1444. doi: <https://doi.org/10.1785/0120200287>

Rezaeian S, Zhong P, Hartzell S, Zareian F (2015) Validation of Simulated Earthquake Ground Motions Based on Evolution of Intensity and Frequency Content *Bulletin of the Seismological Society of America* 105:3036-3049

Roten, D., Fäh, D., Cornou, C., Giardini, D. (2006). Two-dimensional resonances in Alpine valleys identified from ambient vibration wavefields. *Geophysical Journal International*, 165(3), 889-905.

Ruiz, S., Ojeda, J., Pastén, C., Otarola, C., & Silva, R. (2018). Stochastic strong-motion simulation in borehole and on surface for the 2011 m w 9.0 tohoku-oki megathrust earthquake considering p, sv, and sh amplification transfer functions. *Bulletin of the Seismological Society of America*, 108(5), 2333–2346. <https://doi.org/10.1785/0120170342>

Saint-Mard Ludvine, Ground motion simulation for seismic hazard: the Irikura recipe (2019) EDF Internal Report (6125-1723-2019-03856-EN)

Saragoni RG, Hart GC. Simulation of Artificial Earthquakes. *Earthquake Engineering & Structural Dynamics* 1973; 2: 249–267.

Sawada, S., Irikura, K., Kudo, K., Okada, H., & Sasatani, T. (1998). Phase characteristics on site amplification of layered ground with irregular interface. *The Effects of Surface Geology on Seismic Motion*, 1009-1013.

Shible, H. et al., 2022, GITEC: A Generalized Inversion Technique Benchmark, *Bulletin of the Seismological Society of America*, doi: 10.1785/0120210242.

Shible, H., 2021, Development of a new approach to define reference ground motions applicable to existing strong-motion databases, *Earth Sciences*, Université Grenoble Alpes.

Si H., Midorikawa S. (1999) New attenuation relationships for peak ground acceleration and velocity considering effects of fault type and site condition, *Journal of Structural and Construction Engineering*, 523, 63–70 (in Japanese with English abstract).

Somerville P., Irikura K, Graves R., Sawasa S., Wald D., Abrahamson N., Iwasaki Y., Kagawa T., Smith N., Kowada A. (1999) Characterizing crustal earthquake slip models for the prediction of strong ground motion, *Seism. Research letters*, Vol. 70, No. 1.

Stafford, P. J. (2014, 03). Crossed and Nested Mixed-Effects Approaches for Enhanced Model Development and Removal of the Ergodic Assumption in Empirical Ground-Motion Models, *Bulletin of the Seismological Society of America* 104(2), 702–719.



Star LM, Stewart JP, Graves RW (2011) Comparison of Ground Motions from Hybrid Simulations to NGA Prediction Equations Earthquake Spectra 27:331-350 doi:10.1193/1.3583644

Tao, Y., Rathje, E. (2020). The Importance of Distinguishing Pseudoresonances and Outcrop Resonances in Downhole Array Data. *Bulletin of the Seismological Society of America*, 110(1), 288-294.

Thompson, E. M., Baise, L. G., Tanaka, Y., Kayen, R. E. (2012). A taxonomy of site response complexity. *Soil Dynamics and Earthquake Engineering*, 41, 32-43.

Tsioulou A, Taflanidis AA, Galasso C (2019) Validation of stochastic ground motion model modification by comparison to seismic demand of recorded ground motions *Bulletin of Earthquake Engineering* 17:2871-2898 doi:10.1007/s10518-019-00571-x

Van Houtte, C. , S. Drouet, and F. Cotton, 2011, Analysis of the Origins of κ (Kappa) to Compute Hard Rock to Rock Adjustment Factors for GMPEs Analysis of the Origins of κ (Kappa) to Compute Hard Rock to Rock Adjustment Factors for GMPEs, *Bulletin of the Seismological Society of America*, 101, no. 6, 2926–2941, doi: 10.1785/0120100345.

Wang, N., Takedatsu, R., Olsen, K. B., & Day, S. M. (2019). Broadband ground-motion simulation with interfrequency correlations. *Bulletin of the Seismological Society of America*, 109(6), 2437–2446. <https://doi.org/10.1785/0120190136>

Zhong K, Lin T, Deierlein GG, Graves RW, Silva F, Luco N (2021) Tall building performance-based seismic design using SCEC broadband platform site-specific ground motion simulations *Earthquake Engineering & Structural Dynamics* 50:81-98 doi:<https://doi.org/10.1002/eqe.3364>

8. Appendix

8.1. SCEC platform

The Southern California Earthquake Center (SCEC) Broadband Platform (BBP) is a collection of open-source scientific software modules that can simulate broadband (0-20+ Hz) ground motions for earthquakes at regional scales, compare simulation results between methods, and validate simulation results against observations. BBP software modules include kinematic rupture generators, low- and high-frequency seismogram synthesis methods that model the propagation of seismic waves through 1D layered velocity structures, site-effects modules, ground motion intensity measure calculations, and ground motion goodness-of-fit tools. The BBP has been developed over the last ten years as a collaborative project involving geoscientists, earthquake engineers, including graduate students, researchers and practitioners, and the SCEC research computing group.

The latest Broadband Platform release, version 19.8.0, is available for download on GitHub. The SCEC BBP software can be compiled and run on Linux systems using open-source compilers and libraries. It features an interactive command-line interface that guides users through the process of setting up validation or scenario simulation runs. Capabilities also include the ability for users to automate the simulation setup steps through scripts, making it easier and efficient supporting the submission of sets of simulations to computer clusters.

(description from <https://www.scec.org/article/697>)

Left: List of scientific methods available in the SCEC Broadband Platform. Each simulation method is created by combining a specific set of scientific modules. Right: The GP method (as example) includes a rupture generator, low and high-frequency modules, and site response module.

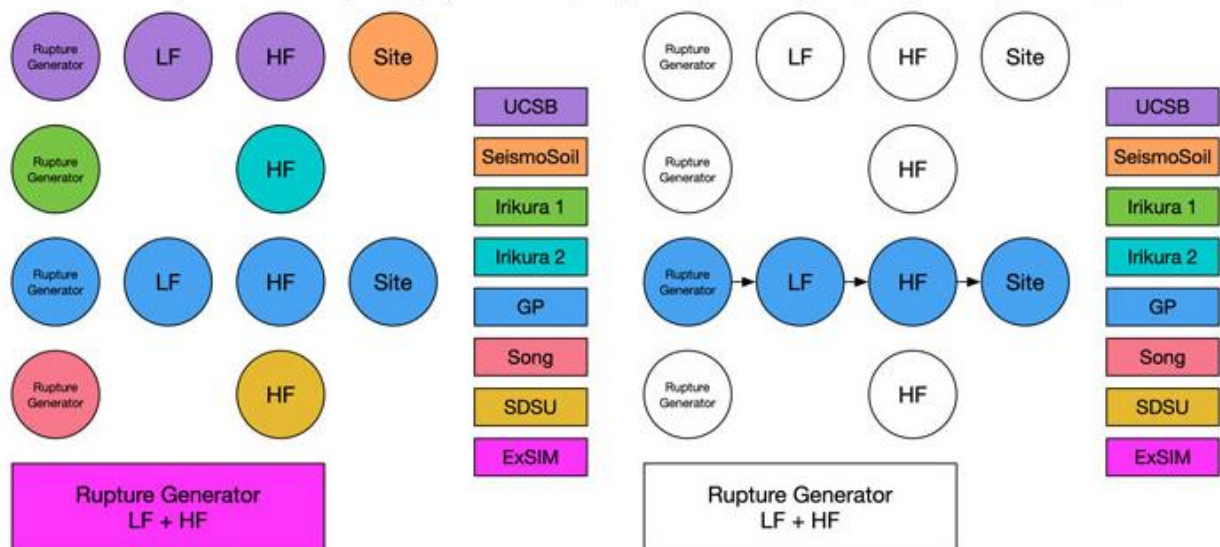


Figure A1 : Modelling options and opensource modules available within SCEC broadband platform



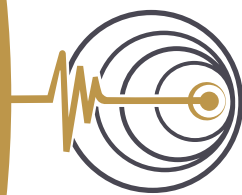
8.2. Details on the Seister approach and application



Methods and tools innovations for seismic risk assessment - METIS project

**Simulations of region-specific
ground motions at bedrock by
combining spectral
decomposition and empirical
Green's functions approaches**

Rapport N° : STR_GDS_20P39_03



SEISTER
SEISMIC ENGINEERING SOLUTIONS

Date : 29/03/2023

Préparé pour :

**GÉODYNAMIQUE
& STRUCTURE**



METIS

Seismic Risk Assessment
for Nuclear Safety

Methods and tools innovations for seismic risk assessment - METIS project

Simulations of region-specific ground motions at bedrock by combining spectral decomposition and empirical Green's functions approaches

STR_GDS_20P39_03

Client

Géodynamique & Structure
Immeuble CAP SUD
106 Avenue Marx Dormoy
92120 Montrouge - France

Email

Pierre-alain.naze@geodynamique.com

Supplier

SEISTER SAS
Le Quartz
58 Chemin de la Justice
92290 Châtenay-Malabry
France

Email

David.Baumont@seister.fr

Purchase order

N° GDS-22-001 dated of 07/01/2022

Report SEISTER n° :

STR_GDS_20P39_03

Version n° : 0

Number of pages : 47

	Authors	Verification	Approbation
Date	28/03/2023	29/03/2023	29/03/2023
Name	Shible. H., Ameri G., Maharjan S., Baumont D.	G. Ameri	D. Baumont

Version	Date	Status	Description
0	29/03/2023	Final	Final report on METIS project

Table of content

Table of content	4
List of figures	5
List of tables	8
1. Introduction	9
2. General methodology	10
2.1 Source and site spectral modeling	11
2.2 Ground motion simulations using the EGF technique	12
3. Application to a case study	14
3.1 Evaluation of source and site terms	15
3.2 Correction of Empirical Green's functions (EGFs)	17
3.3 Source modeling for target magnitudes	22
3.4 Results for selected target magnitudes	25
3.4.1 Comparison with empirical GMM	25
3.4.2 Comparison with observations from similar events	31
3.4.3 Simulated time histories	33
4. Discussion and conclusions	35
5. References	37
A. Appendix	40
A.1 Definition of the usable frequency range	40
A.2 Searching for EGFs	42
A.3 Sensitivity tests on the EGF selection procedure	43
A.4 On the modelling trade-off between source and site terms	45

List of figures

Figure 3.1 Map showing the ESM subset of stations and earthquakes used for the GIT application (DATA _{GIT}). The black lines represent the source-site ray paths in the dataset.	14
Figure 3.2: The magnitude distribution versus epicentral distances R_{EPI} (a) and focal depths (b) for the defined ESM subset DATA _{GIT} , used for GIT application.	15
Figure 3.3: (a) Source terms of a selection of earthquakes recorded at 2 stations GNU and MOMA, (b,d) their respective site responses as obtained from GIT. (c,e) The source-site combination at each station. The gray and black colors correspond to inversions performed with REF1 and REF2 reference conditions, respectively.	16
Figure 3.4:(a) The magnitude-distance distribution of selected recordings to construct the database for EGF simulations (DATA _{EGF}). (b) Magnitude-depth distribution of these recordings. The color scale represents the distance to the METIS site.	18
Figure 3.5: The correction of source and site effects applied on the 2 components of an example recording. (a) The correction function is used to remove source and site effects. (b) The FAS of the original signal and the corrected one.	19
Figure 3.6: The original time history of a record is shown (in black) for both components E and N. The source-site corrected time history is also shown (in red).	19
Figure 3.7: The FAS of combined horizontal components of the source-site corrected signals, passing through outlier-detection procedure before being input for EGF simulations. The identified outlier in the distance bin 1-3 km is highlighted in red. The blue dotted lines correspond to the median \pm standard deviation, the limits beyond which the signals are flagged outliers. The dashed black lines show the frequency range f_{min} - f_{max} in which source-site corrected recordings are considered reliable.	21
Figure 3.8: (left) Map showing the source-site ray paths of DATA _{EGF} from the initial dataset. Red ray paths correspond to outliers identified and excluded from simulations. (right) Magnitude-distance distribution of DATA _{EGF} with red triangles representing the identified outliers.	21
Figure 3.9: Example of 3D view of simulated rupture geometry for a Mw=5.5 event. The final displacement on the rupture is shown for a single simulation. The red rectangle represents the surface projection of the rupture and the vertical dashed red line points the rupture nucleation. The brown circles represent the hypocenter and the epicenter of the EGF event (EMSC-20161031_0000053). Triangles show the position of the considered stations. The blue rectangle represents the fault plane hosting the randomly generated rupture models.	23
Figure 3.10: Example realizations of slip distributions (left) generated from the k^{-2} source model and hypocenter locations and related rupture times (right) for the Mw=5.5 scenarios. Note the different dimensions of the ruptures. The hypocenter is assumed to be in the lower half of the rupture (Mai et al., 2005).	23
Figure 3.11: Representative rupture parameters obtained for the 30 rupture models for Mw 5.0, 5.5 and 6.0 earthquakes.	24
Figure 3.12: Absolute source time functions generated by the k^{-2} method (left) and corresponding source spectra (right) for the Mw=5.5 scenarios (30 simulation, Nsim). The Brune source spectra for the minimum (0.67 MPa), mean (2.3 MPa) and maximum (6.2 MPa) stress drop values are also reported (in black) for comparison as well as the mean of the simulated source spectra (in gray).	24
Figure 3.13 : Simulated spectral acceleration (PSA) for Mw=5 (left) and M=6 (right) as a function of the Joyner-Boore distance (Rjb) for three spectral periods (T=0.01 s, 0.2 s and 2 s). The gray circles represent the geometric mean of the horizontal components, and the vertical black bars represent the mean and standard deviation of simulated values over distance bins. Stations within the surface projection of the rupture are plotted at Rjb = 0.1 km. The GMM for Italy (ITA18) by Lanzano et al. (2019) is plotted in light green (median \pm 1 standard deviation) considering a Vs30=800 m/s and normal fault mechanism. The median ITA18 adjusted for reference rock conditions according to Lanzano et al. (2022) is shown in red.	27
Figure 3.14 : Simulated spectral acceleration (PSA) for Mw=5 (left) and M=6 (right) as a function of the Joyner-Boore distance (Rjb) for three spectral periods (T=0.01 s, 0.2 s and 2 s). The gray circles represent the geometric mean of the horizontal components, and the vertical black bars	

represent the mean and standard deviation of simulated values over distance bins. Stations within the surface projection of the rupture are plotted at $R_{jb} = 0.1$ km. The European GMM adopted by Weatherill et al. (2020) is plotted in red for a $V_{s30}=1100$ m/s and considering the 9 branches of the logic tree proposed to capture uncertainties in median ground motion for attenuation cluster 3.28

Figure 3.15 : Simulated response spectra (in gray) for the $M_w=5$ (left) and $M_w=6$ (right) scenarios at 20 km (stations at distances between 15 km to 25 km are used) for the geometric mean of horizontal components. The mean ± 1 standard deviation of the simulated spectra is shown in black. The GMM for Italy (ITA18) by Lanzano et al. (2019) is plotted in green (median ± 1 standard deviation) considering a $V_{s30} = 800$ m/s and normal fault mechanism. The median ITA18 adjusted for reference rock conditions according to Lanzano et al. (2022) is shown in red.29

Figure 3.16 : (upper-left) simulated response spectra (in gray) for the $M_w=5$ scenarios at 20 km (stations at distances between 15 km to 25 km are used) for the geometric mean of horizontal components. The mean ± 1 standard deviation of the simulated spectra is shown in black. The mean spectrum obtained for each EGF is shown in color. (upper-right) the same as in upper-left but in terms of Fourier amplitude spectra (FAS). (lower-left) Fourier amplitude spectra of the EGF (after deconvolution for source and site terms). (lower-right) Map of the adopted EGF paths for $M_w=5$ and 20 km (in colors) compared overall set of EGF paths (in gray). Circles and triangles represent epicenters and stations respectively.30

Figure 3.17 : Comparison between simulated horizontal significant durations (D5-95: time elapsed between 5% and 95% of the total Arias Intensity) as a function of distance for $M_w=5$ (left) and $M_w=6$ (right) scenarios and the predictions by the Sandikkaya and Akkar (2017) empirical model for the Pan-European region (in blue, median ± 1 standard deviation) for $V_{s30}=800$ m/s and normal-fault mechanism.31

Figure 3.18 : Comparison between simulated (gray circles) and observed (red triangles) spectral acceleration (PSA) for $M_w=5$ (left) and $M_w=6$ (right) as a function of the Joyner-Boore distance (R_{jb}) for three spectral periods ($T=0.01$ s, 0.2 s and 2 s). The vertical black bars represent the mean and standard deviation of simulated values over distance bins. Stations within the surface projection of the rupture are plotted at $R_{jb} = 0.1$ km. The observed data are for ± 0.1 magnitude units with respect to the target magnitudes.32

Figure 3.19 : Comparison between simulated (in gray) and observed (in red) response spectra for $M_w=5$ (left), $M_w=5.5$ (center) and $M_w=6$ (right) scenarios at 20 km (spectra distances between 15 km to 25 km are used and, for observations only, magnitudes within ± 0.1 units from the target) for the geometric mean of horizontal components. The median ± 1 standard deviation of the simulated spectra is shown in black. The thick red curve represents the mean of the observed spectra. See the text for further details on the selected data.33

Figure 3.20: Example of simulated acceleration (left) and velocity (right) time-histories (east-west component) for a $M_w=6.0$ scenario at increasing distances (station code and R_{jb} are indicated in the figure). The original EGF event is EMSC-20161031_0000053.34

Figure 3.21 : Example of simulated acceleration (left) and velocity (center) time histories (east-west component) for a $M_w=6.0$ scenario above the fault ($R_{jb}=0$ km) considering station IT.ACC and EGF event EMSC-20161112_0000066. The selected simulations are for three values of stress drop ($\#30=2.1$ MPa, $\#15=4.9$ MPa and $\#13=0.7$ MPa). The corresponding response spectra are presented in the right-most plot and compared with ensemble of simulations using this EGF for $M_w=6$ and $R_{jb}=0$ km.34

Figure 5.1: The gain of a 4th-order Butterworth filter at different f_{cHP} with fixed $f_{cLP}=30$ Hz (upper figure), and at different f_{cLP} with fixed $f_{cHP}=0.1$ Hz (lower figure). The dashed lines correspond to the frequency band unaffected by the filter edge effects (gain>99%).40

Figure 5.2: Distribution of the number of recordings per station versus the distance to the METIS site. The initial number of all recordings is represented by circles, recordings filtered to keep magnitudes <4.0 and $R_{EPI} < 50$ km by triangles, and recordings filtered to keep magnitudes <5.0 and $R_{EPI} < 100$ km by squares. The blue, green and red colors mark the distance ranges 0-100 km, 100-120 km and 120-140 km, respectively.42

Figure 5.3: A sensitivity test on the selection procedure, by modifying the condition on the frequency band between (1) $f_{HP}-f_{LP}=0.1-30$ Hz, (2) $f_{min}-f_{max} = 0.3-25$ Hz, and (3) $f_{min}-f_{max}= 0.1-30$ Hz.	43
Figure 5.4: A sensitivity test on the selection procedure, by modifying the definition of bins between (1) magnitude and distance binning and (2) distance binning only.	44
Figure 5.5 (a) Source terms of all earthquakes in the considered dataset for GIT. (b) site amplification terms obtained for all sites in the dataset. The average term in each case is marked in dashed lines. The gray lines correspond to “REF1” reference condition, while the black lines correspond to “REF2” conditions.	45
Figure 5.6 : (a) The source terms of earthquakes (magnitude <4) recorded at 5 stations in the dataset, (b) their respective site responses as obtained from GIT. (c) The source-site combination at each station. The gray and black colors correspond to inversions performed with REF1 and REF2 reference conditions, respectively.	47

List of tables

Table 5-1: Summary of filter corner frequencies (f_{cHP} and f_{cLP}) and usable frequencies (f_{min} and f_{max}). The ratio of f_{min}/f_{cHP} and f_{cLP}/f_{max} is also noted.	41
--	----

1. Introduction

Estimating earthquake ground motions at reference bedrock conditions is a major challenge in seismic hazard assessment. This is needed, either because the target site is located on outcropping bedrock or because soil response will be subsequently integrated by soil response analysis. In both cases, the application of standard empirical ground-motion models (GMMs) to estimate reference bedrock motion may provide biased estimates. In fact, the vast majority of strong-motion databases contain earthquake recordings of stations installed on soil or soft-rock sites while very few stations are on hard-rock sites. This prevents having reliable ground motion estimates at bedrock, especially in the magnitude-distance range of interest for the seismic hazard.

Several attempts have been made in the last decades to overcome the issue of deriving GMMs for reference conditions. Many of these attempts aimed to adjust existing models from soft-rock to reference-rock conditions through proxy-based corrections (Cotton et al., 2006; Houtte et al., 2011; Biro and Renault, 2012; Ameri et al., 2017; Lanzano et al., 2022). Others addressed the problem differently, mainly by deconvolving time histories from site effects under the 1D assumptions before GMM developments, resulting in corrected hard-rock motion (Cadet et al., 2012; Laurendeau et al., 2018; Shible et al., 2018). Furthermore, the detailed review of hard-rock motion predictions by Bard et al. (2020) resulted in several recommendations, one of which is the use of generalized inversions to robustly predict and remove site effects. Following these recommendations, Shible (2021) extended the deconvolution approach of surface recordings beyond the limitation to 1D conditions through the use of site terms from generalized inversion techniques. Though the results of the deconvolution approach are promising, the potential lack of data in specific regions remains an obstacle to advancing in this direction of empirical modelling.

Because of such paucity of data, alternatives to empirical GMMs should be considered to estimate reference ground motion for hazard analyses. One alternative is to simulate earthquake ground motions using for example 3D physics-based approaches that are capable of generating synthetic time-histories at bedrock considering a local or regional 3D crustal model and an extended-source model. However, such approaches still suffer from the limited knowledge of the propagation medium which prevents, in most cases, obtaining time histories covering a sufficiently large frequency band (0.1-20 Hz). Another particularly appealing approach is the Empirical Green's Functions (EGF) simulation method which combines empirical data and theoretical models. The basic idea of the EGF approach is to interpret recordings of small events at the site of interest as reasonable approximations of Green's functions (describing the impulse response of the medium) and to convolve them suitably with more or less complex source model to simulate time histories that correspond to larger earthquakes.

The power of this technique lies in its ability to map the site- and path-specific effects into the ground-motion field, providing a local ground-motion model without the need for computationally expensive approaches to simulate 3D wave propagation. The counterpart of this approach in most applications is that the site response is only modelled for its linear behaviour, while soil nonlinearity potentially observed for large ground motions is not accounted for. In an application to hard-rock sites, this

limitation is, however, not of concern. Nonetheless, the application of the EGF technique to obtain bedrock time histories remains challenging because site effects are already included in the recordings at each site.

To comply with the global objectives of the METIS project, we aim to develop a database of reference rock ground motion simulations to be used as input motion for site effect modelling. Taking into account the lessons learned from last decade PSHA studies, we also intend through this study to account to the possible extent for the local and regional crustal properties as a step towards partially non-ergodic seismic hazard assessment taking the benefits of the available earthquake recordings in the region.

In this contribution, we propose a method to simulate reference bedrock time histories by combining spectral decompositions of ground motion with EGF simulation techniques. The proposed method, which is built upon well-known approaches, is briefly described in section 2. Section 3 presents an application to a case study in a moderate-seismicity region characterized by limited amount of local data in order to demonstrate the advantages of the proposed approach. Finally some discussion and future perspectives are presented in section 4.

2. General methodology

The proposed methodology relies first on the nonparametric spectral decomposition approach (also called the generalized inversion technique, GIT) that has been developed and used in many studies to separate the contribution of source, path, and site terms (e.g., Castro et al., 1990; Oth et al., 2015, 2011; Ameri et al., 2020; Shible et al., 2022a). We remove the decomposed isotropic source and site effects from the recordings, through the deconvolution in the Fourier domain similar to Shible (2021), in order to derived deconvolved EGF to be used in the simulations. Then, we apply the EGF simulation method developed by Dujardin et al. (2020) to couple the deconvolved EGF with a k^{-2} kinematic rupture model.

The workflow of the proposed methodology is as follows:

1. A dataset of recordings is collected for the target region. The region should be large enough to allow a sufficient number of data for the application of the GIT,
2. GIT is applied to the selected data to separate source, path, and site terms from the observed Fourier spectra. Generally, the attenuation terms are robustly determined in the adopted nonparametric GIT approach and unaffected by site/source constraints applied to inversions (Bindi and Kotha, 2020; Oth et al., 2011). This allows for obtaining a robust combined term of source and site effects,
3. Deconvolved EGF (representing only the path term) are obtained by correcting the observed records by source and site terms estimated by GIT. This is done for a sub-set of EGF selected to be used in the simulations in order to sample the region around the target site,

4. For each target magnitude (e.g., $M_w=6$) a set of kinematic rupture models following a k^{-2} slip distribution and approximating an ω^{-2} source spectrum are generated according to the approach presented by (Dujardin et al., 2020). Uncertainties in kinematic source parameters (e.g., slip distribution, rupture velocity, hypocentral location, stress drop, rupture dimensions) are sampled,
5. The source time function and the EGF associated with each sub-fault are then convolved to produce 3-component time histories that combine a simulated source contribution in addition to the empirical path effect. Because of the absence of site effects, the simulated ground motions are representative of reference bedrock conditions.

The region-specific, site-effect-free dataset produced by this approach can be used alone or in combination with existing empirical datasets to adjust existing GMMs, derive new GMMs, or select hazard-consistent time histories to be used in soil or structural response analysis.

2.1 Source and site spectral modeling

Generalized spectral inversion schemes are based on the principle of separation of the Fourier amplitude spectrum into three main components, as indicated in Eq(1):

$$FAS_{ij}(f) = E_j(f) A_{ij}(r_{ij}, f) S_i(f) \quad (1)$$

where FAS_{ij} is the Fourier amplitude spectrum at each frequency f recorded at site i for event j , $E_j(f)$ is the source function, $A_{ij}(r_{ij}, f)$ is the path contribution over the event-site distance r_{ij} , and $S_i(f)$ is the site response term.

Applying logarithm to Eq(1), we obtain a linear system of the form $A \cdot x = b$, where b is the data vector, x is the solution of the system, and A describes the system matrix (e.g. Andrews, 1986; Castro et al., 1990). Following its definition, the system has two undetermined degrees of freedom, which can be solved if two constraints are added in the inversion. The first constraint is often applied to one (site term = 1) or several site responses (mean of site terms =1), while the second one is applied to the attenuation functions by defining a reference distance R_0 at which $A(r = R_0, f) = 1$ at all frequencies f . Solving the linear system leads to non-parametric terms, and it is often called as a non-parametric inversion scheme (Bindi et al., 2009; Oth et al., 2011, 2015; Bindi and Kotha, 2020).

As discussed further in this paper, we apply the inversion scheme to a region covering the METIS case study site to determine the source spectra $E(f)$ for each earthquake, the attenuation curves as functions of the hypocentral distance r at each frequency $A(r, f)$, and the site amplification $S(f)$ as a function of frequency for each site in the dataset. The source and site terms are then combined to form a non-parametric correction term, which is used to derive the EGFs prior to simulations. In this study, we do not intend provide a detailed interpretation of inversion results in terms of source or attenuation parameters and as such we will focus on the non-parametric functions.

2.2 Ground motion simulations using the EGF technique

According to the representation theorem (Aki and Richards, 2002), assuming a rectangular fault rupture characterized by length L and width W , the simulated acceleration $U(\vec{r}, t)$ for a station at position \vec{r} can be written as:

$$U(\vec{r}, t) = \int_0^L \int_0^W R(x, y; t) \cdot FG_{x,y}(\vec{r}, t) dx dy$$

where $R(x, y; t)$ represents the contribution to the moment rate function at position (x, y) on the fault, and $FG_{x,y}(\vec{r}, t)$ is the Green's function in acceleration associated to the same subfault.

Originally, Hartzell (1978) proposed to use small-magnitude events as EGF which implicitly allows for the complexity of the propagation and linear site effects over a broad frequency range. The simulation approach adopted in this study couples the EGF technique with a kinematic description of the extended fault assuming a k^{-2} slip model. We provide here a general overview of the approach and detail the specific choices made for the present application referring to Dujardin et al. (2018, 2020) for further readings on the general formulation of the method.

1. **Rupture Area Dimensions.** The seismic moment M_0 , the focal mechanism, and the size of the fault on which the rupture is expected are postulated. Then, the size of the rupture area on this fault, which is assumed to be rectangular, is automatically calculated from the stress drop ($\Delta\sigma$) and the seismic moment M_0 , as originally proposed by Herrero and Bernard (1994). The dimensions of the rupture area are derived as follows. From the input stress drop, the theoretical corner frequency (f_c) is derived following the Brune (1970) model. Then, according to the following approximation (Hanks, 1979; Hanks and McGuire, 1981): $f_c = 1/T_{Rup}$, where $T_{Rup} = D_{Rup}/V_r$ is the rupture duration and V_r is the rupture velocity (m/s), we derived the length (L) and width (W) of the rupture area by assuming that the characteristic size of the rupture is $D_{rup} = \sqrt{L^2 + W^2}$. Thus, only the ratio between L and W is necessary to derive the dimensions of the rupture area. V_R depends on V_S in the vicinity of the fault, and it commonly varies between $0.7 \cdot V_S$ and $0.85 \cdot V_S$ (Heaton, 1990). V_S in the vicinity of the fault is also used to derive the differences in travel times between the different parts of the rupture area and the target station. Both V_S and the ratio between V_S and V_R are parameters to be chosen by the user.
2. **Static Slip Generation.** Once rupture dimensions are defined, the static slip distributions of the source are generated in two steps, as the low and high-frequency parts of the static slip are constrained separately. The low-frequency part is set to a constant value over the rupture area (the mean slip derived from the seismic moment and rupture area). The high-frequency part is defined in the wavenumber domain following Herrero and Bernard (1994) and should have a k^{-2} decay at high wavenumbers.

3. Spatial Sampling. The rupture area is discretized into sub-faults where their sizes are defined according to the target maximum frequency (f_{kmax}) of the simulations which is 20 Hz in our application.

$$SF_{dim} = \frac{V_r}{2 \times f_{kmax}}$$

Note that this approach differs from the EGF formulation based on scaling laws between large and small earthquakes, in which the sub-faults size depends on the EGF seismic moment (e.g., Irikura and Kamae, 1994; Miyake et al., 2003).

4. Rupture kinematics. The rupture kinematics is defined based on the position of the rupture starting point and of the rupture velocity. The slip rate function is defined as the sum of the isosceles triangles as proposed by Hisada (2001). The slip rate function can be parameterized by three parameters: the slip rate function duration τ_{rise} (or rise time), the number of summed triangles (Nv) and Ar which corresponds to the ratio of the area of the j+1th triangle with respect to the ratio of the jth triangle (i.e. $Ar = A_{j+1}/A_j$). For the present application, we use Nv = 4 and $Ar = \sqrt{2}$ (Dujardin et al., 2020). Hisada (2001) showed that it has two characteristics frequencies: $f1 = 1/(2\tau_{rise})$ and $fmax = 1/\tau_1$, where τ_1 is the duration of the first triangle. τ_{rise} is supposed to be constant over the rupture area, and is defined according to Somerville et al. (1999):

$$\tau_{rise} = 2.03 \times 10^{-9} (M_0)^{1/3}$$

Finally, the absolute source time function is obtained by summing the contribution of each sub-fault.

5. Green's function adjustments. Several adjustments can be applied in order to correct the EGF for amplitude and time differences when it is shifted from its original location to the subfault position (Dujardin et al., 2018; 2020). Moreover, a radiation pattern correction is also proposed by Dujardin et al. (2020) when the focal mechanisms of the EGF and of the target event are not the same. In this application, we corrected the EGF in amplitude for geometrical and anelastic attenuation (Qs) based on the GIT results. However, we did not use the radiation pattern correction because the information on the focal mechanism of the small events was not available. The simulated target events are thus assumed to have the same focal mechanism as the small events selected for the EGF. This appears reasonable since the selected small events are considered as representative of the event type that may occur close to the target site. The correction for the travel-time difference of the EGF is tested but finally not adopted because of the relatively small dimensions of the rupture and thus the small the time-shift of the EGF (also note that as discussed in the following the simulated ruptures are assumed to be centered on the EGF hypocenter).
6. Time series generation. The source time function and the EGF associated with each sub-fault are then convolved and integrated over the fault in order to obtain ground motions from the simulated target earthquake.

3. Application to a case study

The case study within the METIS project corresponds to a hypothetical site located on the western coast of Italy, few tens of kilometers north of Rome. Ground motion modelling study should thus be as much as possible representative of the ground motion characteristics observed in the region around the case study.

The data selection rely on the earthquake recordings as close as possible to the target site as reported in the ESM database (Engineering Strong-Motion Database, Luzi et al., 2016; Lanzano et al., 2019) which contains a large amount of strong motion data recorded in Italian regions (Lanzano et al., 2019).

In this study, we apply the GIT on a dataset that includes the available stations close to study case. We performed two data selections:

- A first selection is dedicated for the GIT analysis, and it includes a wide selection of stations and earthquakes as shown in Figure 3.1. We note here that very few recordings in the ESM data are observed in the 100 km range around the site. We denote this ESM subset as $DATA_{GIT}$,
- A second selection is dedicated for EGF recordings, which is used for EGF simulations in this study as described afterward. We denote this ESM subset as $DATA_{EGF}$.

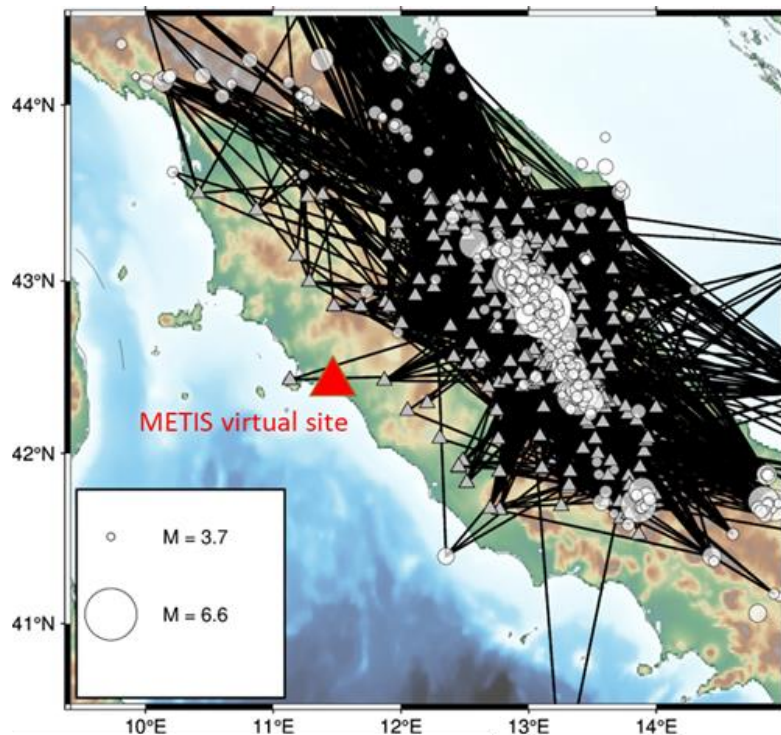


Figure 3.1 Map showing the ESM subset of stations and earthquakes used for the GIT application ($DATA_{GIT}$). The black lines represent the source-site ray paths in the dataset.

Note that time histories provided by ESM are not raw data but were processed as described in details in several publications (e.g., Luzi et al., 2016; Lanzano et al., 2019) following Paolucci et al. (2011). An

important aspect of ESM data processing for empirical modeling is related to the usable frequency bandwidth. In fact, data processing included application of a 4th order Butterworth band-pass filter over the frequency range $[H_p \text{ } L_p]$, where the “Hp” and “Lp” are the high-pass and low-pass corner frequencies, respectively. These corner frequencies were determined following Paolucci et al. (2011) and reported in the ESM flatfiles. We consider in our analysis that the largest usable frequency bandwidth can be defined as $[f_{min} = 1.3H_p ; f_{max} = L_p/1.3]$, which allows to avoid edge-effects of the filter. The definition of the usable frequency band is further discussed in Appendix A.1.

3.1 Evaluation of source and site terms

We apply preliminary selection criteria on ESM data to define DATA_{GIT}. The imposed criteria are as follows:

- We discard all records with epicentral distance (R_{EPI}) > 250 km to avoid the impact of long-distance attenuation on the results of the inversions,
- Only events at depths < 40 km are kept to restrict the analysis to shallow crustal earthquakes,
- All events with missing depth information are discarded since the depth information is needed to calculate hypocentral distances (R_{hypo}), usually used to approximate the ray path in GIT,
- The minimal number of recordings per station and event is set to 5.

The criteria imposed result in the data magnitude-distance distribution shown in Figure 3.2. The subset appears to include enough recordings at different magnitudes and distance ranges, covering magnitudes between 3.5 and 6.5 and R_{EPI} starting from a few kilometers. The depths of considered earthquakes are dispersed between a few kilometers and 40 km. DATA_{GIT} contains 10113 recordings in total.

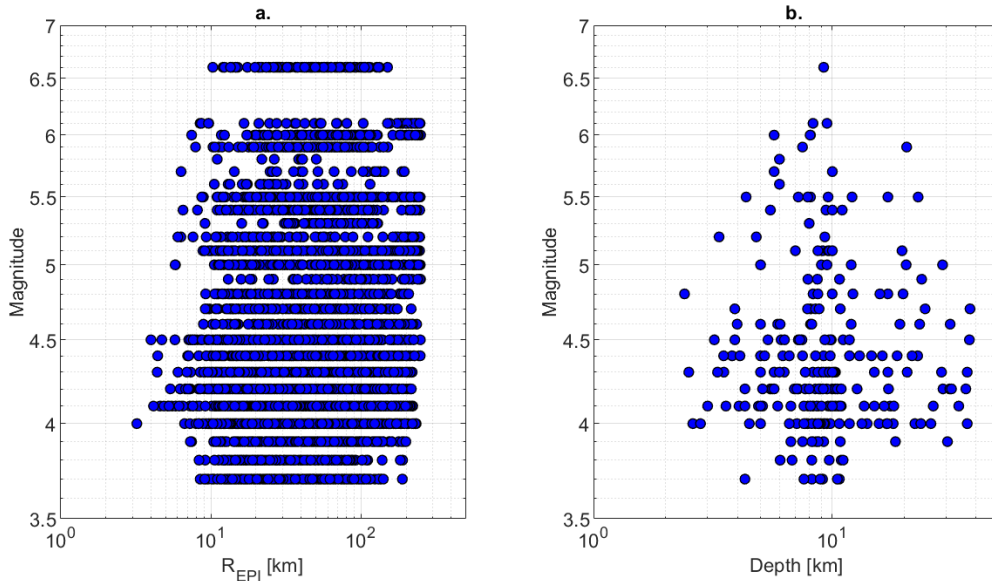


Figure 3.2: The magnitude distribution versus epicentral distances R_{EPI} (a) and focal depths (b) for the defined ESM subset DATA_{GIT}, used for GIT application.

We assume that DATA_{GIT} covers a region with homogenous attenuation. This allows us to apply inversions using a single attenuation model (as in Eq(1)). We also set the reference hypocentral distance $R_0=10$ km due to lack of data at shorter distance bins. The impact of this choice is usually interpreted as shifting the source spectra to a distance R_0 . Then, this shifting is generally counterbalanced by rescaling them with R_0 (e.g., Castro et al., 1990; Oth et al., 2011; Bindi and Kotha, 2020).

The way of dealing with site constraints in GIT is not unique (Bindi and Kotha, 2020; Drouet et al., 2010; Nakano et al., 2015; Pacor et al., 2016; Shible et al., 2022a; Morasca et al., 2023), and it can be applied on one or several site terms. Figure 3.3 shows source spectra we obtained from GIT for a selection of earthquakes recorded on two different sites (GNU and MOMA), using two different site constraints referred hereafter as REF1 and REF2. According to REF1 hypothesis, the mean site response of all stations is fixed to 1, while according to REF2 hypothesis, the mean site response of a reference sites chosen by Morasca et al., (2023) is equal to 1. We observe that the impact on site terms is counterbalanced by impact on the source terms and consequently the attenuation functions are unaffected by the site constraint. Therefore, the combination of GIT-derived source and site terms are robust and unaffected by the site constraint choice. This is also in agreement with previous studies (Bindi and Kotha, 2020; Oth et al., 2011). Further discussion on the trade-off between the source and site terms in the nonparametric GIT are presented in Appendix A.4.

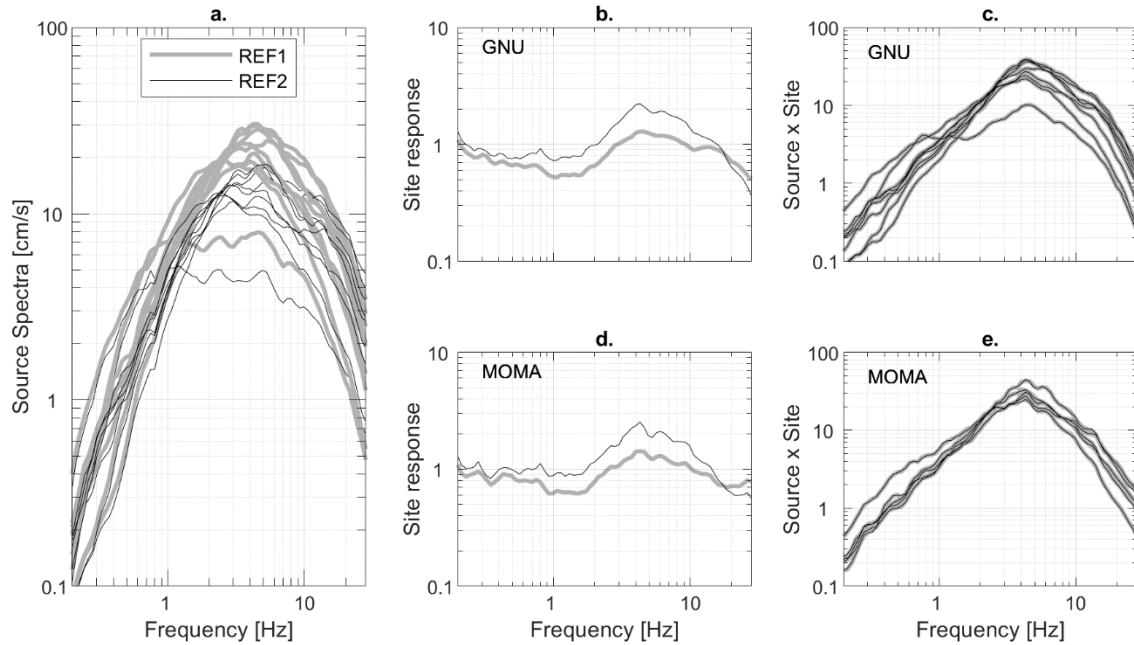


Figure 3.3: (a) Source terms of a selection of earthquakes recorded at 2 stations GNU and MOMA, (b,d) their respective site responses as obtained from GIT. (c,e) The source-site combination at each station. The gray and black colors correspond to inversions performed with REF1 and REF2 reference conditions, respectively.

3.2 Correction of Empirical Green's functions (EGFs)

First, an automated procedure is implemented to search for recordings to be used as input to EGF simulations. The automated procedure is defined to respect a set of criteria during the search. $DATA_{EGF}$ cannot be only defined from stations close to the case study due to lack of such recordings in the ESM database (see Appendix A.2). So, we searched for stations within a radius of 140 km from case study, while keeping a priority to data recorded on stations at shorter radii (i.e., near the study case). This is done by defining a sorted list of stations following their distance to case study.

Usually, the EGFs used in simulations are chosen among recordings of small magnitudes, which is an advantage of the approach, especially in low-to-moderate seismicity regions (Del Gaudio et al., 2018; Dujardin et al., 2020). However, we could retain a sufficient amount of recordings only after accepting events with magnitudes up to 5.0, since ESM database mainly focuses on magnitudes >4 . Also, the EGFs are preferred to be covering similar source-to-station distances as those of major interest for the seismic hazard analyses. So, we focus on recordings with epicentral distances less than 100 km.

The automated selection of EGFs is performed as follows:

- We ensure an acceptable sampling of source-to-site distances associated to EGFs by iteratively filling 10 equally-spaced bins of R_{EPI} (in \log_{10} scale), between 1 and 100 km,
- The priority to stations near the case study is respected by searching for station recordings in order from the sorted list,
- Filling distance bins by recordings from different stations is done until a minimal number of 10 recordings is found,
- We also attribute the recording if f_{min} and f_{max} cover the frequency range 0.3-25 Hz.

Further tests on the selection procedure are presented in Appendix A.3

Figure 3.4 shows the magnitude-distance distribution of data resulting from the automatic EGF search. We observe that most of the distance bins are well completed for different magnitudes, except for those within 1-3 km. We also remark that R_{EPI} bins between 35 and 100 km mostly contain from stations within 100 km from study case. Then, data with R_{EPI} between 15 and 35 km are mainly from stations at 100-120 km from the study case, while data at $R_{EPI} < 15$ km is mostly from stations farther than 120 km.

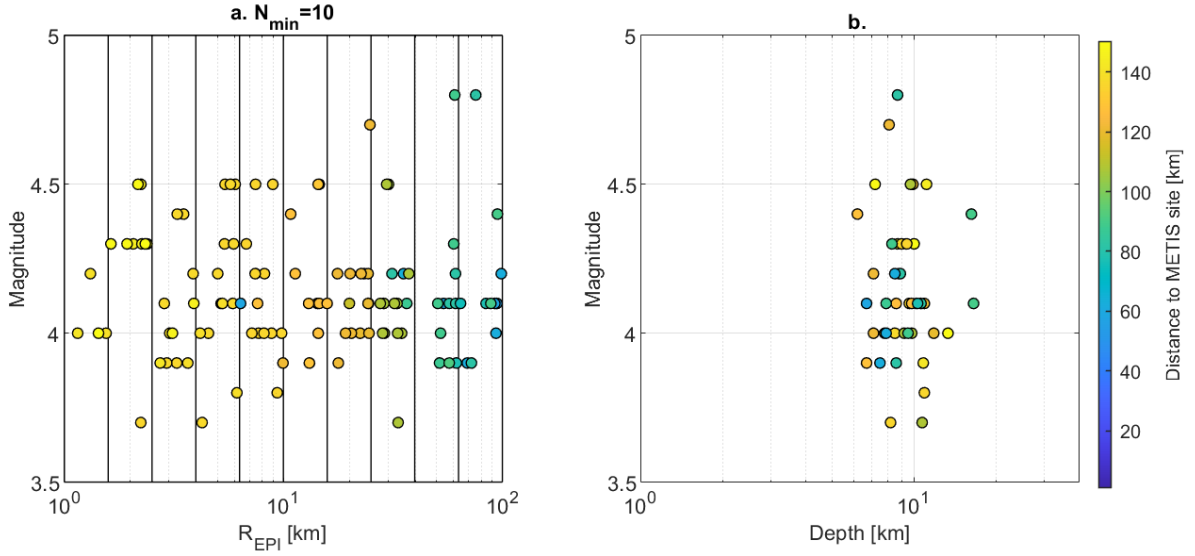


Figure 3.4:(a) The magnitude-distance distribution of selected recordings to construct the database for EGF simulations ($DATA_{EGF}$). (b) Magnitude-depth distribution of these recordings. The color scale represents the distance to the METIS site.

Afterwards, we apply the correction procedure to remove source and site effects as they result from GIT application. An example is shown in Figure 3.5, where we consider the recording of the earthquake referenced by “EMSC-20161201_0000064”, in the ESM database, of magnitude 3.9 at the station SNI of the IT network ($R_{EPI} = 60$ km). The correction function is defined as the combination of the corresponding source and site terms resulting from the GIT application. The correction is applied as follows:

- The original time history is first zero-padded to the next power of 2, before calculating the Fourier transform,
- Then, the correction function is interpolated, in the logarithmic scale, over the same frequency vector as the Fourier transform of the original time history,
- The correction functions do not cover the whole frequency band (they are simply the results of GIT), so we apply one-padding to complete the missing frequency points (Figure 3.5a). To avoid abrupt changes at the edges of the correction function, we apply smoothing at $f < 0.3$ Hz and $f > 28$ Hz using a $\frac{1}{2}$ cosine tapering in logarithmic scale,
- The phase of the transfer function is not estimated by the GIT. So, we assume a zero-phase of the correction function,
- We then correct the Fourier transform of the original earthquake signal with the defined correction function Figure 3.5b and c),
- In the end, we retrieve the corrected time history by applying the inverse Fourier transform (Figure 3.6).

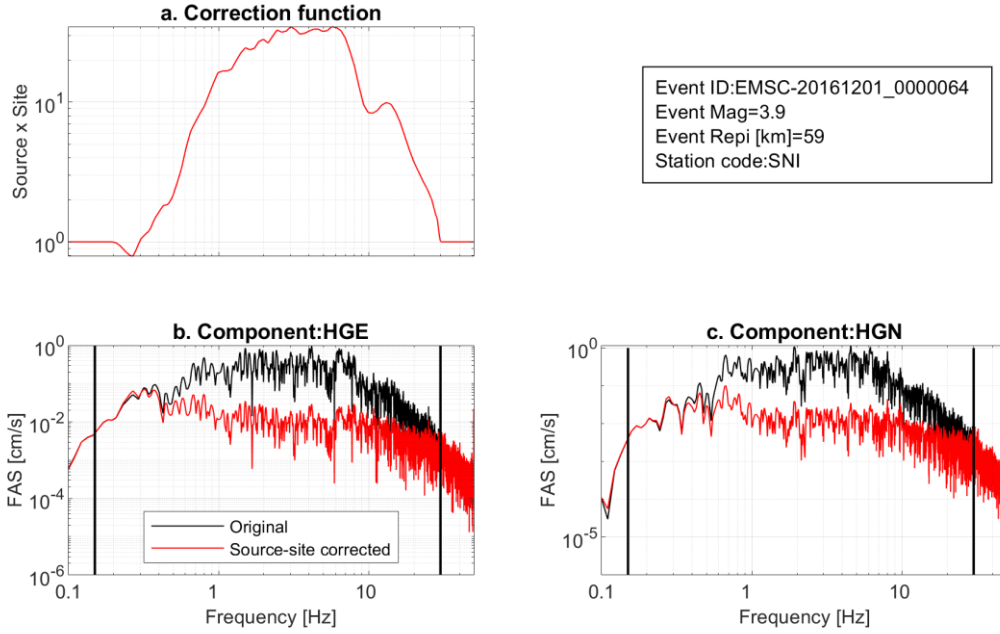


Figure 3.5: The correction of source and site effects applied on the 2 components of an example recording. (a) The correction function is used to remove source and site effects. (b) The FAS of the original signal and the corrected one.

We apply the source-site correction on both horizontal components of ground motion of all recordings in the DATA_{EGF} . We show in Figure 3.6 both E and N components of the same recording as in Figure 3.5. We can observe that after removing the source and site terms we still have a similar shape of the seismic signal because no phase modification was applied. As the main source of energy in the signal is removed, the amplitudes are much lower. Here, it is important to note that the signals are corrected for “averaged” source and site effects. Consequently, the corrected signal may still carry contributions from anisotropic effects of the source (e.g., directivity effects) and site (e.g., basin effects) effects.

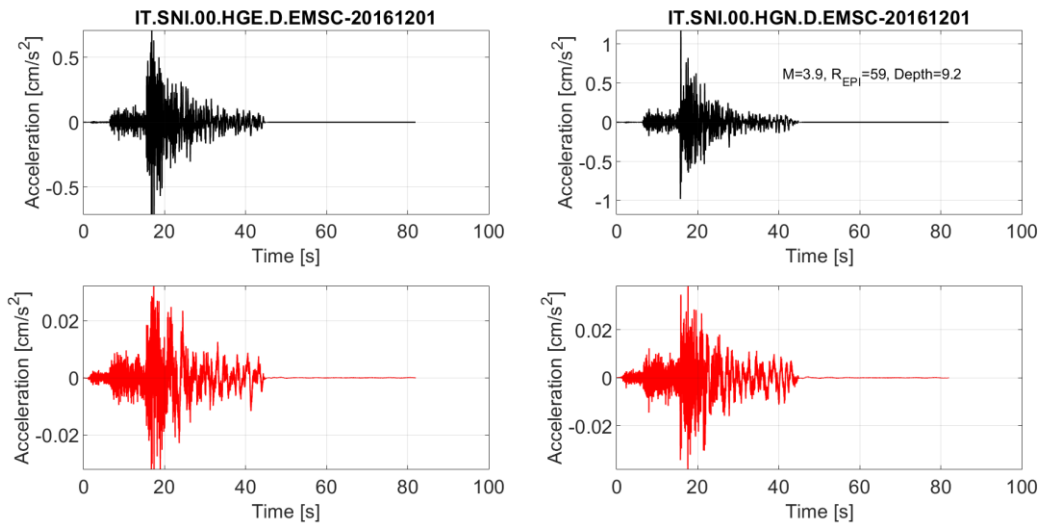


Figure 3.6: The original time history of a record is shown (in black) for both components E and N. The source-site corrected time history is also shown (in red).

We apply the correction procedure on all recordings of $DATA_{EGF}$. We perform a visual examination of each of the recordings to ensure that there are no anomalies, either before or after their correction from source-site effects. Then, we pass these corrected recordings through a verification analysis and visual inspection following their forms in the frequency domains. This post-correction verification consists of:

1. Visual checking of the Fourier spectra per distance bin, where distance bins are the same ones used to select the data initially (i.e., 10 distance bins in the logarithmic scale between 0.1 and 100 km),
2. Calculating the geometric mean of the two horizontal components denoted as “GM”,
3. Calculating the median GM and standard deviation of all recordings in \log_{10} ,
4. Flagging out as outliers all records that are outside the range of median GM ± 2.5 times the standard deviation within the frequency range 5-20 Hz,
5. Finally eliminating outliers from selection and repeating the process (steps 1, 2, 3, 4, and 5) until no outliers are found.

In the end, this process is stable when applied on $DATA_{EGF}$ and leads to identifying only very few records as outliers (6 out of 103). We show an example in Figure 3.7 for the combined horizontal components of records in 4 distance bins. After running the verification process, we identify outliers and flag it in red (e.g., the record of EMSC-20170427_0000119-FEMA) when it exceeds the limits of the stabilized median ± 2.5 standard deviation (shown in blue), at $f > 5$ Hz. We note that the analysis is limited to the usable frequency bandwidth (i.e., $f_{min}-f_{max}$), over which we had a reliable source-site correction function from GIT. We remark the increasing attenuation effects with increasing R_{EPI} .

Figure 3.8 shows the source-to-site paths and the magnitude-distance distribution of the EGF finally retained for ground motion simulations or the target events. We note that the source-to-station paths of the selected EGFs show a weak coverage of the region within 80 km around the study site. As already pointed out, this is because stations close to the METIS site have well-recorded far-distance events in the Apennines but lack of well-recorded local events. We also note that the some of the EGF are related to the same event recorded at multiple stations as well as to the same station that recorded multiple events. Overall the selected EGF corresponds to 39 events and 35 stations.

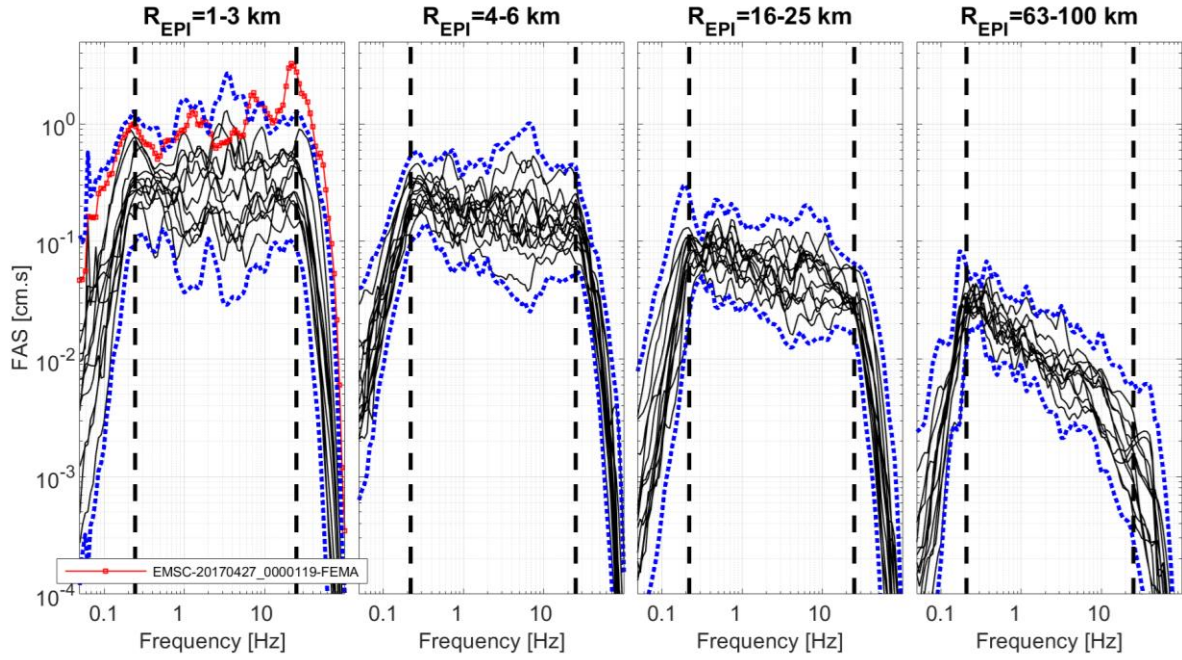


Figure 3.7: The FAS of combined horizontal components of the source-site corrected signals, passing through outlier-detection procedure before being input for EGF simulations. The identified outlier in the distance bin 1-3 km is highlighted in red. The blue dotted lines correspond to the median \pm standard deviation, the limits beyond which the signals are flagged outliers. The dashed black lines show the frequency range f_{min} - f_{max} in which source-site corrected recordings are considered reliable.

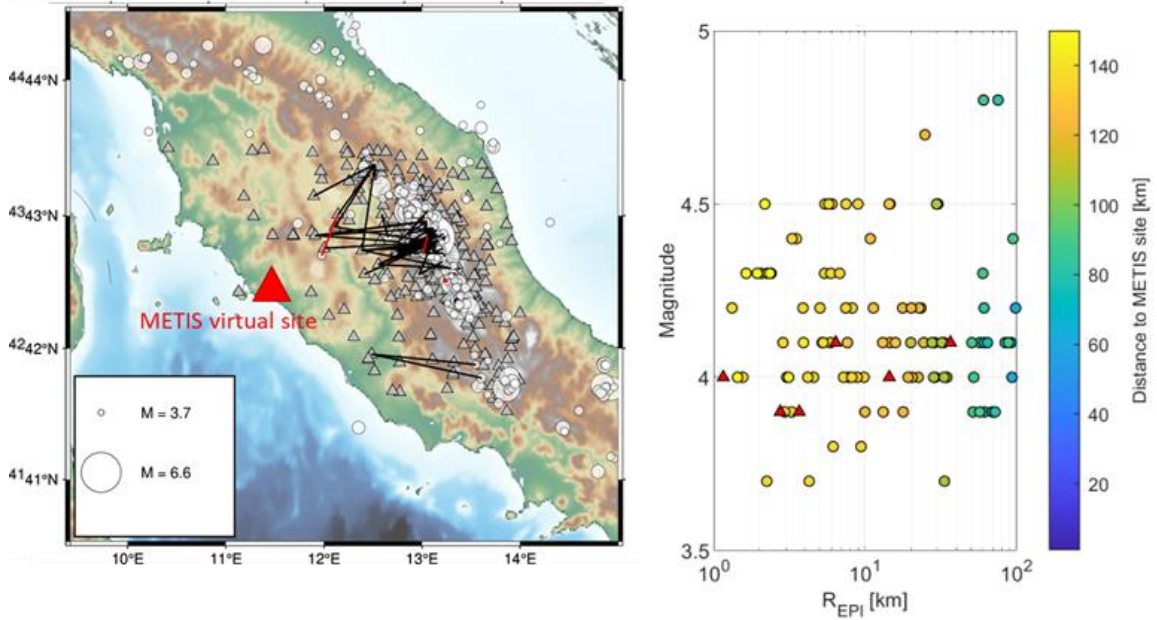


Figure 3.8: (left) Map showing the source-site ray paths of $DATA_{EGF}$ from the initial dataset. Red ray paths correspond to outliers identified and excluded from simulations. (right) Magnitude-distance distribution of $DATA_{EGF}$ with red triangles representing the identified outliers.

3.3 Source modeling for target magnitudes

Once the EGFs have been selected, they are convolved with a kinematic source model for the target magnitudes to simulate synthetic time histories for events of relevance for seismic hazard. Here we consider $M_w=5.0$, 5.5 and 6.0. In order to consider the uncertainties in the parameters describing the rupture geometry and kinematics of the target scenario events, the generation of the rupture models relies on random sampling. For each of the 39 selected EGF events, strike and dip angles of the target rupture are defined assuming uniform distributions within the following ranges: strike $[0 - 360^\circ]$ and dip $[40^\circ-90^\circ]$. The rupture is constrained to have an aspect ratio of 2 and centered at the hypocentral location of the EGF event. Then, 30 kinematic rupture models are simulated for each of the considered magnitudes and for each EGF event as follows:

- The stress drop ($\Delta\sigma$) values, which ultimately control (together with the magnitude) the rupture dimension and the corner frequency (f_c), are sampled (using Latin Hypercube Sampling) assuming a lognormal distribution. A median $\Delta\sigma=2$ MPa is selected being representative of the median stress drop obtained from the GIT applied to the selected dataset in his study. This value agrees with results from Morasca et al. (2023) for the bulk of events considered in their dataset (M_w below 5) in Central Italy. For larger magnitudes Morasca et al. (2023) suggest increasing values of stress drop with average values of about 10 MPa for $M_w\approx 6$. However, estimates of stress drop are generally characterized by large scatter and self-similar earthquake scaling is still subject of debate. A standard deviation ($\sigma_{\ln(\Delta\sigma)}$) of 0.5 is assumed in agreement with typical values inferred from empirical ground motion models (Cotton et al., 2013),
- The k^{-2} slip distributions are randomly generated as described in Section 2.2 (Figure 3.10, left),
- The position of the hypocenter is randomly located along the strike of the rupture and in its lower half (Figure 3.9, Figure 3.10, right),
- The rupture velocity is randomly sampled in the range $0.7 \cdot V_s$ and $0.85 \cdot V_s$ following a uniform distribution. $V_s = 3.2$ km/s is assumed for the Central Italy region (Morasca et al. 2023). Moreover, rupture velocities are randomly perturbed by 0.1% in order to mimic realistic rupture propagation (Figure 3.10, right).

Figure 3.10 shows examples of the randomly generated $M_w=5.5$ kinematic rupture scenarios in terms of rupture dimensions, slip distributions, and location of the hypocenter of the rupture. The distributions of some other relevant source parameters are shown in Figure 3.11. The distributions of hypocentral depths are similar for the three magnitudes because they are controlled by the hypocentral depths of the EGF events especially for the smaller rupture dimensions ($M_w=5.0$). The distributions of depth of the top of the rupture (Z_{tor}) are also quite similar, although for the number of scenarios with Z_{tor} smaller than 5 km increases with magnitude. As expected, the values of average slip, rupture length and rupture width clearly increase with the target magnitude.

Figure 3.12 shows the generated absolute source time functions for the Mw=5.5 scenarios providing a significant variability in the time and frequency domains despite the relatively small source dimension (and short source duration). The corresponding source spectra follow adequately the omega-squared model up to the requested maximum frequency (i.e., 20 Hz) according to the Hisada (2001) method. We note that the mean source spectrum of the 30 simulations is in good agreement with the Brune's model for a mean stress drop value of the input distribution (2.3 MPa).

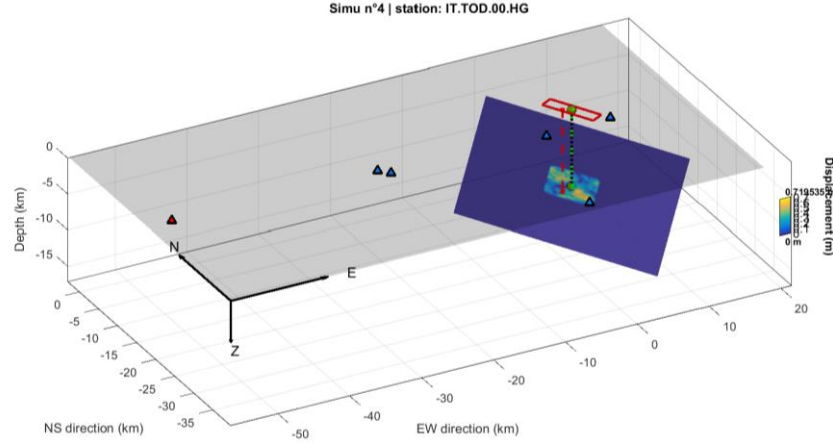


Figure 3.9: Example of 3D view of simulated rupture geometry for a Mw=5.5 event. The final displacement on the rupture is shown for a single simulation. The red rectangle represents the surface projection of the rupture and the vertical dashed red line points the rupture nucleation. The brown circles represent the hypocenter and the epicenter of the EGF event (EMSC-20161031_0000053). Triangles show the position of the considered stations. The blue rectangle represents the fault plane hosting the randomly generated rupture models.

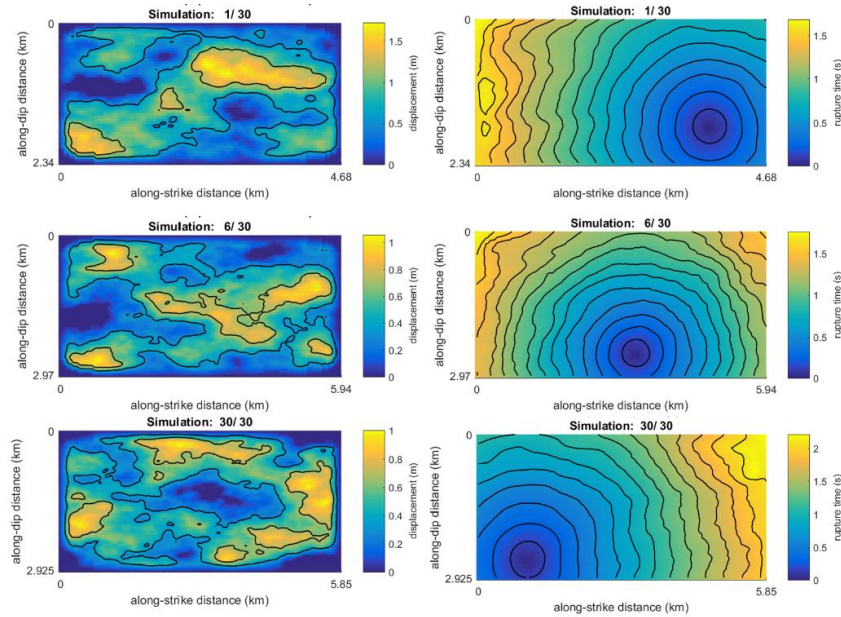


Figure 3.10: Example realizations of slip distributions (left) generated from the k^{-2} source model and hypocenter locations and related rupture times (right) for the Mw=5.5 scenarios. Note the different dimensions of the ruptures. The hypocenter is assumed to be in the lower half of the rupture (Mai et al., 2005).

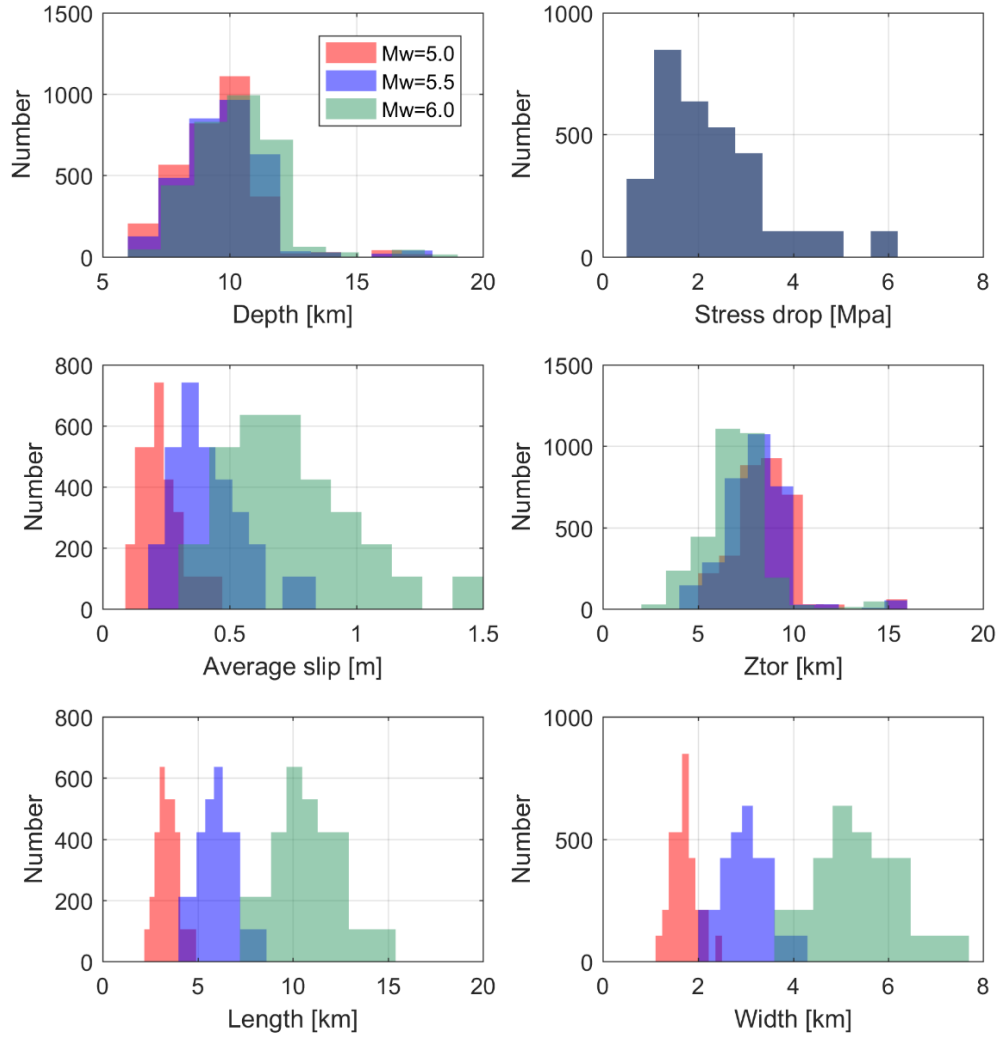


Figure 3.11: Representative rupture parameters obtained for the 30 rupture models for Mw 5.0, 5.5 and 6.0 earthquakes.

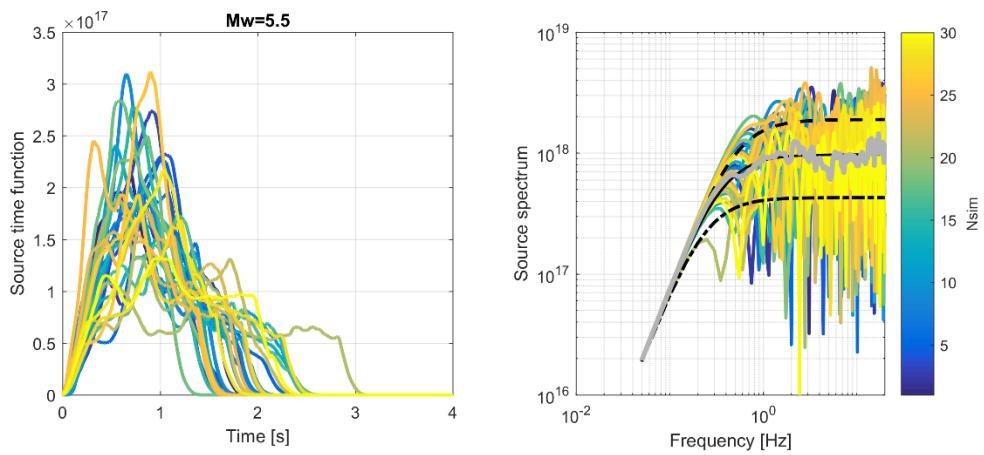


Figure 3.12: Absolute source time functions generated by the k^{-2} method (left) and corresponding source spectra (right) for the Mw=5.5 scenarios (30 simulation, Nsim). The Brune source spectra for the minimum (0.67 MPa), mean (2.3 MPa) and maximum (6.2 MPa) stress drop values are also reported (in black) for comparison as well as the mean of the simulated source spectra (in gray).

3.4 Results for selected target magnitudes

3.4.1 Comparison with empirical GMM

We used 97 EGFs (once outliers are excluded, as discussed previously) and 30 rupture models for each target magnitude resulting in slightly less than 3000 ground motions for each horizontal component covering distances up to about 100 km. Starting from the whole set of simulated time histories, we computed response spectra (geometric mean of horizontal components) as well as other ground-motion intensity measures of interest (e.g., PGA, PGV, duration). The results of the simulated ground motions are first presented in terms of spectral acceleration values at selected spectral periods for the Mw=5 and Mw=6 scenarios.

In Figure 3.13, the simulated horizontal spectral accelerations at three spectral periods ($T = 0.01$ s, 0.2 s and 2 s) are represented as a function of distance and are compared with the empirical GMM for Italy (ITA18) by Lanzano et al. (2019) for a $V_{s30} = 800$ m/s. Since the site response has been removed in the simulations, the ITA18 model modified by Lanzano et al. (2022) for generic reference rock is also shown. Note that simulations were band-pass filtered between 0.3 Hz and 20 Hz which represent approximately the usable frequency band of the EGF and maximum target frequency of the simulations. We observe that the simulated values are in good agreement with the ITA18 GMM, the mean values of the simulations being in general within one standard deviation of the GMM for both magnitudes. The distance scaling of the simulated values is also very consistent with that of ITA18 confirming that the use of the selected EGF to account for the path effect is appropriate. Of particular interest for the present study is the fact that mean simulated values is in better agreement with the ITA18 GMM corrected for the site response as proposed by Lanzano et al. (2022) supporting the procedure adopted to remove the site terms from the EGFs.

Interestingly, the standard deviation of the simulated values is also in broad agreement with that of the ITA18 at least up to about 20 km. At longer distance, the standard deviation of simulations decreases likely because the variability of the rupture models mostly affects the simulated ground motions at short distances whereas at longer distances, the variability is mostly controlled by differences in the attenuation along the path which in our case is related to a limited region. Similarly, the lower standard deviation of the simulated spectral accelerations at long periods ($T = 2$ s) maybe related to the similarity of the EGF at long periods sampling a much smaller regions with respect to the one considered in the ITA18 GMM.

A further comparison of the distance scaling of the simulated spectral accelerations is presented in Figure 3.14. In this case the simulations are compared with the median predictions from the GMM adopted in the latest European Seismic Hazard Model (ESHM20) as described by Weatherill et al. (2020). The median ground motion model is represented by nine logic tree branches accounting for epistemic uncertainties in the attenuation and source terms. Here we consider the predictions for the attenuation cluster corresponding to the location of the METIS site (cluster 3 in Weatherill et al., 2020) corresponding to a fast attenuation compared to the default model. The comparison shows that the simulated spectral accelerations at $T=0.01$ s and $T=0.2$ s are generally lower than the predictions by the ESHM20 GMM whereas they are more in agreement for $T=2$ s. The distance scaling at short spectral

periods seems stronger for the simulated values than for the GMM which suggest a different attenuation in the target region compared to that of the ESHM20 GMM (although a regional attenuation term correction is considered). Furthermore, the ESHM20 GMM is evaluated for generic a $V_{s30}=1100$ m/s which does not corresponds to the reference bedrock conditions of the simulations.

In Figure 3.15, the comparison with the ITA18 model is presented in terms of response spectra at a distance of 20 km. The simulated response spectra at distances between 15 and 25 km as well as their mean spectrum are compared to the response spectra predicted by the ITA18 for $V_{s30}=800$ m/s and modified for reference site conditions. The response spectra of the simulated time-histories for both magnitudes are in general good agreement with the ones predicted by the ITA18 GMM and in particular with the model for reference sites. We observe however that the peaks of the mean simulated spectra are slightly shifted toward higher frequencies compared to the ITA18 models. This may be due to the characteristics of the EGFs employed to simulate the ground motions at such distances. In order to illustrate this, Figure 3.16 shows, for the case of $M_w=5$ at 20 km, the mean of the simulated spectra (in spectral response and Fourier domains) for each adopted EGF (denoted by an event and a station). We note that the simulated spectra depend significantly on the considered EGF both in amplitude and in spectral shape, especially for frequencies higher than about 2 Hz. Some of the EGFs produce response spectra with peaks at frequencies higher than 10 Hz whereas others lead to spectral shapes more in agreement with the ITA18 model. The variability of the EGF Fourier spectra (lower-left plot of Figure 3.16) resembles that of the simulated spectra with e.g., blueish colors spectra having lower amplitudes than reddish colors ones, and points out that the wave propagation effects can be highly variable even in such a small region (Figure 3.16 lower-right). We note however that trade-off exists between source and propagation effects and that phenomena such as rupture directivity (highlighted by Colavitti et al., 2022 for small magnitudes in Central Italy) that are not accounted by the isotropic source correction we adopted in the GIT may also contribute to the observed variability of the EGF spectra.

In order to further validate the simulated ground motions we compare in Figure 3.17 the significant duration (D5-95) of the simulated time histories for the $M_w=5$ and $M_w=6$ scenarios with the estimates from the Pan-European empirical model by Sandikkaya and Akkar (2017). The comparison as a function of distance shows a good agreement between simulated and predicted values by the empirical model. Some relevant differences are noted at the shortest and longest distances where the duration of the simulated time histories are respectively shorter and longer than those predicted by the model. At short distance, the duration is controlled by the source duration and this result may suggest that the simulated source durations for the target events are too short. The short duration of a specific EGF used at short distance may also contribute to the observed differences.

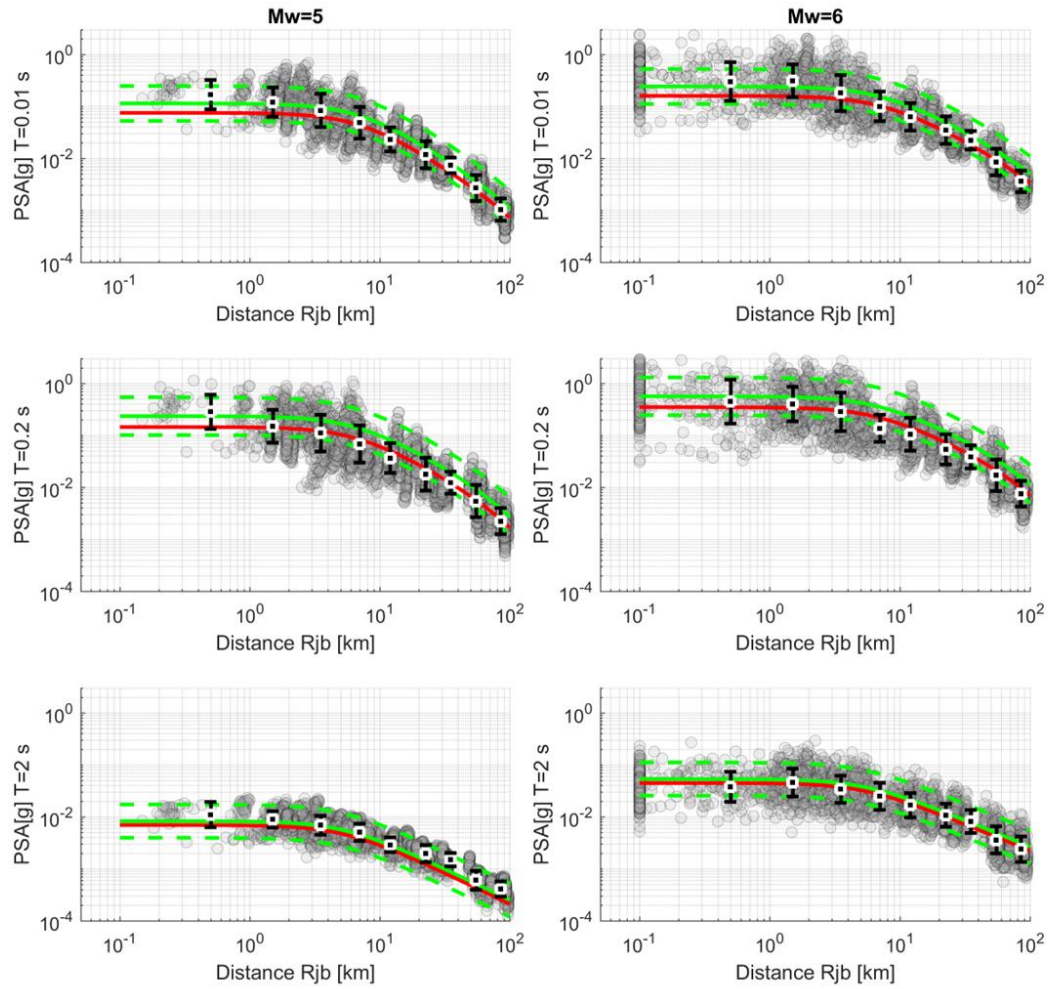


Figure 3.13 : Simulated spectral acceleration (PSA) for $M_w=5$ (left) and $M=6$ (right) as a function of the Joyner-Boore distance (Rjb) for three spectral periods ($T=0.01$ s, 0.2 s and 2 s). The gray circles represent the geometric mean of the horizontal components, and the vertical black bars represent the mean and standard deviation of simulated values over distance bins. Stations within the surface projection of the rupture are plotted at $R_{jb} = 0.1$ km. The GMM for Italy (ITA18) by Lanzano et al. (2019) is plotted in light green (median ± 1 standard deviation) considering a $V_{s30}=800$ m/s and normal fault mechanism. The median ITA18 adjusted for reference rock conditions according to Lanzano et al. (2022) is shown in red.

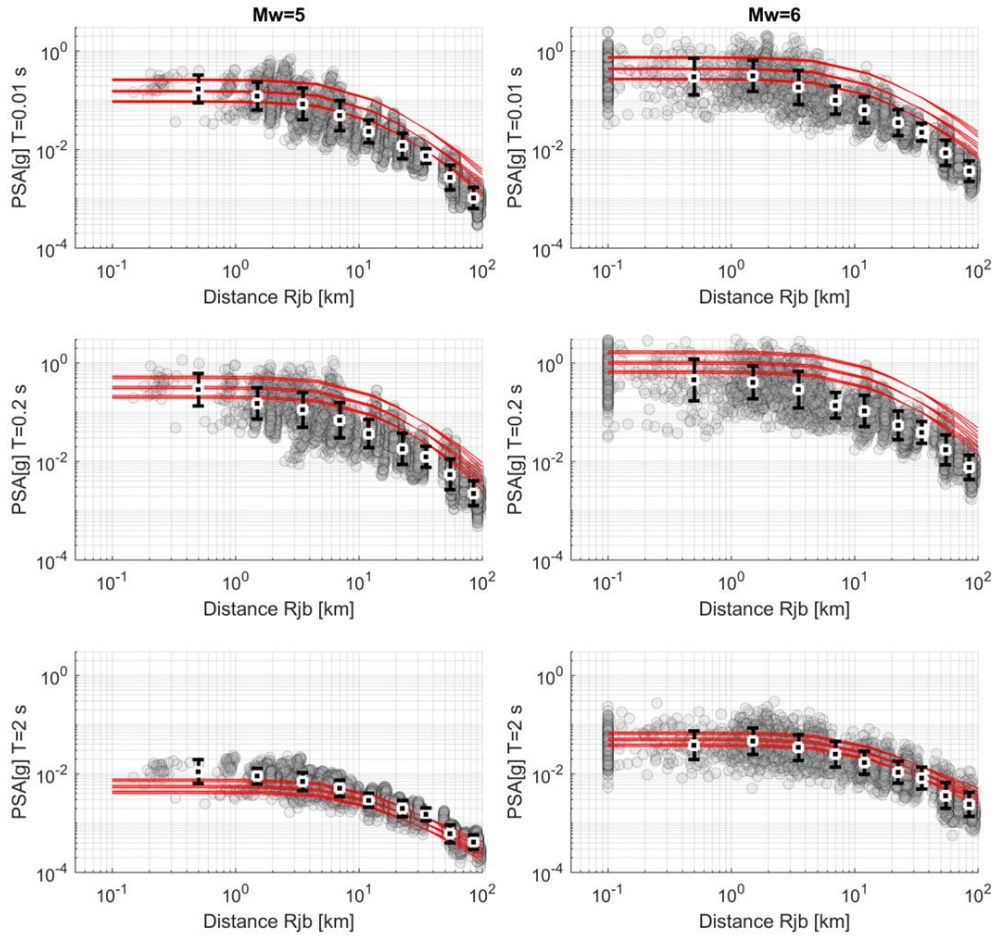


Figure 3.14 : Simulated spectral acceleration (PSA) for $M_w=5$ (left) and $M_w=6$ (right) as a function of the Joyner-Boore distance (R_{jb}) for three spectral periods ($T=0.01$ s, 0.2 s and 2 s). The gray circles represent the geometric mean of the horizontal components, and the vertical black bars represent the mean and standard deviation of simulated values over distance bins. Stations within the surface projection of the rupture are plotted at $R_{jb} = 0.1$ km. The European GMM adopted by Weatherill et al. (2020) is plotted in red for a $V_{s30}=1100$ m/s and considering the 9 branches of the logic tree proposed to capture uncertainties in median ground motion for attenuation cluster 3.

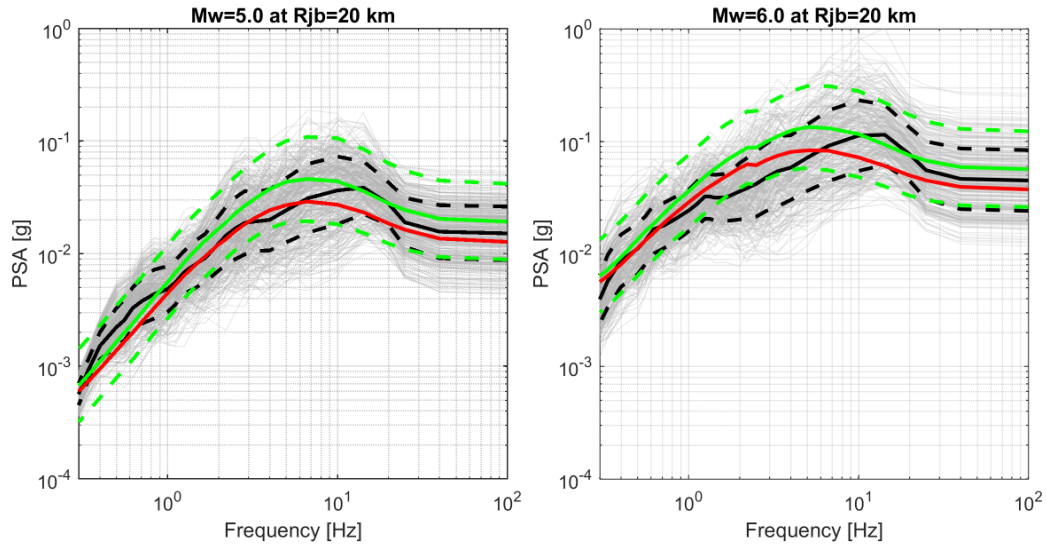


Figure 3.15 : Simulated response spectra (in gray) for the Mw=5 (left) and Mw=6 (right) scenarios at 20 km (stations at distances between 15 km to 25 km are used) for the geometric mean of horizontal components. The mean \pm 1 standard deviation of the simulated spectra is shown in black. The GMM for Italy (ITA18) by Lanzano et al. (2019) is plotted in green (median \pm 1 standard deviation) considering a $V_{s30} = 800$ m/s and normal fault mechanism. The median ITA18 adjusted for reference rock conditions according to Lanzano et al. (2022) is shown in red.

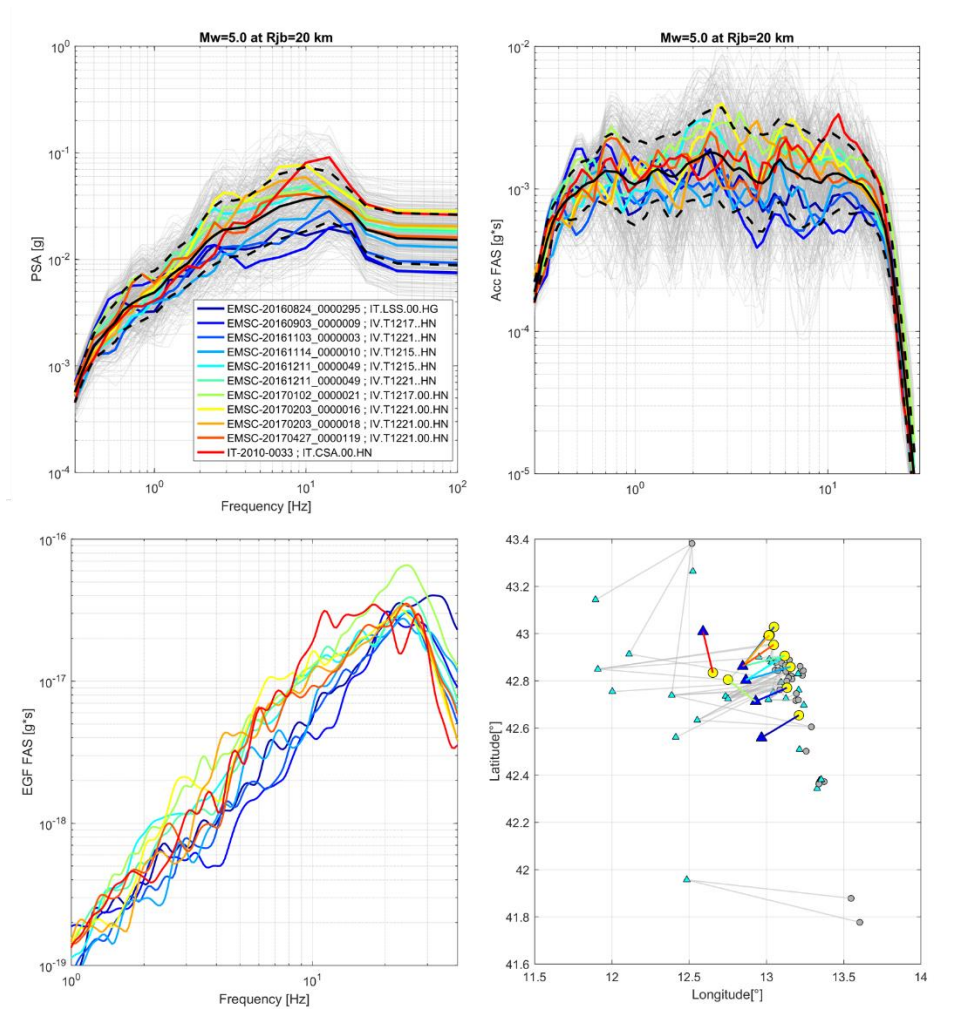


Figure 3.16 : (upper-left) simulated response spectra (in gray) for the Mw=5 scenarios at 20 km (stations at distances between 15 km to 25 km are used) for the geometric mean of horizontal components. The mean ± 1 standard deviation of the simulated spectra is shown in black. The mean spectrum obtained for each EGF is shown in color. (upper-right) the same as in upper-left but in terms of Fourier amplitude spectra (FAS). (lower-left) Fourier amplitude spectra of the EGF (after deconvolution for source and site terms). (lower-right) Map of the adopted EGF paths for Mw=5 and 20 km (in colors) compared overall set of EGF paths (in gray). Circles and triangles represent epicenters and stations respectively.

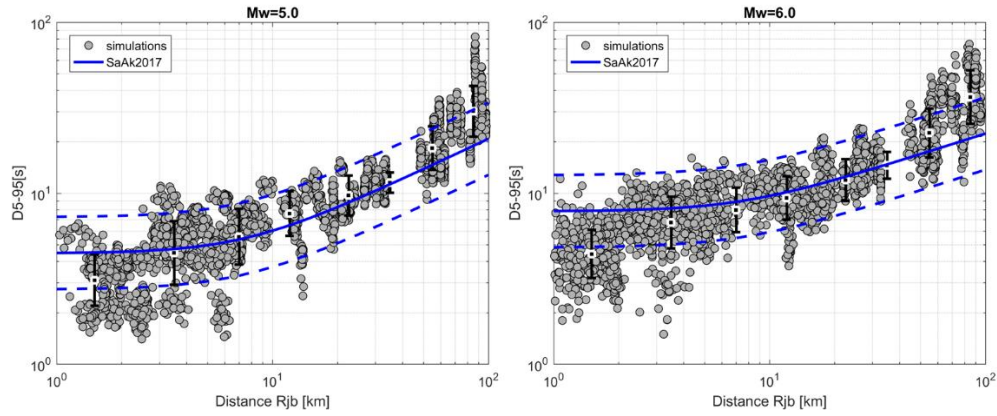


Figure 3.17 : Comparison between simulated horizontal significant durations (D5-95: time elapsed between 5% and 95% of the total Arias Intensity) as a function of distance for Mw=5 (left) and Mw=6 (right) scenarios and the predictions by the Sandikkaya and Akkar (2017) empirical model for the Pan-European region (in blue, median \pm 1 standard deviation) for Vs30=800 m/s and normal-fault mechanism.

3.4.2 Comparison with observations from similar events

A second comparison is presented in this section with respect to spectral accelerations observed for events occurred in Central Italy with magnitudes close to those of the simulated target scenarios. To this aim, we selected from the ITACA database (Russo et al., 2022) the available recordings at stations located between 41.5° and 43.5° latitude and 11.0° and 13.5° longitude from magnitudes between 4.8 to 6.2 at distances up to 100 km from the stations. In order to have a meaningful comparison, we considered only stations identified as reference rock sites in ITACA according to the procedure by Lanzano et al. (2020). The comparison between simulated and observed spectral accelerations as a function of distance is presented in Figure 3.18 for Mw=5.0 and Mw=6.0. For each magnitude, only observations from events within 0.1 magnitude units from the target are considered. Because our objective is to simulate regional ground motions and not to model a specific event, we mix observations from several events in this comparison. The mean values and the range of simulated values are in good agreement with the observations for both magnitudes and for the considered spectral periods. The simulations show a slight tendency to underestimate the observations at $T=0.2$ s and for Mw=5, short-period spectral ordinates are also lower than observed ones at large distances (70 km). Most of the data are at distances larger than 10 km and we cannot comment much on the comparison at shorter distances; however the few observations at close distances are captured by the range of simulated values. It is also important to remark that the set of observations does not contain necessarily the same stations considered in the simulations.

Figure 3.19 shows a similar comparison in terms of response spectra for three magnitudes (Mw=5.0, 5.5 and 6.0) at 20 km. Despite the fact that the observed data are limited in number, especially for Mw=6, and that the variability is quite large also due to the selected range of distances (15 km to 25 km), we note a general good agreement between the mean simulated and observed spectra, particularly for Mw=5.5 and 6.0.

Overall these comparisons support both the appropriateness of the Green's function deconvolution approach as well as the source modelling for target events in the region.

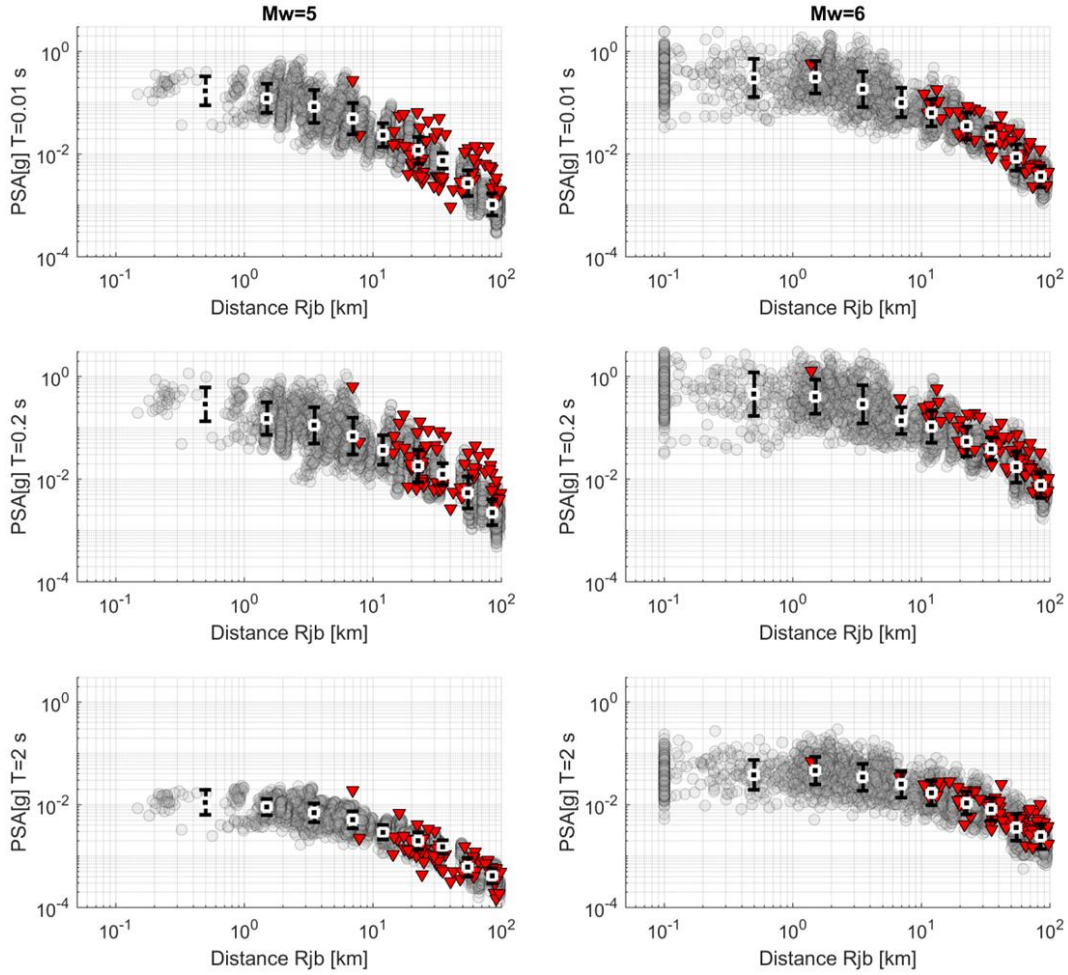


Figure 3.18 : Comparison between simulated (gray circles) and observed (red triangles) spectral acceleration (PSA) for $M_w=5$ (left) and $M_w=6$ (right) as a function of the Joyner-Boore distance (R_{jb}) for three spectral periods ($T=0.01$ s, 0.2 s and 2 s). The vertical black bars represent the mean and standard deviation of simulated values over distance bins. Stations within the surface projection of the rupture are plotted at $R_{jb} = 0.1$ km. The observed data are for ± 0.1 magnitude units with respect to the target magnitudes.

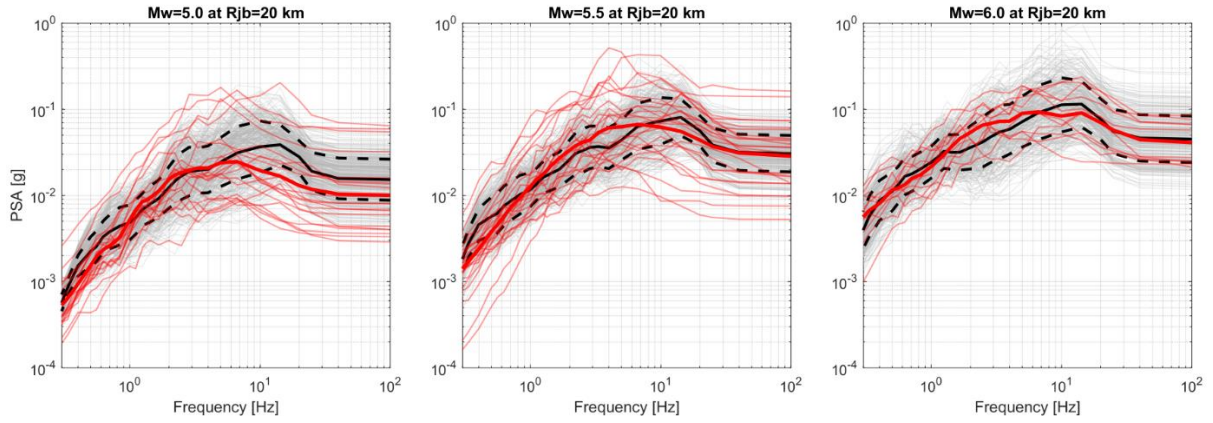


Figure 3.19 : Comparison between simulated (in gray) and observed (in red) response spectra for Mw=5 (left), Mw=5.5 (center) and Mw=6 (right) scenarios at 20 km (spectra distances between 15 km to 25 km are used and, for observations only, magnitudes within ± 0.1 units from the target) for the geometric mean of horizontal components. The median ± 1 standard deviation of the simulated spectra is shown in black. The thick red curve represents the mean of the observed spectra. See the text for further details on the selected data.

3.4.3 Simulated time histories

One of the advantages of the proposed simulation approach is that it allows generating synthetic time histories based on empirical path terms including complexities in the wave propagation that would be difficult to model numerically. Moreover, the time histories are simulated at reference rock (i.e., without site response) and they may be used as realistic region-specific input motions for dynamic soils response analysis.

Figure 3.20 shows an example of simulated acceleration and velocity horizontal time histories for Mw=6.0 at several stations with increasing distances. We can note that the durations of the simulated time histories realistically increase with increasing distance as well as the time difference between P and S-waves arrivals. At the largest distances we also observe the presence of surface waves after the S-waves phase on the velocity signal.

Figure 3.21 shows an example of the impact of the variation of the source stress drop on the simulated time histories for a Mw=6 at a station above the fault (Rjb=0 km). The acceleration and velocity time histories as well as the corresponding response spectra are presented for three stress drop values chosen to be close to the average, the minimum and the maximum values of the distribution of the stress drop used in the simulations (see section 3.3). We can observe that as expected the PGA and PGV values as well as the spectral ordinates increase with increasing stress drop because the source radiates more high-frequency energy. Moreover, we observe that the duration is inversely proportional to the stress drop because it controls in the present approach the dimensions of the rupture. We remark that rupture velocity and rupture nucleation point are also randomly varied in the set of 30 simulations which further contributes to the differences in the presented time histories.

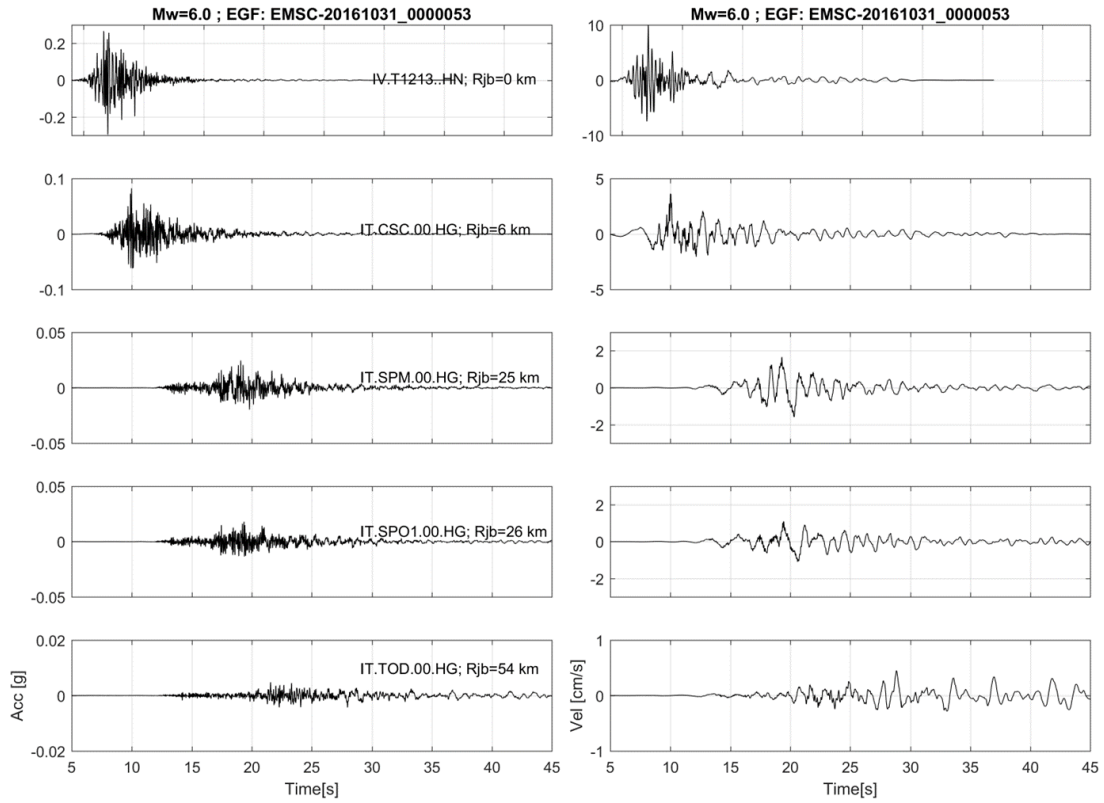


Figure 3.20: Example of simulated acceleration (left) and velocity (right) time-histories (east-west component) for a Mw=6.0 scenario at increasing distances (station code and Rjb are indicated in the figure). The original EGF event is EMSC-20161031_0000053.

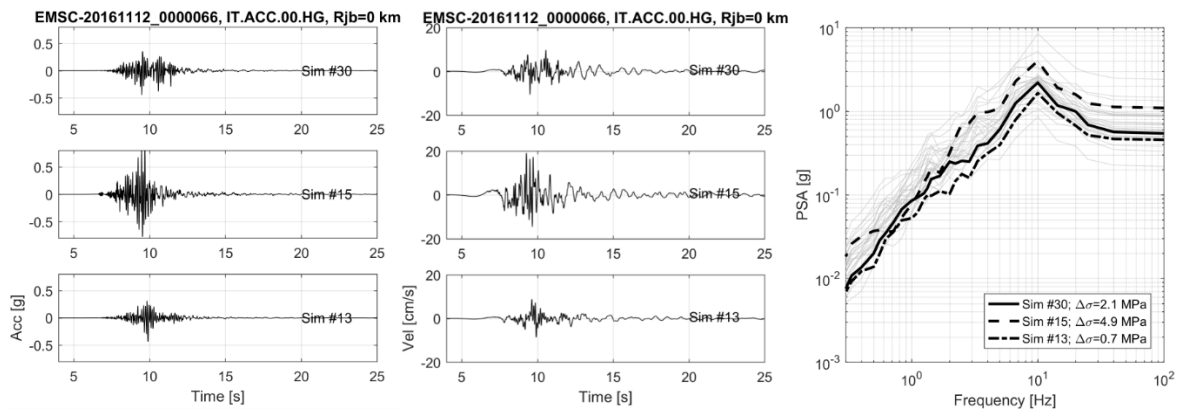


Figure 3.21 : Example of simulated acceleration (left) and velocity (center) time histories (east-west component) for a Mw=6.0 scenario above the fault (Rjb=0 km) considering station IT.ACC and EGF event EMSC-20161112_0000066. The selected simulations are for three values of stress drop (#30=2.1 MPa, #15=4.9 MPa and #13=0.7 MPa). The corresponding response spectra are presented in the right-most plot and compared with ensemble of simulations using this EGF for Mw=6 and Rjb=0 km.

4. Discussion and conclusions

As shown in the previous sections, the proposed method to simulate reference bedrock time histories is rather promising. The main advantages and limitations of the proposed approach are discussed hereafter.

The proposed method allows the efficient generation of 3-component time histories for reference bedrock conditions containing empirical region-specific path effects. Provided that the usable frequency band of the EGF is large enough, the simulated data cover the wide frequency range of interest for engineering applications (about 0.2 to 20 Hz). Thanks to the use of the EGF, the method accounts for 3D wave propagation without the need for detailed theoretical modeling of the crust and using modest computational resources compared to 3D physics-based modeling. As documented in the previous sections, the resulting time series are statistically credible both in time (i.e. shape, amplitude, duration) and in frequency (i.e. FAS amplitude, response spectra) for the various magnitude-distance rupture scenarios considered. Even if some progresses are still to be done regarding the modeling of the ground motion variability, the application could be easily expanded to a much larger EGF dataset including small magnitude records at short distances.

In this application, the EGF recordings were retrieved from events having magnitude between 3.5 and 5.0. There is no theoretical limit on the magnitude to adopt when selecting the EGF, the only limitation being the appropriate signal-to-noise ratio of the small-event records over a broadband frequency range. As such, compared to the classic EGF approach of Irikura, the present methodology can be applied to much-lower-magnitude events (M_{2+}). In this way, the wealth of small-magnitude data that may be available in low-seismicity regions may be used to simulate large-magnitude events, in particular at short distances which a topic is of major concern for the seismic hazard assessment. This calls for the reinforcement of seismological instrumentation of the critical facilities at the site scale and site vicinity in order to expand the database to low magnitude recording at close distance of the target sites.

The use of the nonparametric GIT to estimate the source and site terms makes the path term (the deconvolved EGF) neither sensitive to the reference site(s) used in the inversion nor to the metadata (magnitude, V_{S30}) of the collected recordings. This has the advantage of taking the best of the two techniques (GIT and EGF modeling) without suffering of the main limitations. This is also of great interest given the difficulty to find relevant reference-site outcrops to deploy the instrumentations in many areas (e.g. Po plain, Parisian basin), or to make use of the recordings near industrial area which are polluted by the anthropic activities. Thanks to the approach, even soft soil sediment recordings close enough to the target site are of interest to evaluate the reference rock ground motion at the target site, provided that these recordings can be coupled in the GIT to other measurements to sort out the source, path and site terms. The weak sensitivity of the deconvolved EGF to the metadata is also a great advantage when combined with the EGF simulation technique as it allows taking benefit of the small magnitude events which are often poorly characterized in terms of moment magnitude. One should nonetheless recognize that the lack of constrained on the hypocentral depth, in particular

for the small magnitude events, remains an issue when using the EGF. Thanks to the densification of the seismological network, this limitation may vanish in the forthcoming years.

In the framework of the METIS project, the approach has been set up to generate a large set of 3-component time histories covering the necessary magnitude-distance range (e.g., based on hazard disaggregation for a target site) with the objective to select hazard-consistent time histories for subsequent soil response analysis or structural response evaluation. However, the deconvolved EGF coupled to the kinematic source modeling methodology could also be used either to develop region-specific reference GMMs in the high seismicity regions or to adjust existing GMMs for the target region in the low to moderate seismicity regions to partially remove the ergodic assumption in classic PSHA. The comparisons of the response spectra predicted by the purely empirical models with the ones obtained by post-processing the database of simulated ground motions can also shed some lights to inform the seismic hazard team when characterizing the GMM to represent the Center, Body and Range of the technically defensible interpretations. Indeed, the lack of reference rock recordings is a strong limitation to validate the existing GMPE models. These results offer a complementary resource to select existing models and may also be used to develop the weighting scheme.

Some of the challenges that face this approach are to be discussed. The strongest limitation is related to the fact that the proposed methodology cannot be applied if no data is available in the target region, contrary to purely numerical simulation approaches. Another strong limitation is the lack of data to validate the overall results. Indeed, we must acknowledge that, regarding reference rock ground motion, there are very little data preventing to perform statistical analyses. One strategy could consist of combining the reference rock ground motion with the site effects (GIT, 1D modeling) to compare with the natural recordings. Even if one must concede some assumptions, this could warrant the overall consistency of the estimates.

In this study, we focus to develop practical and operational products to be used for the METIS project. Further tests are nonetheless highly recommended to assess the impact of all the used parameters, inputs, and assumptions in this approach. For example, the spectral decomposition of ground motion relies on constraints, one of which is the choice of the reference distance. Though it is preferably chosen in the application within the shortest distances bins available, its lower limit is controlled by the presence of data. A quantification of the impact of such a choice in the overall procedure and results should be further assessed.

Further improvements in the methodology may consider the phase modification in the source-site deconvolution. At present, phase is not considered in the deconvolution and this will undoubtedly bias to some extent the duration of the simulated time histories, particularly for soft-soil sites. Another important improvement may concern the source model which is still quite simplified in the current approach. Pseudo-dynamic rupture models and fractal approaches may provide more realistic source radiation, a better control of the directivity, a better correlation between the slip, rupture velocity and rise time. On one hand, better accounting for the directivity may lead to increase the ground motion variability at short-to-intermediate distance. On the other hand, a better representation of the kinematic source may help to discard non-realistic rupture realization, contributing to better control the variability.

5. References

- Ameri, G., F. Hollender, V. Perron, and C. Martin (2017). Site-specific partially nonergodic PSHA for a hard-rock critical site in southern France: Adjustment of ground motion prediction equations and sensitivity analysis, *Bull. Earthq. Eng.* doi: 10.1007/s10518-017-0118-6.
- Ameri, G., Martin, C., Oth, A., 2020. Ground-Motion Attenuation, Stress Drop, and Directivity of Induced Events in the Groningen Gas Field by Spectral Inversion of Borehole Records. *Bulletin of the Seismological Society of America* 110, 2077–2094. <https://doi.org/10.1785/0120200149>
- Andrews, D.J., 1986. Objective Determination of Source Parameters and Similarity of Earthquakes of Different Size, in: Das, S., Boatwright, J., Scholz, C.H. (Eds.), *Earthquake Source Mechanics*. American Geophysical Union, pp. 259–267. <https://doi.org/10.1029/GM037p0259>
- Bard, P.-Y., Bora, S.S., Hollender, F., Laurendeau, A., Traversa, P., 2020. Are the Standard V S - Kappa Host-to-Target Adjustments the Only Way to Get Consistent Hard-Rock Ground Motion Prediction? *Pure Appl. Geophys.* 177, 2049–2068. <https://doi.org/10.1007/s00024-019-02173-9>
- Bindi, D., Kotha, S.R., 2020. Spectral decomposition of the Engineering Strong Motion (ESM) flat file: regional attenuation, source scaling and Arias stress drop. *Bull Earthquake Eng* 18, 2581–2606. <https://doi.org/10.1007/s10518-020-00796-1>
- Bindi, D., Pacor, F., Luzi, L., Massa, M., Ameri, G., 2009. The Mw 6.3, 2009 L'Aquila earthquake: source, path and site effects from spectral analysis of strong motion data. *Geophys J Int* 179, 1573–1579. <https://doi.org/10.1111/j.1365-246X.2009.04392.x>
- Biro, Y., Renault, P., 2012. Importance and Impact of Host-to-Target Conversions for Ground Motion Prediction Equations in PSHA. *Proc. of the 15th World Conference on Earthquake Engineering*. 10.
- Brune, J. N. (1970). Tectonic stress and the spectra of seismic shear waves from earthquakes. *Journal of Geophysical Research*, 75(26), 4997–5009.
- Cadet, H., Bard, P.-Y., Rodriguez-Marek, A., 2012. Site effect assessment using KiK-net data: Part 1. A simple correction procedure for surface/downhole spectral ratios. *Bull Earthquake Eng* 10, 421–448. <https://doi.org/10.1007/s10518-011-9283-1>
- Castro, R.R., Anderson, J.G., Singh, S.K., 1990. Site response, attenuation and source spectra of S waves along the Guerrero, Mexico, subduction zone. *Bulletin of the Seismological Society of America* 80, 1481–1503.
- Colavitti, L., Lanzano, G., Sgobba, S., Pacor, F., & Gallovič, F. (2022). Empirical evidence of frequency-dependent directivity effects from small-to-moderate normal fault earthquakes in Central Italy. *Journal of Geophysical Research: Solid Earth*, 127, e2021JB023498. <https://doi.org/10.1029/2021JB023498>
- Cotton, F., Scherbaum, F., Bommer, J.J., Bungum, H., 2006. Criteria for Selecting and Adjusting Ground-Motion Models for Specific Target Regions: Application to Central Europe and Rock Sites. *J Seismol* 10, 137. <https://doi.org/10.1007/s10950-005-9006-7>
- Del Gaudio, S., Hok, S., Festa, G., Causse, M., Lancieri, M., 2018. Near-Fault Broadband Ground Motion Simulations Using Empirical Green's Functions: Application to the Upper Rhine Graben (France–Germany) Case Study, in: Dalguer, L.A., Fukushima, Y., Irikura, K., Wu, C. (Eds.), *Best Practices in Physics-Based Fault Rupture Models for Seismic Hazard Assessment of Nuclear Installations*, Pageoph Topical Volumes. Springer International Publishing, Cham, pp. 155–177. https://doi.org/10.1007/978-3-319-72709-7_10
- Drouet, Cotton Fabrice, Guéguen Philippe, 2010. v_{S30} , κ , regional attenuation and Mw from accelerograms: application to magnitude 3–5 French earthquakes. *Geophysical Journal International* 182, 880–898. <https://doi.org/10.1111/j.1365-246X.2010.04626.x>
- Dujardin, A., Hollender, F., Causse, M., Berge-Thierry, C., Delouis, B., Foundotos, L., Ameri, G., Shible, H., 2020. Optimization of a Simulation Code Coupling Extended Source ($k=2$) and Empirical Green's Functions: Application to the Case of the Middle Durance Fault. *Pure Appl. Geophys.* 177, 2255–2279. <https://doi.org/10.1007/s00024-019-02309-x>

- Dujardin, A., Causse, M., Berge-Thierry, C., & Hollender, F. (2018). Radiation patterns control the near-source ground-motion saturation effect. *Bulletin of the Seismological Society of America*. <https://doi.org/10.1785/0120180076>.
- Hanks, T. C. (1979). b values and $\omega - \gamma$ seismic source models: Implications for tectonic stress variations along active crustal fault zones and the estimation of high-frequency strong ground motion. *Journal of Geophysical Research: Solid Earth*, 84(B5), 2235–2242.
- Hanks, T. C., & McGuire, R. K. (1981). The character of high-frequency strong ground motion. *Bulletin of the Seismological Society of America*, 71(6), 2071–2095.
- Hartzell, S.H., 1978. Earthquake aftershocks as Green's functions. *Geophysical Research Letters* 5, 1–4. <https://doi.org/10.1029/GL005i001p00001>
- Heaton, T. H. (1990). Evidence for and implications of self-healing pulses of slip in earthquake rupture. *Physics of the Earth and Planetary Interiors*, 64(1), 1–20.
- Herrero, A., Bernard, P., 1994. A kinematic self-similar rupture process for earthquakes. *Bulletin of the Seismological Society of America* 84, 1216–1228. <https://doi.org/10.1785/BSSA0840041216>
- Hisada, Y., 2001. A Theoretical Omega-Square Model Considering Spatial Variation in Slip and Rupture Velocity. Part 2: Case for a Two-Dimensional Source Model. *Bulletin of the Seismological Society of America* 91, 651–666. <https://doi.org/10.1785/0120000097>
- Houtte, C.V., Drouet, S., Cotton, F., 2011. Analysis of the Origins of κ (Kappa) to Compute Hard Rock to Rock Adjustment Factors for GMPEs. *Bulletin of the Seismological Society of America* 101, 2926–2941. <https://doi.org/10.1785/0120100345>
- Irikura, K., & Kamae, K. (1994). Estimation of strong ground motion in broad-frequency band based on a seismic source scaling model and an empirical Green's function technique. *Annali di Geofisica* xxxvii, 6, 1721–1743.
- Kotha, S.R., Weatherill, G., Bindi, D., Cotton, F., 2020. A regionally-adaptable ground-motion model for shallow crustal earthquakes in Europe. *Bull Earthquake Eng* 18, 4091–4125. <https://doi.org/10.1007/s10518-020-00869-1>
- Lanzano, G., L. Luzi, F. Pacor, C. Felicetta, R. Puglia, S. Sgobba, and M. D'Amico (2019). A revised ground motion prediction model for shallow crustal earthquakes in Italy, *Bull. Seismol. Soc. Am.* 109, no. 2, 525–540.
- Lanzano G., C. Felicetta, F. Pacor, D. Spallarossa, and P. Traversa (2020). Methodology to identify the reference rock sites in regions of medium-to-high seismicity: an application in Central Italy, *Geophys. J. Int.* 222(3) 2053–2067.
- Lanzano, G., Sgobba, S., Luzi, L., Puglia, R., Pacor, F., Felicetta, C., D'Amico, M., Cotton, F., Bindi, D., 2019. The pan-European Engineering Strong Motion (ESM) flatfile: compilation criteria and data statistics. *Bull Earthquake Eng* 17, 561–582. <https://doi.org/10.1007/s10518-018-0480-z>
- Lanzano, G., Felicetta, C., Pacor, F., Spallarossa, D. & Traversa, P., (2022). Generic-to-reference rocks scaling factors for the seismic ground motion in Italy, *Bull. seism. Soc. Am.*, 112, 1583–1606.
- Laurendeau, A., Bard, P.-Y., Hollender, F., Perron, V., Foundotos, L., Ktenidou, O.-J., Hernandez, B., 2018. Derivation of consistent hard rock ($1000 < V_S < 3000$ m/s) GMPEs from surface and down-hole recordings: analysis of KiK-net data. *Bull Earthquake Eng* 16, 2253–2284. <https://doi.org/10.1007/s10518-017-0142-6>
- Luzi, L., Puglia, R., Russo, E., D'Amico, M., Felicetta, C., Pacor, F., Lanzano, G., Çeken, U., Clinton, J., Costa, G., Duni, L., Farzanegan, E., Gueguen, P., Ionescu, C., Kalogeras, I., Özener, H., Pesaresi, D., Sleeman, R., Strollo, A., Zare, M., 2016. The Engineering Strong- Motion Database: A Platform to Access Pan-European Accelerometric Data. *Seismological Research Letters* 87, 987–997. <https://doi.org/10.1785/0220150278>
- Miyake, H., Iwata, T., & Irikura, K. (2003). Source characterization for broadband ground-motion simulation: Kinematic heterogeneous source model and strong motion generation area. *Bulletin of the Seismological Society of America*, 93(6), 2531–2545
- Morasca, P., D'Amico, M., Sgobba, S., Lanzano, G., Colavitti, L., Pacor, F., Spallarossa, D., 2023. Empirical correlations between an FAS non-ergodic ground motion model and a GIT derived

- model for Central Italy. *Geophysical Journal International* 233, 51–68. <https://doi.org/10.1093/gji/ggac445>
- Nakano, K., Matsushima, S., Kawase, H., 2015. Statistical Properties of Strong Ground Motions from the Generalized Spectral Inversion of Data Observed by K- NET, KiK- net, and the JMA Shindokei Network in Japan. *Bulletin of the Seismological Society of America* 105, 2662–2680. <https://doi.org/10.1785/0120140349>
- Oth, A., Bindi, D., Parolai, S., Giacomo, D.D., 2011. Spectral Analysis of K-NET and KiK-net Data in Japan, Part II: On Attenuation Characteristics, Source Spectra, and Site Response of Borehole and Surface Stations. *Bulletin of the Seismological Society of America* 101, 667–687. <https://doi.org/10.1785/0120100135>
- Oth, A., Miyake, H., Bindi, D., 2015. On the Relation of Earthquake Stress Drop and Ground Motion Variability. *AGU Fall Meeting Abstracts* 51, S51A-2641.
- Pacor, F., Spallarossa, D., Oth, A., Luzi, L., Puglia, R., Cantore, L., Mercuri, A., D'Amico, M., Bindi, D., 2016. Spectral models for ground motion prediction in the L'Aquila region (central Italy): evidence for stress-drop dependence on magnitude and depth. *Geophysical Journal International* 204, 697–718. <https://doi.org/10.1093/gji/ggv448>
- Paolucci, R., Pacor, F., Puglia, R., Ameri, G., Cauzzi, C., Massa, M., 2011. Record Processing in ITACA, the New Italian Strong-Motion Database, in: Akkar, S., Gülkan, P., van Eck, T. (Eds.), *Earthquake Data in Engineering Seismology: Predictive Models, Data Management and Networks, Geotechnical, Geological, and Earthquake Engineering*. Springer Netherlands, Dordrecht, pp. 99–113. https://doi.org/10.1007/978-94-007-0152-6_8
- Russo E, Felicetta C, D Amico M, Sgobba S, Lanzano G, Mascandola C, Pacor F, Luzi L (2022). Italian Accelerometric Archive v3.2 - Istituto Nazionale di Geofisica e Vulcanologia, Dipartimento della Protezione Civile Nazionale. doi: 10.13127/itaca.3.2
- Sandikkaya, M.A., Akkar, S. Cumulative absolute velocity, Arias intensity and significant duration predictive models from a pan-European strong-motion dataset. *Bull Earthquake Eng* 15, 1881–1898 (2017). <https://doi.org/10.1007/s10518-016-0066-6>
- Shible, H., 2021. Development of a new approach to define reference ground motions applicable to existing strong-motion databases (Earth Sciences). Université Grenoble Alpes.
- Shible, H., Hollender, F., Bindi, D., Traversa, P., Oth, A., Edwards, B., Klin, P., Kawase, H., Grendas, I., Castro, R.R., Theodoulidis, N., Gueguen, P., 2022a. GITEC: A Generalized Inversion Technique Benchmark. *Bulletin of the Seismological Society of America* 112, 850–877. <https://doi.org/10.1785/0120210242>
- Shible, H., Hollender, F., Bindi, D., Traversa, P., Oth, A., Edwards, B., Klin, P., Kawase, H., Grendas, I., Castro, R.R., Theodoulidis, N., Gueguen, P., 2022b. GITEC: A Generalized Inversion Technique Benchmark. *Bulletin of the Seismological Society of America*. <https://doi.org/10.1785/0120210242>
- Shible, H., Laurendeau, A., Bard, P.-Y., Hollender, F., 2018. Importance of local scattering in high frequency motion: lessons from Interpacific project sites, application to the KiK-net database and derivation of new hard-rock GMPE. 16th european conference on earthquake engineering, Jun 2018, Thessalonique, Greece , Paper #12113.
- Somerville, P., Irikura, K., Graves, R., Sawada, S., Wald, D., Abrahamson, N., et al. (1999). Characterizing crustal earthquake slip models for the prediction of strong ground motion. *Seismological Research Letters*, 70(1), 59–80.
- Weatherill G, Cotton F (2020) A ground motion logic tree for seismic hazard analysis in the stable cratonic region of Europe: regionalisation, model selection and development of a scaled backbone approach. *Bull Earthq Eng*. <https://doi.org/10.1007/s10518-020-00940-x>

A. APPENDIX

A.1 DEFINITION OF THE USABLE FREQUENCY RANGE

An important component of the quality check of seismic signals is to evaluate the range of usable frequencies. As mentioned earlier, the ESM data are band-pass filtered, with low-pass and high-pass corner frequencies $f_{c_{LP}}$ and $f_{c_{HP}}$, respectively. Since the type of the filter applied is a 4th order Butterworth filter, we expect that the filter will still affect to some extent some frequencies $> f_{c_{HP}}$, as well as some frequencies $< f_{c_{LP}}$.

Figure 5.1 shows examples of the gain of a 4th order Butterworth filter at different $f_{c_{HP}}$ and $f_{c_{LP}}$ values. First, while fixing the $f_{c_{LP}}$ at 30 Hz and varying the $f_{c_{HP}}$ between 0.1, 0.3 and 1.0 Hz, we highlight the frequency band that is unaffected by the filter edge effects, i.e., gain $> 99\%$. We denote in each case f_{min} as the minimal frequency after which we consider the frequency band as usable. Similarly, we fix $f_{c_{HP}}$ at 0.1 Hz and variate $f_{c_{LP}}$ between 20, 25, and 30 Hz. Then, we denote f_{max} as the maximal frequency after which the signal is no longer reliable, because of filter effects. The frequency band $[f_{min} - f_{max}]$ is highlighted in Figure 5.1 with a dashed line on the gain function.

Table 5-1 shows a summary of the tested filter corner frequencies ($f_{c_{HP}}$ and $f_{c_{LP}}$) as well as the defined limits of the usable frequency band f_{min} and f_{max} . In order to generalize the deduction of a usable frequency bandwidth after the filter application, we compute the ratios of $f_{min}/f_{c_{HP}}$ and $f_{c_{LP}}/f_{max}$. We observe an almost constant value of $f_{min}/f_{c_{HP}} = 1.5$ and a value $f_{c_{LP}}/f_{max} = 1.4$. Therefore, we considered for the rest of the study that a usable bandwidth (free of filter effects) is $[f_{min} - f_{max}]$, where we calculate f_{min} as $1.5 \times f_{c_{HP}}$ and $f_{max} = f_{c_{LP}} / 1.4$.

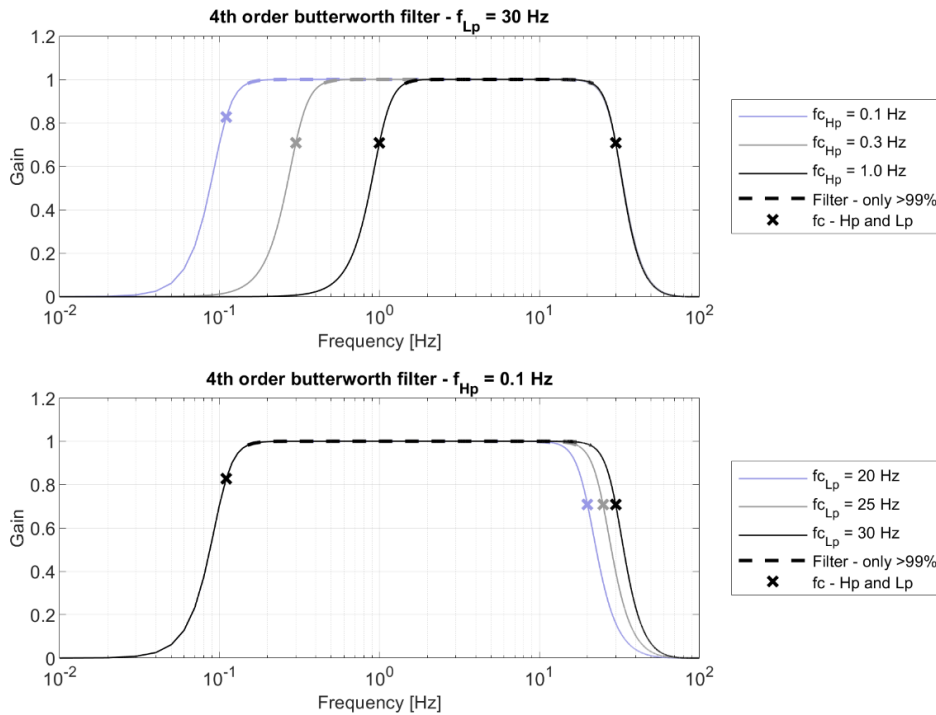


Figure 5.1: The gain of a 4th-order Butterworth filter at different $f_{c_{HP}}$ with fixed $f_{c_{LP}}=30$ Hz (upper figure), and at different $f_{c_{LP}}$ with fixed $f_{c_{HP}}=0.1$ Hz (lower figure). The dashed lines correspond to the frequency band unaffected by the filter edge effects (gain $>99\%$).

Table 5-1: Summary of filter corner frequencies ($f_{c_{HP}}$ and $f_{c_{LP}}$) and usable frequencies (f_{min} and f_{max}). The ratio of $f_{min}/f_{c_{HP}}$ and $f_{c_{LP}}/f_{max}$ is also noted.

$f_{c_{HP}}$	f_{min}	$f_{min}/f_{c_{HP}}$	$f_{c_{LP}}$	f_{max}	$f_{c_{LP}}/f_{max}$
0.11	0.15	1.50	20	13.74	1.45
0.30	0.45	1.50	25	17.34	1.40
1.00	1.44	1.44	30	21.05	1.40

A.2 SEARCHING FOR EGFS

In a first step, we identify stations in the ESM database that are within three different ranges of epicentral distances from the site, i.e., 0-100 km, 100-120 km and 120-140 km. We could find 30 stations that are within 100 km from the site, while recorded earthquakes are mainly concentrated in the Apennines regions. We also remark that the number of recording stations significantly increases if we search beyond 100 km from the METIS site.

Usually, the EGFs used in simulations are chosen among recordings of small magnitudes, which is an advantage of the approach, especially in low-to-moderate seismicity regions (Del Gaudio et al., 2018; Dujardin et al., 2020). Also, the EGFs are preferred to be covering similar source-to-station distances as those of major interest for the seismic hazard analyses. So, we apply two filters on data based on magnitudes and epicentral distances, to explore the availability of recordings, as follows:

- Data filtered to keep only magnitudes < 4.0 and $R_{EPI} < 50$ km (*filter 1*),
- Data filtered to keep only magnitudes < 5.0 and $R_{EPI} < 100$ km (*filter 2*).

Figure 5.2 shows the impact of magnitude-distance filters applied to data in terms of number of recordings. We can notice that the amount of recordings per station as well as the number of stations increase with increasing distance from the METIS site. Second, we can observe that the recordings corresponding to low-magnitude earthquakes recorded at short-distances (i.e., data after *filter 1*) are very few and only at stations beyond 80 km from the METIS site. However, widening the search ranges in *filter 2* allowed to find much more stations with sufficient number of recordings (> 5), generally distributed between 50 and 140 km. Therefore, we included data of earthquakes with magnitudes going up to 5.0, even though much lower magnitudes than 5.0 are generally preferred for EGF simulations.

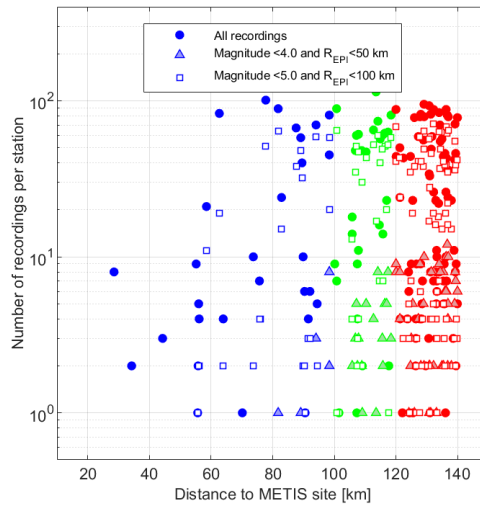


Figure 5.2: Distribution of the number of recordings per station versus the distance to the METIS site. The initial number of all recordings is represented by circles, recordings filtered to keep magnitudes < 4.0 and $R_{EPI} < 50$ km by triangles, and recordings filtered to keep magnitudes < 5.0 and $R_{EPI} < 100$ km by squares. The blue, green and red colors mark the distance ranges 0-100 km, 100-120 km and 120-140 km, respectively.

A.3 SENSITIVITY TESTS ON THE EGF SELECTION PROCEDURE

We test in this section the sensitivity of the EGF selection to different imposed criteria with the aim to refine the procedure. The initial selection ensured low- and high-pass filter (f_{LP} , f_{HP}) corner frequencies over 0.1-30 Hz. So, we test the condition on the frequency range of recordings to ensure a usable frequency range (i.e., f_{min} and f_{max}) over 0.1-30 Hz and 0.3-25 Hz.

Figure 5.3 shows the results of the selection procedure in terms of the number of recordings retained. First, we observe that ensuring a frequency range of 0.1-30 Hz for f_{min} - f_{max} instead of f_{HP} - f_{LP} leads to a significant drop in data amount, which seems insufficient for our analyses. However, if we narrow the frequency band to acceptable f_{min} - f_{max} = 0.3-25 Hz, we retain a sufficient amount of data over different distance bins. Therefore, we retain, in what follows, the condition of the usable frequency range to be acceptable on 0.3-25 Hz.

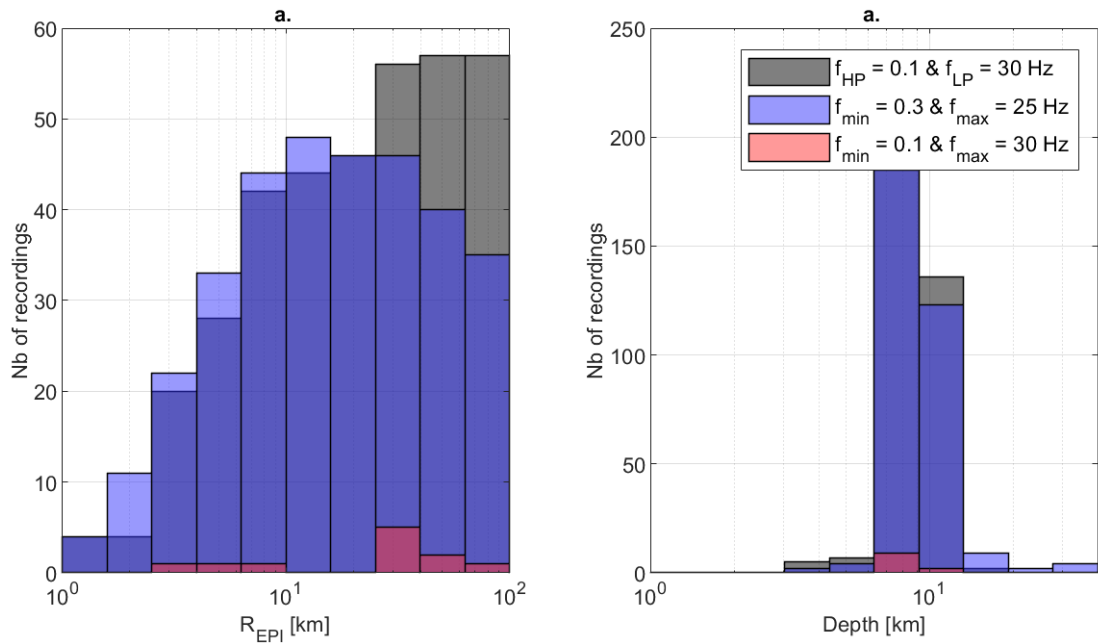


Figure 5.3: A sensitivity test on the selection procedure, by modifying the condition on the frequency band between (1) f_{HP} - f_{LP} =0.1-30 Hz, (2) f_{min} - f_{max} = 0.3-25 Hz, and (3) f_{min} - f_{max} = 0.1-30 Hz.

We test hereafter the impact of considering magnitude-distance binning or distance binning only in the selection of the EGF. Initially, the magnitude-distance binning was adopted by considering 10 equally-spaced bins of R_{EPI} (in \log_{10} scale, between 1 and 100 km) and 10 equally-spaced bins of magnitude (in linear scale between 2.5 and 5). As shown in Figure 5.4 the automatic procedure yielded a large amount of recordings by using the magnitude-distance binning, especially for distances larger than 5 km. In order, to have a manageable number of EGF and because the source spectra will be removed in our methodology, we also tested the use of the distance binning only. We observe that considering the binning in distance regulates the total number EGFs about 100, which we consider as an acceptable number as recordings for EGF simulations.

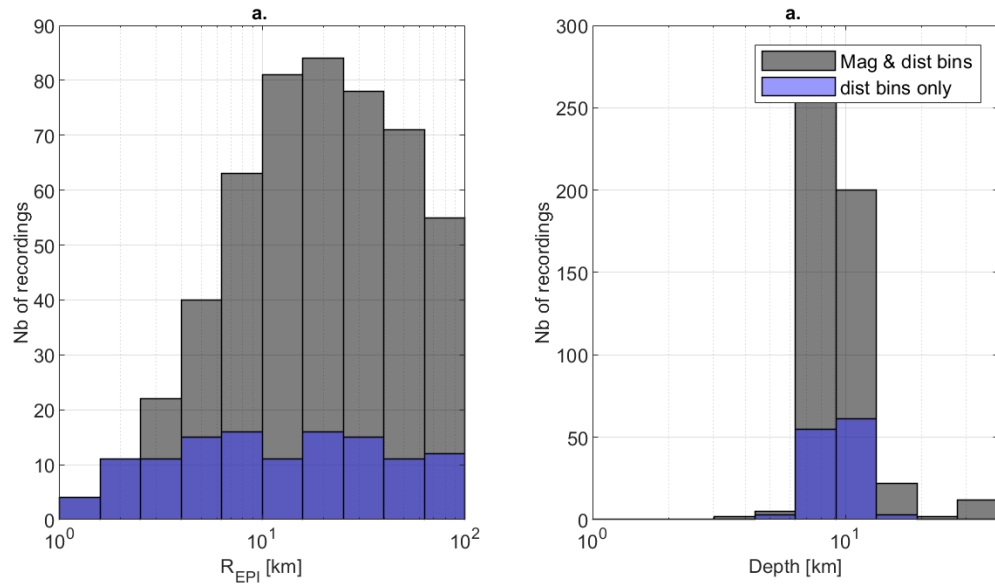


Figure 5.4: A sensitivity test on the selection procedure, by modifying the definition of bins between (1) magnitude and distance binning and (2) distance binning only.

A.4 ON THE MODELLING TRADE-OFF BETWEEN SOURCE AND SITE TERMS

The inversion results obtained using both reference conditions are highlighted in this section. Figure 5.5a and Figure 5.5b show the obtained source acceleration spectra of all earthquakes and site terms of all sites in the GIT dataset, using different reference conditions REF1 and REF2.

First, the source spectra as obtained from inversions need to be corrected since the attenuation model was constrained to 1 at a reference distance $R_{ref} = 10$ km. The source spectra shown in Figure 5.5a have been scaled systematically by a factor of 10 (that corresponds to R_{ref}). Then, the average source spectrum and the average site term are shown for results from both REF1 and REF2 conditions. We can observe the increase in the average site term, over almost all the frequency range, obtained from REF2 with respect to the average with the condition REF1 (i.e., imposed to unity). This increase in the average site term is accompanied by a decrease in the average source spectrum of REF2 inversions with respect to REF1 inversions, which highlights the existing trade-off between source and site terms.

The inversions performed using REF1 and REF2 conditions show an example of the well-known trade-off issue when dealing with GIT. This trade-off is best solved when applying additional constraints on the inversions using site-specific information, independently from GIT. However, this trade-off seems to be limited to source and site, while the attenuation results are almost not affected, which was also observed in our results (for simplicity and brevity attenuation functions are not commented on in the document). This tradeoff should not raise any difficulties for developing the EGF database that must be deconvolved by both the source and site terms.

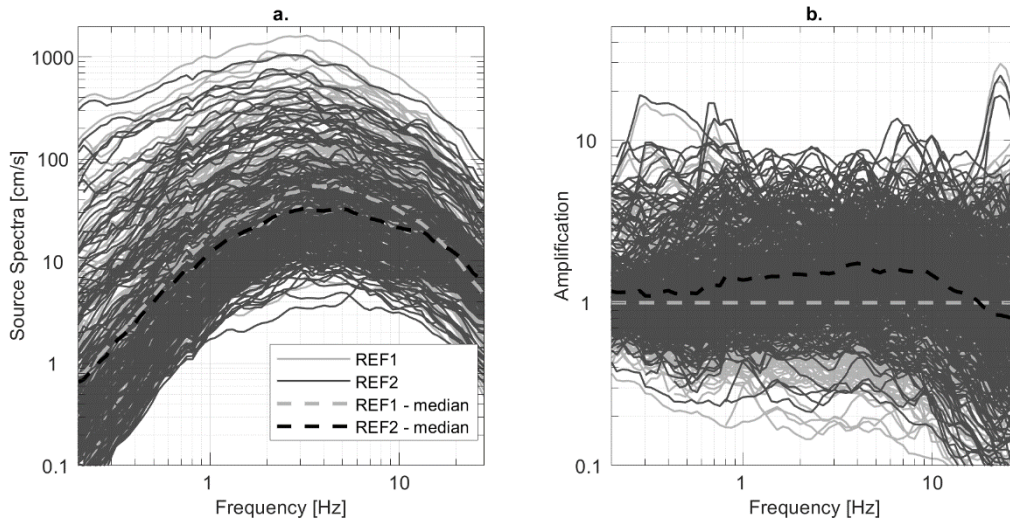


Figure 5.5 (a) Source terms of all earthquakes in the considered dataset for GIT. (b) site amplification terms obtained for all sites in the dataset. The average term in each case is marked in dashed lines. The gray lines correspond to “REF1” reference condition, while the black lines correspond to “REF2” conditions.

We do not intend, in this document, to do a detailed interpretation of source, attenuation, and site terms. Thus, we currently skip all the post-processing of GIT terms to fit them with physical models, e.g., Brune’s source model, geometrical spreading and anelastic attenuation, etc., which is also an

important step to understand ground motion characteristics. We focus on the combination of source and site terms, which we intend to use in the correction of recordings prior to the EGF simulations.

Figure 5.6 shows the source and site terms as obtained from both GIT applications (i.e., REF1 and REF2), for each of the 5 stations at which we have recordings for EGF simulations for a short distance and low magnitude events. The source spectra of earthquakes of magnitudes < 4.0 recorded at each station are shown in Figure 5.6a, the site responses are shown in Figure 5.6b, and their combination for each earthquake in Figure 5.6c. We can clearly observe that the combination of both source and site terms does not induce any changes in the associated FAS when considering either REF1 or REF2.

This clearly shows that in our intended application for the calculation of EGF at reference rock, the correction for the source-site combination will not be sensible to the choice of the reference condition.

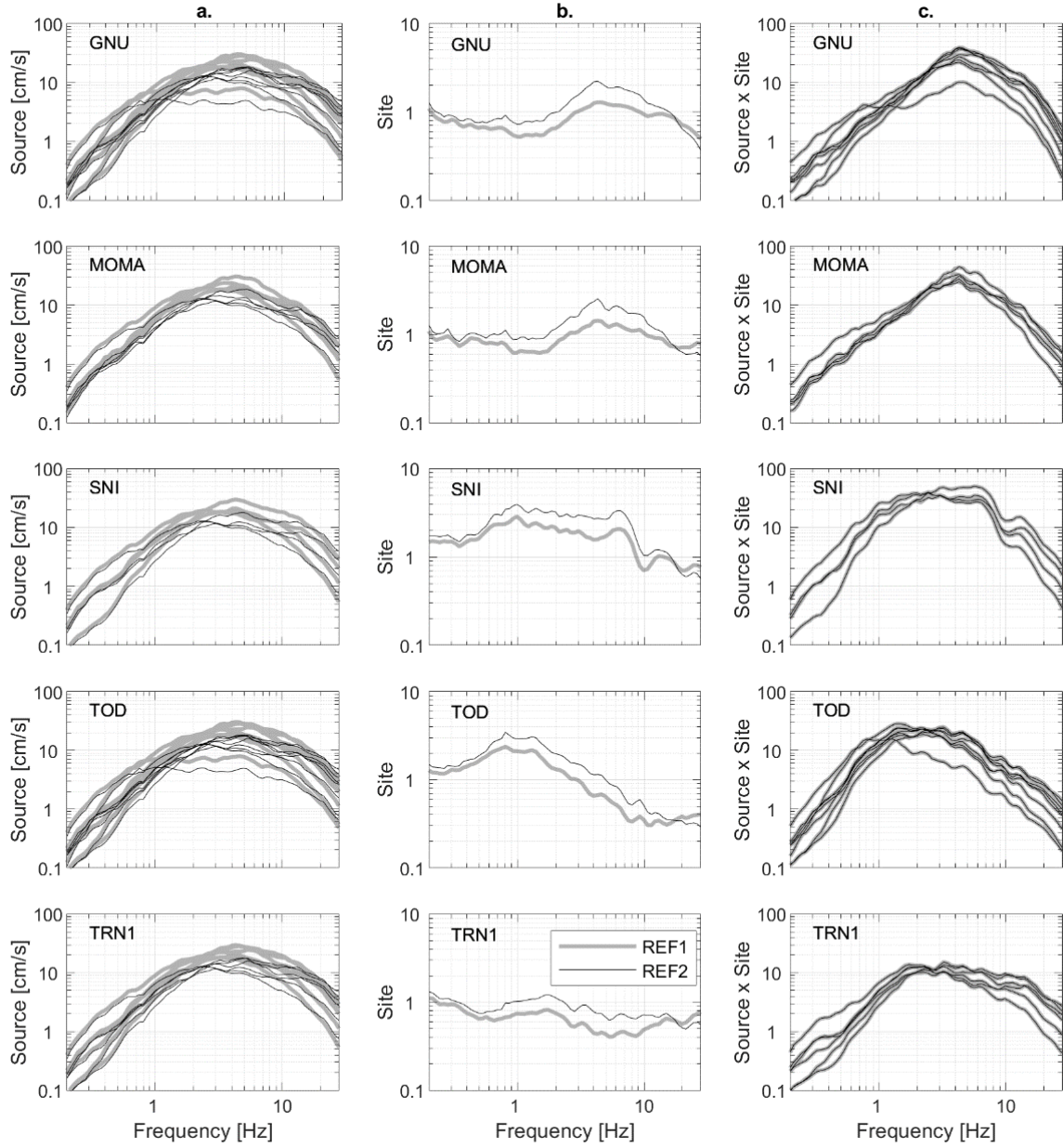
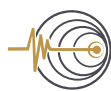


Figure 5.6 : (a) The source terms of earthquakes (magnitude <4) recorded at 5 stations in the dataset, (b) their respective site responses as obtained from GIT. (c) The source-site combination at each station. The gray and black colors correspond to inversions performed with REF1 and REF2 reference conditions, respectively.



SEISTER

SEISMIC ENGINEERING SOLUTIONS

Seister S.A.S.

Office Chatenay-Malabry

*Immeuble LE QUARTZ . 58, Rue du Chemin de la
Justice. 92290 CHATENAY-MALABRY, France*

Office Gémenos

*Le Grand Bosquet. Chemin de Font Sereine, Bât C
13420 Gémenos, France*

www.seister.fr

